



Michigan Technological University
Create the Future Digital Commons @ Michigan Tech

Dissertations, Master's Theses and Master's
Reports - Open

Dissertations, Master's Theses and Master's
Reports

2010

Electron transport in molecular systems

Haiying He

Michigan Technological University

Follow this and additional works at: <https://digitalcommons.mtu.edu/etds>

 Part of the [Physics Commons](#)


Copyright 2010 Haiying He

Recommended Citation

He, Haiying, "Electron transport in molecular systems", Dissertation, Michigan Technological University, 2010.

<https://doi.org/10.37099/mtu.dc.etds/107>

Follow this and additional works at: <https://digitalcommons.mtu.edu/etds>

 Part of the [Physics Commons](#)

ELECTRON TRANSPORT IN MOLECULAR SYSTEMS

By

HAIYING HE

A DISSERTATION

Submitted in partial fulfillment of the requirements

for the degree of

DOCTOR OF PHILOSOPHY

(Physics)

MICHIGAN TECHNOLOGICAL UNIVERSITY

2009

Copyright © Haiying He 2009

This dissertation, "Electron Transport in Molecular Systems", is hereby approved in partial fulfillment of the requirements for the degree of DOCTOR OF PHILOSOPHY in the field of Physics.

DEPARTMENT or PROGRAM:
Physics

Signatures:

Dissertation Advisor _____
Dr. Ravindra Pandey

Committee _____
Dr. Donald R. Beck

Dr. Max Seel

Dr. Marta Wloch

Dr. Shashi P. Karna

Department Chair _____
Dr. Ravindra Pandey

Date _____

Dedication

To what is unseen

Contents

Acknowledgments	xiii
Acronyms	xv
List of Figures	xxii
List of Tables	xxiv
Abstract	xxv
1 General Introduction	1
1.1 Molecular Electronics	1
1.1.1 Concept genesis	1
1.1.2 Milestones	4
1.1.3 Research horizons	8
1.1.3.1 Molecular spintronics	10
1.1.3.2 Molecular electronics in biology	11
1.2 Transport Theories	16
1.2.1 Drift-diffusion transport: Fluidic current	16
1.2.2 Boltzmann equation: Particle-based semiclassical transport . .	20

1.2.3	Quantum transport: Wave-like charactered electrons	22
2	Theoretical Methods	27
2.1	Coherent Electron Transport	29
2.1.1	Tunneling Hamiltonian formalism	30
2.1.2	Landauer-Büttiker formalism	34
2.1.3	Green's function (GF) method	38
2.1.4	Non-equilibrium Green's function (NEGF) method	42
2.1.5	Beyond coherent transport	47
2.2	Electronic Structure From First-Principles	48
2.2.1	Basic approximations	49
2.2.2	Hartree-Fock theory	51
2.2.3	Density functional theory (DFT)	54
2.2.3.1	Hohenberg-Kohn theorem	54
2.2.3.2	Kohn-Sham theorem	55
2.2.3.3	Exchange-correlation functional forms	58
2.2.4	Molecular orbital theory and basis sets	60
2.2.4.1	Molecular orbital theory	60
2.2.4.2	Basis sets	62
3	Organic Spin Valve - Role of Molecular Spacer	71
3.1	Introduction	71
3.2	Simulation Model and Computational Details	77
3.2.1	Current formalism for spin-polarized electron transport	77
3.2.2	Computational details	78

3.3	Spin-Valve Effect in a Ni-BDT···Ni System	80
3.3.1	Structural and magnetic properties	80
3.3.2	Work function	82
3.3.3	Tunneling current	83
3.3.4	Summary	90
3.4	Spin-Valve Effect in a Ni-BCODT···Ni System	91
3.4.1	Structure and energetics	92
3.4.2	Tunneling currents	94
3.4.3	Summary	98
4	Giant Magnetoresistive Effect in a Carbon Fullerene - Interface Ef-	
	fect	101
4.1	Introduction	101
4.2	Simulation Model and Computational Details	104
4.3	Site-dependency of GMR Effect in a Ni-C ₆₀ -Ni System	107
4.3.1	Ni-C ₆₀ -Ni bonding characteristics	107
4.3.2	Tunnel current and GMR	110
4.3.3	Transmission function (T)	114
4.4	Summary	117
5	Unimolecular Diodes and Transistors - Functionalization of	
	Molecules	119
5.1	Introduction	119
5.2	Simulation Model and Computational Details	124
5.3	Rectification Effect in a Donor-Bridge-Acceptor (DBA) Architecture .	128
5.3.1	Asymmetric currents under forward and reverse biases	128

5.3.2	Evolution of electronic structure under bias	129
5.3.3	Transmission functions under bias	133
5.3.4	Electronic structure mechanism - the dipole-rule	136
5.4	Transistor Behavior in an ABD-IC-DBA Architecture	137
5.4.1	Molecular design and simulation model	139
5.4.2	Tunneling current - enhancement/depletion gating effect . . .	141
5.4.3	Molecular orbital energy shift - polarization effect	143
5.4.4	Evolution of molecular orbital wave characters - gate molecule intervention effect	146
5.5	Summary	149
6	Modified Nanopore DNA Sequencing - Functionalization of Elec- trodes	151
6.1	Introduction	151
6.2	Simulation Model and Computational Details	154
6.2.1	Simulation model	154
6.2.2	Electronic structure and geometry optimization	157
6.2.3	NEGF quantum transport formalism	158
6.3	Differentiation of DNA Bases - Static Calculations	160
6.3.1	Base paring and binding energies	160
6.3.2	Tunneling currents and recognition map	161
6.3.3	Detection Using Force Signal	165
6.4	Dynamic Stability of Currents - Molecular Dynamic Simulations . . .	166
6.4.1	Modeling and methods	167
6.4.2	Stability of pairing geometry	168
6.4.3	Stability of tunneling current	171

6.4.4	Influencing factors for tunneling current	173
6.4.4.1	Vacuum size	173
6.4.4.2	Hydrogen bonds	174
6.4.5	Base recognition scheme	180
6.5	Summary	181
7	Grand Summary and Future Perspectives	183
7.1	Grand Summary	183
7.2	Future Perspectives	187
	Appendix	193
A	Accuracy and Computational Cost: A Case Study in Smeagol	193
B	List of Related Publications	195
	Bibliography	198

Acknowledgments

I am not standing alone with what is finished on me today. I would give thanks to the Lord who has guided my ways, walked side by side with me and done every goodness in me.

I would like to thank Prof. Ravindra Pandey, my advisor, who has provided this precious opportunity for me to continue to study in US. He has been a great tutor for both my academic and personal life. He has taught me to learn, understand and appreciate physics from every perspective. He has also taught me how to teach my children and have close family relations.

I am greatly grateful to Prof. John Vail, another person who led me to a continuing study in physics. He has also been a good teacher and friend ever since. I learned from him how important thinking is.

I would sincerely thank Prof. Donald R. Beck, Prof. Max Seel, Prof. Marta Wloch and Prof. Shashi P. Karna for being my advisory committee members and reading through this dissertation and giving valuable comments and suggestions.

I would give special thanks to Prof. Ranjit Pati, who first introduced me to the topic of molecular electronics. His kindness and patience gave me more than a good experience in research.

Thanks to our collaborators Prof. Udo Pernisz, Prof. Richard Brown, Prof. Miguel

Blanco, Prof. Roberto Orlando, Prof. Michel Rérat, Dr. Alexandre Reily Rocha, Prof. Stefano Sanvito, Dr. Anton Grigoriev, Prof. Rajeev Ahuja, Dr. Govind Mallick, Emilie Amzallag, Isabelle Baraille. I would also sincerely thank my 2008 summer intern advisors Dr. Enrique R. Batista and Dr. Richard L. Martin in Los Alamos National Laboratory and our collaborators there Dr. Ping Yang, Dr. Darryl L. Smith, Dr. Sergei Tretiak, Dr. Avadh Saxena, and Dr. Svetlana V. Kilina.

Help from colleagues worked/working in our research group Dr. Ralph H. Scheicher, Prof. Dilip Kanhere, Dr. Mrinalini Despande, Dr. Aurora Costales, Dr. Anil Kandam and Dr. Huitian Jiang is greatly appreciated. Also special thanks to two senior office mates Kah Chun Lau and S. Gowtham, who have worked closely with me on research, computer and even life problems. I also appreciate working together with the current office mates Xiaoliang Zhong, Saikat Mukhopadhyay and Chunhui Liu.

This work could not be possible without the support of my family. My husband has always been working behind me. My children probably could not understand now how important they are a motivation to me, even though dragging my legs sometimes. My parents and my sister are also always there for me.

Last, but not the least, I would give thanks to all the brothers and sisters in the Lord, Kedmon and Chipo Hungwe, Lin Pan and Hongwei Yu, Shijuan Wang and Yong Peng, Yan Li and Chunming Gao, Ruihong Zhang and Zhenlin Wang, to name just a few.

Acronyms

AFM	Atomic Force Microscopy
B3LYP	Becke 3-parameter exchange and Lee, Yang and Parr correlation functional form
BCODT	bicyclo[2.2.2.]octane-1,4-dithiol molecule
BDT	benzene-1-4-dithiol molecule
BTH	Bardeen, Tersoff and Hamann formalism
CNT	carbon nanotube
DBA	donor-bridge-acceptor
DFT	density functional theory
DOS	density of states
FET	field effect transistor
GGA	generalized gradient approximation
GMR	giant magnetoresistance
HF	Hartree-Fock
HJBT	heterojunction bipolar transistor
HOMO	highest occupied molecular orbital
JMR	junction magnetoresistance
KS	Kohn-Sham
LCAO	linear combination of atomic orbitals
LDA	local density approximation
LUMO	lowest unoccupied molecular orbital
MD	molecular dynamics
MIGS	metal-induced gap state
MOS	metal oxide semiconductor
MWCNT	multiwalled carbon nanotube
NBO	Natural Bond Orbital
NDR	negative differential resistance
NEGF	non-equilibrium Green's function
PBE	Perdew, Burke and Ernzerhof exchange-correlation functional form
TP	para-terphenyl molecule
PW91	Perdew-Wang exchange and correlation functional form

SAM	self-assembled monolayer
SCF	self-consistent field
SIESTA	Spanish Initiative for Electronic Simulations with Thousands of Atoms program
SMEAGOL	Spin and Molecular Electronics in an Atomically Generated Orbital Landscape program
ssDNA	single-stranded DNA
STM	Scanning Tunneling Microscopy
STS	Scanning Tunneling Spectroscopy
VASP	Vienna Ab initio Simulation Package

List of Figures

1.1	Paradigms of transport theories spanning from macroscopic to atomic scales [75].	17
2.1	Illustration of (a) a two-terminal molecular electronic device, and (b) electron current flow under a bias of V with the electrochemical potentials at the left and the right electrodes maintained at μ_1 and μ_2 , respectively [75].	28
2.2	An example of the flow chart of the NEGF self-consistent procedure as implemented in an <i>ab initio</i> quantum transport code SMEAGOL based on the electronic structure code SIESTA [45].	45
2.3	Schematic illustration of all-electron (solid lines) and pseudoelectron (dashed lines) potentials and their corresponding wavefunctions. The radius at which all-electron and pseudoelectron values match is defined as r_c [112].	68
3.1	A schematic illustration of the self-assembled BDT monolayer on the Ni(111) substrate and the Ni probe tip separated by vacuum in a STM experiment. Notation of symbols: red - Ni; cyan - S; blue - C; green - H.	80
3.2	The magnetization density of the Ni surface layer (a) before (left), and (b) after (right) the deposition of the SAM.	81
3.3	The planar average electrostatic potential along the z direction for one unit cell of the BDT monolayer coated on Ni(111).	82
3.4	$I - V$ curves for the parallel ($\uparrow\uparrow$) and anti-parallel ($\uparrow\downarrow$) alignments of spins of the tip-molecular wire system. The contribution to the total currents from spin-up (\uparrow) and spin-down (\downarrow) states in both parallel and anti-parallel spin alignments is shown in the inset for using Ni_{13} as the tip cap.	84

3.5	The projected density of states of the BDT monolayer on Ni(111). Zero of the energy is aligned to the Fermi energy.	85
3.6	The projected density of states of the probe tip cap consisting of a Ni atom, a Ni ₅ cluster and a Ni ₁₃ cluster respectively. The energy levels are broadened using the Gaussian smearing of width 0.2 eV.	86
3.7	I-V curves for the parallel ($\uparrow\uparrow$) and anti-parallel ($\uparrow\downarrow$) alignments of spins of the tip-molecular wire system with Ni ₅ as the cap configuration. Sigma represents the width of the Gaussian smearing used to take into account the semi-infinite nature of the tip.	87
3.8	A diagram showing the origin of spin-valve effect the tip-molecular wire system with Ni ₁₃ as the cap configuration under a positive bias on the sample. The arc arrow represents the electron current flow, expressing both the direction and magnitude.	88
3.9	A sketch of the geometrical configurations of benzene-1-4 dithiol (BDT) and bicyclo[2.2.2]octane-1,4-dithiol (BCODT) molecules. Notations of S1, S2 and C1 - C4 are referred to the sulfur or carbon atoms in the molecules in an ascending order of the distance away from the Ni(111) substrate.	91
3.10	$I - V$ curves for the parallel (P) and anti-parallel (AP) spin configurations of the tip-vacuum-SAM-substrate system. The contribution to the total currents from spin-up and spin-down electrons in both parallel and anti-parallel spin configurations is shown in the inset. . .	94
3.11	The projected density of states (PDOS) of the BCODT and BDT monolayers on Ni(111). Zero of the energy is aligned to the Fermi energy.	96
3.12	The spin density isosurface of (a) BCODT and (b) BDT monolayers deposited on Ni(111) substrate. The charge density of the HOMO of the corresponding molecule is also shown in the inserted box.	97
4.1	Binding sites of Ni on C ₆₀ : (a) B66 - a bridge site over a C=C double bond; (b) B56 - a bridge site over a C-C single bond ; (c) H6 - a hole site above the center of a hexagonal ring of C atoms; (d) H5 - a hole site above the center of a pentagonal ring of C atoms.	102

4.2	A schematic illustration of a Ni-C ₆₀ -Ni molecular device. Top: The left/ right contact region is modeled by a Ni atom and the rest of the semi-infinite electrode is a Ni bulk reservoir, described by an effective self-energy Σ . Bottom: A slice of the charge density plots of the core scattering region is shown for the B66 binding site of C ₆₀	105
4.3	Current-voltage curves for parallel (PL) and anti-parallel (AP) spin orientations of Ni leads in Ni-C ₆₀ -Ni. The B66, B56, H5 and H6 are binding sites of C ₆₀	110
4.4	Differential conductance (dI/dV) vs. voltage curves for parallel (PL) and anti-parallel (AP) spin orientations of Ni leads in Ni-C ₆₀ -Ni. The B66, B56, H5 and H6 are binding sites of C ₆₀	111
4.5	Junction magnetoresistance (JMR) vs. voltage plots for Ni-C ₆₀ -Ni. The B66, B56, H5 and H6 are binding sites of C ₆₀	113
4.6	Transmission functions for (a) parallel (P) and (b) anti-parallel (AP) spin orientations of Ni leads in Ni-C ₆₀ -Ni. The Kohn-Sham orbitals are also given; pure C ₆₀ orbitals are in black, hybrid states are in magenta, and pure Ni orbitals are in green. The B66 and H6 are binding sites, and zero of the energy is aligned to the Fermi energy.	115
4.7	Molecular orbitals for α -HOMOs of Ni-C ₆₀ -Ni in which Ni is bonded at B66 (left) and H6 (right) sites in the parallel (P) case. One of C ₆₀ 's LUMOs takes part in the hybridization with Ni $3d_{xy}$ and $3d_{x^2-y^2}$ to generate the metal induced gap states (MIGS) in Ni-C ₆₀ -Ni. The orientation of Cartesian coordinates is also given here.	116
5.1	Schematic illustration of the extended molecules (a) Au ₂ -DBA-Au ₂ , (b) Au ₂ -TP-Au ₂ coupled to the left and the right electrodes. The semi-infinite effect of the electrodes is included by the self-energy term Σ . The atoms are labeled as C in gray, N in blue, H in white and Au in yellow.	125
5.2	Current-voltage curves for DBA (in red solid circle and solid line) and TP (in green empty circle and dashed line). The calculated rectification factor for DBA is plotted in the inset.	128

5.3	Electrostatic potential for DBA under a bias of (a) -1.20 V, (b) 0.00 V and (c) 1.20 V (excluding the linear potential drop due to the external electric field). The green surfaces correspond to the regions with a positive electrostatic potential energy of 0.1 eV, whereas the purple areas correspond to the regions with a negative electrostatic potential energy of -0.1 eV.	130
5.4	Molecular spectra of the DBA extended molecule under a series of external electric field. The HOMO orbital due to the donor group (D) is in green and the first DBA virtual orbital due to the acceptor group (A) is in magenta. The pseudo Fermi level E_F in each case is taken as the average between the HOMO (a D orbital, in green) and the LUMO (a Au orbital, in black) of the extended molecular system.	131
5.5	Plots of (a) the highest occupied (D-orbital) and (b) the lowest unoccupied (A-orbital) (excluding Au orbitals) molecular orbitals with the isovalue=0.02 $e/\text{\AA}^3$	132
5.6	Transmission functions for DBA under a series of forward bias. The bias windows are shown in magenta lines. The pseudo Fermi level is aligned to zero.	134
5.7	Illustration of current rectification mechanism in a D-B-A type of molecule with weak donors and acceptors. The bias window is shown in light blue.	136
5.8	Schematic illustration of the setup of a unimolecular transistor ABD-IC-DBA in measurement. C atoms are in gray, N in blue, H in white, and Au in yellow. In this diagram, a positive bias is applied upon the source (S) and the drain (D) termini, where the drain has a higher potential (i.e. a lower potential energy). A top-and-bottom double gate is applied generating a uniform positive gate field E pointing downward in the same direction as that of the intrinsic dipole moment of the entire molecule.	139
5.9	$I - V$ curves for the molecular system under an applied positive gate electric field (labeled) in the range of 0.0 to 9.25×10^8 V/m. The calculated modulation factor I_{ON}/I_{OFF} is also plotted in the inset. . .	141
5.10	Molecular spectra of the Au_2 -ABD-IC-DBA- Au_2 extended molecule under a series of gate fields. The highest occupied orbitals due to the donor group (D) are in green; the lowest unoccupied orbitals due to the acceptor group (A) are in magenta; the highest occupied orbital due to the IC molecule is in red.	144

5.11	Evolution of molecular orbitals of the $\text{Au}_2\text{-ABD-IC-DBA-Au}_2$ extended molecule under a series of gate fields: (a) 0 V/m, (b) 6.17×10^8 V/m and (c) 9.25×10^8 V/m. The highest occupied orbitals due to the donor group (D) are labeled in sequence of D1, D2, D3 and D4. The highest occupied orbital due to the IC molecule is labeled as IC.	146
5.12	Transmission functions for the ABD-IC-DBA molecular system under a series of gate fields (labeled in the figure in unit of 10^8 V/m). The transmission peaks due to the second pair of the highest occupied D orbitals D3 and D4 are labeled by * and +, respectively. The pseudo Fermi level is aligned to zero.	147
6.1	An illustration of the proposed device: ssDNA is passing through the nanopore with functionalized gold electrodes embedded. A probe molecule (e.g. Cytosine) is immobilized on the inner surface of the left electrode by a sulfur atom. As part of the ssDNA molecule, a Guanosine monophosphate unit is shown as the target to be identified.	155
6.2	Five initial C-G base-pairing geometries.	157
6.3	The current-voltage curves for the device functionalized with a C-probe for all four possible target bases (A: red square; C: green circle; G: blue triangle; T: pink upside-down triangle) with current signals plotted in logarithmic scale. The current signals are taken as ratios with respect to the value of having C as the target at a bias of 0.1 V.	162
6.4	Flow diagram illustrating the decision-making process of a device involving C-probe leading to the identification of a target base in the sequence. Here, "high" and "low" refer to higher or lower current values at a given bias voltage. The height of the bars below the letters A, C, G, and T on the right side of the figure corresponds to the respective current signal (on a logarithmic scale). The crossed-out letters below the bars refer to possible target bases that have been ruled out.	164
6.5	T-X (X=A, C, G and T) pairing geometries by energy minimization.	169
6.6	Current variation as a function of MD simulation time for T-X (X=A, C, G, T) pairing systems at a bias of 250 mV.	171
6.7	Tunneling currents of the C-G paring system as a function of the MD simulation time at a bias of 250 mV.	172

6.8	Transmission functions for (a) the T-A and (b) the C-G pairing system sampled from the MD simulations at a bias of 250 mV. The bias window is indicated by vertical black lines. The Fermi level is aligned to zero.	174
6.9	Current variation as a function of the average H-bond length at a bias of 250 mV. It is fitted by an exponential decay in red.	175
6.10	Transmission functions for the C-G pairing system with the average H-bond length varying from 1.8 to 2.2 at (a) zero bias and (b) a bias of 250 mV. The Fermi level is aligned to zero. A bias window of $-125 \text{ meV} < E - E_F < 125 \text{ meV}$ is indicated by vertical black lines on both graphs for easy of tracking the shift in peak positions near E_F	176
6.11	Electrostatic potential profile varies as a function of the strength of hydrogen bonding (reflected from the bonding length R_{HB} as labeled in the figure) between the C-G pairing.	177

List of Tables

3.1	Bond lengths (R) and binding energy (E_b) of bicyclo[2.2.2]octane-1,4-dithiol (BCODT) and benzene-1-4-dithiol (BDT) adsorbed on Ni(111).	92
4.1	Symmetry, bond lengths (R_{Ni-C}), relative total energy (E_t) with the total energy of the triplet state at the B66 binding site set to zero, magnetic moment of Ni (μ) and extra charges on Ni atoms (Q_{Ni}), on nearest neighbor C atoms (Q_{nn-C}), on second nearest neighbor C atoms (Q_{2nn-C}) of Ni-C ₆₀ -Ni extended molecular complex with different binding sites of Ni on the C ₆₀ cage surface.	108
5.1	Summary of the dipole moments, the energy gap between the D/A frontier orbitals $\Delta(\epsilon_A - \epsilon_D)$ and the HOMO (due to the D group) energy with respect to the pseudo Fermi level $\Delta(\epsilon_D - E_F)$ of the extended molecule under a series of applied electric fields. The corresponding applied potentials are also calculated from the knowledge of the distance between two electrodes.	129
5.2	Summary of the total energy, the dipole moment, and the HOMO (due to the D group) energy with respect to the pseudo Fermi level $\Delta(\epsilon_D - E_F)$ of the extended molecule under a series of applied electric fields along the gate direction. The corresponding applied gate potentials are also calculated from the knowledge of the distance between the top and the bottom gates, which is assumed to be 32 Å*.	143
6.1	Binding energy E_b (in eV) for DNA base pairs used in transport calculations.	160
6.2	Vacuum size between the target and the right electrode (in Å) for different probe-target combinations.	161

6.3	Summary of the information deducible for different probes from current measurements (at 100 mV and 250 mV) or from a force signal (proportional to the binding energy). Target bases that cannot be distinguished are combined in parentheses.	163
6.4	Binding energy E_b and geometrical characteristics for T-X (X=A, C, G, T) DNA base pairs optimized using energy minimization.	169
6.5	Individual H-bond lengths, the average H-bond length as well as the vacuum size along the transport direction (z-axis) between G and the right electrode for the C-G pairing system sampled from the MD simulation.	178
A.1	A convergence test of the calculated current with respect to the k -point sampling (Monkhorst-Pack kgrid) on a system of Au ₆₄ -Cytosine-Guanine · · Au ₆₄ using the parallel SMEAGOL code. The current is calculated at a single voltage of 0.25 V using 8 processors in parallel. The total number of atoms, electrons and orbitals are 178, 301, and 488, respectively. The mesh cutoff is set to 150 Ryd.	194

Abstract

The remarkable advances in nanoscience and nanotechnology over the last two decades allow one to manipulate individual atoms, molecules and nanostructures, make it possible to build devices with only a few nanometers, and enhance the nano-bio fusion in tackling biological and medical problems. It complies with the ever-increasing need for device miniaturization, from magnetic storage devices, electronic building blocks for computers, to chemical and biological sensors. Despite the continuing efforts based on conventional methods, they are likely to reach the fundamental limit of miniaturization in the next decade, when feature lengths shrink below 100 nm. On the one hand, quantum mechanical effects of the underlying material structure dominate device characteristics. On the other hand, one faces the technical difficulty in fabricating uniform devices. This has posed a great challenge for both the scientific and the technical communities. The proposal of using a single or a few organic molecules in electronic devices has not only opened an alternative way of miniaturization in electronics, but also brought up brand-new concepts and physical working mechanisms in electronic devices.

This thesis work stands as one of the efforts in understanding and building of electronic functional units at the molecular and atomic levels. We have explored the possibility of having molecules working in a wide spectrum of electronic devices, ranging from molecular wires, spin valves/switches, diodes, transistors and sensors.

More specifically, we have observed significant magnetoresistive effect in a spin-valve structure where the non-magnetic spacer sandwiched between two magnetic conducting materials is replaced by a self-assembled monolayer of organic molecules or a single molecule (like a carbon fullerene). The diode behavior in donor(D)-bridge(B)-acceptor(A) type of single molecules is then discussed and a unimolecular transistor is designed. Lastly, we have proposed and primarily tested the idea of using functionalized electrodes for rapid nanopore DNA sequencing. In these studies, the fundamental roles of molecules and molecule-electrode interfaces on quantum electron transport have been investigated based on first-principles calculations of the electronic structure. Both the intrinsic properties of molecules themselves and the detailed interfacial features are found to play critical roles in electron transport at the molecular scale. The flexibility and tailorability of the properties of molecules have opened great opportunity in a purpose-driven design of electronic devices from the bottom up. The results that we gained from this work have helped in understanding the underlying physics, developing the fundamental mechanism and providing guidance for future experimental efforts.

Chapter 1

General Introduction

1.1 Molecular Electronics

1.1.1 Concept genesis

Although the use of organic molecular materials in a two-terminal electronic setup can be traced back into 1971, when Mann *et al.* first proved the exponential decrease of conductivity vs. thickness through fatty acid salt monolayers predicted by the quantum tunneling theory [1], the serious consideration of molecules as effective functional elements in electronic devices did not come until 1974, when Aviram and Ratner proposed that single molecules with a donor-bridge-acceptor structure would have rectifying properties when placed between two electrodes [2]. This proposal has

generalized *molecular conduction* to *molecular electronic devices*.

In that seminal paper of Aviram and Ratner, the authors demonstrated the possibility of having synthetic electronic devices based on organic molecules. A simple electronic device, a rectifier, was constructed using a single organic molecule which has a relatively electron-poor aromatic subunit (p-type like) and a relatively electron-rich aromatic subunit (n-type like). So this molecular diode was constructed in the analogy to the p-n junction in semiconductors. But instead of doping in semiconductors, the differentiation of electron poor and rich regions is realized by the use of substituent groups on aromatic system, owing to the great success of synthesis and organic chemistry. Those substituents classified as electron withdrawing (that is, showing positive Hammett constants [3, 4]), such as -CN, -Cl, -NO₂, =O, will cause their aromatic subunit to become relatively poor in π electron density, thus raising the electron affinity and making the subunit a good electron acceptor. Conversely, electron-releasing substituents, such as -NH₂, -OCH₃, -OC₂H₅, will increase the π -electron density, thereby lowering the ionization potential and rendering the subunit a good electron donor [5, 6, 2]. A σ -bonding bridge was used to insulate the donor and acceptor subunits in their paper.

The idea was not trivial at all at an age that electronics has been essentially identified with the metal-oxide-semiconductor (MOS) large-scale-integration circuits [7]. It was triggered in some sense by the thinking that "within biological systems, some tasks performed by solid-state devices in electronic applications are performed, instead,

by organic molecule; such tasks include storage and transfer both of energy and of electrons" [2]. Study of charge transfer in molecules was initiated in the 1940s by Joseph Weiss [5] and explained from quantum mechanics by Richard Mulliken in the 1950s [8, 9] in the discussion of the so-called "donor-acceptor" systems. In his Science publication of 1968, Albert Szent-Györgyi coined the word "bioelectronics" pointing out that even molecules with low reactivity, which play a major role as metabolites or hormones, can give off a whole electron, forming a free radical; this suggested that charge transfer may be one of the most common and fundamental biological reactions [10]. The idea was later rationalized by Karna and coworkers [11] carrying out *ab initio* studies on the electron transfer in organic molecules, and providing a mechanism for designing conformational molecular switches. It is an esteemed example that the understanding of the inorganic world helps us to understand the living world or vice versa and expand our thinking.

There were two more driving forces at that time that made "molecular electronics" tangible. One was the success of finding organic equivalents of inorganic electronic systems: semiconductors, metals, superconductor, batteries, etc. in the study of organic charge-transfer crystals and conducting polymers in the 1960s and 1970s [12]. The other was due to the remarkable visionary work of Forrest L. Carter [13] and his initiation of scientific conferences on molecular electronic devices starting from the early 1980s [14, 15, 16].

To sum up, the basic idea of molecular electronics is to use single molecules or a group

of molecules as the basic elements (transistors, wires, etc.) of electronic devices. In this way the size of computers can be reduced dramatically, allowing for an enormous increase in their speed and memory. Comparing traditional electronic circuits with molecular circuits, the time cycle order of magnitude will go from nanoseconds to femtoseconds. Although there has been obscurity in the definition of the scope of molecular electronics, I would in this work stick to the definition of "molecular-scale" electronics [17].

1.1.2 Milestones

The incorporation of molecules in electronic devices brought great challenge in experiments because of the small size of molecules and difficulty in obtaining good contacts.

The milestones in *experimental* molecular electronics are:

1) The invention of *scanning tunneling microscopy* (STM) in 1983 [18] made molecular electronic devices from legacy to reality. It was applied to molecular electronics shortly after its birth [19, 20, 21, 22, 23]. Since basic electronic functions in these future devices are performed on a molecular level, STM is an ideal tool for imaging, manipulating and characterizing the electronic properties of these molecules. The conductance measurement goes one step further from macroscopic to nanoscopic in electronics. And the current-voltage characteristics can be measured at the molecular scale.

2) It took almost two decades before the solid evidence of Aviram-Ratner ansatz of *unimolecular rectification* came out from the experimental work of Martin *et al.* in 1993 [24]. By introducing passive organic spacer layers between the active molecules and metal electrodes in a metal/Langmuir-Blodgett multilayer/metal junction using a planar geometry [25], the authors proved that the rectifier-like characteristic is unequivocally associated with the molecular structure, the basis for molecular electronics. The first proven two terminal molecular device, however, was reported through a monolayer of γ -hexadecylquinolinium tricyanoquinomethanide, about four years later by Metzger's group based on both macroscopic and nanoscopic (Scanning Tunneling Spectroscopy: STS) current-voltage measurements [26].

3) Two terminal *conductance measurements on single molecules* were first reported by Mark Reed's group in 1997 [27]. In their study, molecules of benzene-1,4-dithiol were self-assembled onto the two facing gold electrodes of a mechanically controllable break junction to form a statically stable gold-sulfur-aryl-sulfur-gold system, allowing for direct observation of charge transport through the molecules. This study provides a quantitative measure of the conductance of a junction containing a single molecule, which is a fundamental step in the emerging area of molecular-scale electronics.

4) The *conductance quantum* was measured for a molecular system for the first time in 1998 when a carbon nanotube, glued to a conducting AFM tip, was lowered into liquid Hg at room temperature [28]. In this case, ideal contacts are made to the nanotube, and none of the electrons entering or leaving the nanotube will be backscattered by

the contact. Two important findings deserve to be pointed out. First, conductance quantization were observed in multiwalled carbon nanotubes (MWCNTs) at room temperature. The fundamental quantum of conductance G_0 is equal to $2e^2/h=(12.9 \text{ kilohms})^{-1}$, where e is the charge of an electron and h is the Planck constant. This confirmed the theoretical prediction of the quantized conductance [29, 30, 31]. Secondly, the nanotubes conduct current ballistically (no length-dependence of the resistance) and do not dissipate heat. Instead, the Joule heat is dissipated in the electrical leads, which connect the ballistic conductor (MWCNT) to the macroscopic elements of the circuit (reservoirs). It implies that the electrons in nanotubes are strongly decoupled from the lattice. "Hot" electrons are efficiently removed by the liquid-metal contact rather than being converted into lattice vibrations. Extremely high stable current densities, $J > 10^7 \text{ A/cm}^2$, have been attained (for comparison, J for superconductors is typically on the order of 10^5 A/cm^2).

5) *Negative differential resistance* (NDR) and large on-off ratios were observed for the first time in a molecular device by J. Chen *et al.* in 1999 [32]. In their experiments, molecules containing a nitroamine redox center were self-assembled in a nanopore on a gold surface using sulfur atoms as alligator clips. In a following work, J. M. Seminario *et al.* [33] explained this electrical characteristic by density functional theory (DFT) calculations. The resonant tunneling diode (RTD) behavior is due to a modification of the electronic wavefunctions extending through the molecules. The critical parameters are the HOMO-LUMO gap (HLG) and the spatial extent of the

unoccupied orbitals, since delocalisation is needed to have electron transport. Their results showed how the existence of electronic pathways in the molecule depends strongly on the charging of the molecule under bias.

6) A *room-temperature transistor* (a three-terminal switching device) based on a single carbon nanotube was reported in 1998 [34]. The fabricated device consisted of one semiconducting single-wall carbon nanotube connected to two metal electrodes, and deposited on a Si/SiO₂ back gate. By applying a voltage to a gate electrode, the nanotube can be switched from a conducting to an insulating state. The conductivity of the device changed by about six orders of magnitude upon a change of 10 V in the gate voltage, as a consequence of the modulation of the nanotube band structure induced by the gate and drain-source voltages. Electrical measurements on the nanotube transistor indicate that its operation characteristics can be qualitatively described by the semiclassical band-bending models currently used for traditional semiconductor devices. The fabrication of the three-terminal switching device at the level of a single molecule represents an important step towards molecular electronics. A single electron transistor working at room temperature and based on carbon nanotubes has also been demonstrated [35]. A recent breakthrough in molecular transistors were reported by R. Wolkow and colleagues in 2005 [36]. From STM observation, they have demonstrated that the electrostatic field emanating from a fixed point charge regulates the conductivity of nearby substrate-bound molecules. The onset of molecular conduction is shifted by changing the charge state of a silicon surface atom, or by

varying the spatial relationship between the molecule and that charged center. Classical electrostatic and quantum mechanical calculations were used to model charging and level-shifting effects, which in turn explained the current-voltage spectra and the change of "turn-on" voltages. Because the shifting results in conductivity changes of substantial magnitude, these effects are easily observed at room temperature. A molecule could be controllably charged by a single atom while all adjacent atoms remained neutral. In contrast to the global gating, the local gating was brought to life for the first time in this work, which is extremely important in the integration of this type of transistors into circuits.

1.1.3 Research horizons

The call for molecular electronics has been ever increasing especially after the late 1990s because of the impending need of miniaturization in electronics. Despite the very high resolution reached up to now using the conventional top-down approach, which exploits the ability to realize smaller and smaller structures using lithography and related techniques [37] for the construction of both electronic components and microelectromechanical systems (MEMs), Si electronics is reaching intrinsic physical limitations in about one decade. It means that the famous legacy of the Moore's law is not sustainable using standard (lithographic) approaches due to three fundamental limits [38]. (1) The energy needed to write a bit must be bigger than the average

energy of the thermal fluctuations ($k_B T$) to avoid bit errors (thermal limit). (2) The energy necessary to read or write a bit and the frequency of the circuits are limited by the uncertainty principle (quantum limit). Finally, (3) a maximum tolerable power density exists (power dissipation limit). Technological and economic limitations related to the growing difficulties in fabricating smaller and smaller devices complete this picture.

Different from the top-down approach, molecular electronic devices use a bottom-up approach. It has turned out to be a promising alternative to build nanodevices and/or nanomachines starting from molecular building blocks instead of carving lithographically bigger pieces of matter into smaller and smaller chunks [38, 39]. Today, molecular electronics is developing under a cross-disciplinary effort from chemical, biological, physical, and engineering communities.

It has shown a wide range of applications, switches, wires, diodes, transistors, biosensors, just name a few. They cover from building blocks for revolutionary computer architectures and disposable electronics, to diagnostic tools for genetically driven medicines. However, in this thesis, we will restrict ourselves to discussions of devices, and will not talk about circuits and architectures which are also important and start to draw more attention in these days [40].

It may also be necessary to disclaim that in the following categories the author is not intending to cover all the topics, but those which has a relevance with this thesis

work.

1.1.3.1 Molecular spintronics

Molecular spintronics is a new emerging field combining molecular electronics and spin electronics. Over the past few decades, the impending need for smaller storage devices and higher speed magnetic field sensors has led to a growing interest in spintronics (spin electronics). The central theme of spintronics is the active manipulation of spin degrees of freedom in addition to the charge in solid state systems [41]. The discovery of the giant magnetoresistance (GMR) effect [42] has led to the present generation of read/write heads for magnetic data storage impacting on a multibillion industry. However, in order to achieve the target of one Tb/in², a further improvement of the sensitivity of the read/write heads is needed. Researchers are trying to devise ways to decrease the size of features, appealing to the increasing need for high density magnetic storage, high efficiency magnetic random access memory (MRAM) and design of quantum computers. But it is not until recently that organic molecules started to play a role in spintronics. Xiong et al. [43] reported low-temperature giant magnetoresistance effects as large as 40% using an organic semiconductor (8-hydroxyquinoline aluminum or Alq3) as the spacer layer in a spin-valve structure. They also showed the spin-up or spin-down alignment of electrons was maintained when power was shut off - a property essential for spintronic computer memory. Spin-valve effect in magnetic tunnel junctions using a self-assembled-monolayer of

octanethiol as the spacer was reported experimentally by Ralph’s group [44]. The driving idea behind molecular spintronics is that the spin-orbit and hyperfine interactions are very weak in organic molecules being composed mostly of carbon atoms [45]. It suggests extremely long spin relaxation times in these systems, just as found in carbon nanotubes [46]. Unfortunately, although nothing stands out that this idea should not work, very few experiments have been reported so far. But before experimentalists can address all of the challenges in experiments, like the control and characterization of the metal-molecule interface, the injection and detection of spin-polarized electrons, etc., theoretical work took the initiative and started to explore the possibility of having molecular spin valves using a small prototype molecule like BDT (benzene-1-4-dithiolate molecule) [47, 48, 49, 50], an atomic wire [51] and even a small biomolecule like a short DNA molecule [52]. But the role of molecules, the effect of the metal-molecule interface as well as the spin injection/detection mechanism are still questions of great interest, which may lead us to a theory guided-approach to the design of molecular spintronic devices.

1.1.3.2 Molecular electronics in biology

Another emerging field of research aims at joining biology and nanotechnology. There are two beneficial ways: use of molecular electronics in biology and use of biomolecules in molecular electronics. Probably it is a good reminder that the idea of molecular electronics was actually initiated not by physicists or engineers, but by a great bio-

chemist Albert Szent-Györgyi in pointing out the importance of charge transfer in biological reactions [10]. Now we can apply molecular electronic techniques to tackle biological problems, especially those involving electron transport properties of biosystems. A better understanding of this will help us to understand better how our living bodies work and how to learn from our creator and mimic biological systems in real-life applications.

Recently, there has been couples of experimental studies to assess the transport properties of DNA by means of electrical transport measurements. Nonetheless, the conclusions were quite controversial, ranging from insulator [53], conductor [54, 55, 56], semiconductor [57, 58, 59], to superconductor [60]. It seems by experiments alone, the problem cannot be settled, because of the various issues that are out of control in experiments. Some theoretical work has been performed on DNA molecules to infer their conductivity by exploring the electronic structure [61, 53] and the effective coupling between stacked bases [62]. Gutierrez *et al.* calculated the transmission functions and the $I - V$ characteristics using model Hamiltonians [63]. More recently, Rocha took into account specifically the effect of electrodes and did fully ab initio transport calculations on short DNA molecules [45]. The question, however, remains elusive whether or not this important biomolecule is able to conduct electrical charges over a large length scale.

DNA sequencing is another old, but still active research field because of the need of cheaper and faster sequencing schemes to make genome-based medicine and per-

sonalized medical treatment possible. It was recently suggested [64] that one could embed electrodes in the walls of a solid-state nanopore allowing electronic tunneling of translocating molecules that are linearized and confined in a nanopore, like a single-stranded DNA (ssDNA). Following that, theoretical simulations were done to calculate the transverse electronic current through ssDNA [65]. The time-dependent currents are found to be greatly influenced by the uncertainty of the orientation and structural fluctuations of the nucleotide within the nanopore [66]. The researchers suggested that one use a transverse field greater than the longitudinal pulling field to stabilize the motion of nucleotides and resolve the overlap in the distribution of currents by using statistical analysis and pre-calibration of device. The favorability of using this molecular electronics approach for rapid DNA sequencing was shown in a more recent study by considering the influence of environment and probes [67].

Using biomolecules as electronic components is an intriguing route to molecular electronics. On the one hand, it enables the exploitation of the natural self-assembly and self-recognition properties of these molecules. For example, in the DNA double helix, Guanine is only bound to Cytosine, and Thymine to Adenine specifically. On the other hand, biomolecules are particularly promising components, because of their unique functions, such as binding, catalysis, ion-pumping, sensing and self-assembly [38]. By and large, there are two directions: biomolecular devices and biosensors.

G. Maruccio *et al.* succeeded in the fabrication of a prototype field effect transistor (FET) based on a modified DNA base [68]. This guanosine-based FET operated at

ambient conditions and exhibited a voltage threshold for the conduction which could be modulated by the gate voltage. The electrical characteristics were explained in terms of resonant tunneling. The shift in the threshold voltage, which is defined by the alignment between the molecular minibands and the Fermi level in the electrodes, was related to a modification of the molecular minibands induced by the gate voltage. More recently, a protein field-effect transistor (Pro-FET) based on the blue copper protein azurin was reported by the same group operating at ambient conditions [69]. Electron transport through the device was proposed to occur through hopping from one reduced (Cu (I)) protein to an adjacent oxidized (Cu(II)) protein; followed by the reversible redox reaction which continuously reconverts the oxidized state Cu(II) into the reduced state Cu(I).

The integration of biomolecules (e.g. enzymes, nucleic acids, or antigens/antibodies) with carbon nanotubes (CNT) enables the use of these hybrid systems as active field-effect transistors or biosensor devices (enzyme electrodes, DNA sensors, or immunosensors) [70]. The solid state gate is replaced by nearby molecules that modulate the nanotube conductance when biorecognition events or biocatalytic processes occur. Experiments have shown the source-drain current dependence on the gate voltage of the biomolecule-functionalized CNTFET showed significant change upon the binding of analyte biomolecules [71, 72]. The mechanism of the effect was discussed in terms of the charge redistribution at the nanogate upon binding of charged molecules [71, 73], but remains to be fully understood theoretically for binding of uncharged

molecules [74].

Molecular electronics has shown a great potential as an alternative of semiconductor electronics, because of the small dimension of molecules, their uniformity in structural and electronic properties, ease of fabrication and the large variety of configurations, which may only be limited by our imagination. These studies have also opened dimensions for new device physics and new device design. Theoretical modeling played a key role in the invention and conceptual development of molecular electronic devices. It continues to provide indispensable understanding of the underlying transport mechanism at such a small scale, and establish the correlation between the structural and electronic properties of the molecular system with its transport properties, which may provide basic guidelines in a purpose-driven design in molecular electronics. This work is dedicated to theoretically exploring this possibility. But before we move on to the specific features of molecular electron transport, I would rather start with an overview of the transport schemes applied at different dimension scales. The simple reason is that we are using "assumptions" and "approximations" in almost every modeling/simulation to a physical problem. The scale of interest determines its validity. And it is also good to see the "connections" of different scales.

1.2 Transport Theories

In 1924, Louis-Victor de Broglie formulated the de Broglie hypothesis, claiming that all matter, not just light, has a wave-like nature; he related wavelength, λ , and momentum, p by $\lambda = h/p$, where h is the Planck constant. As a central concept of quantum mechanics, duality addresses the inadequacy of conventional concepts like "particle" and "wave" to fully describe the behavior of quantum objects. Electrons, without exception, have wave-particle duality. However, whether their wave character is pronounced depends on the scale of properties that one is interested in. Different theoretical models have been developed to address the electron transport at different scales (see Fig. 1.1).

1.2.1 Drift-diffusion transport: Fluidic current

If the dimension of a conductor is much larger than the de Broglie wavelength of its electrons, the electrons are seen as "particles". The transport property falls into a semiclassical picture, where electric current is described as the flow (movement) of electrons, which are electric charge carriers. When electric current in a material is proportional to the voltage across it, the material is said to be "ohmic", or to obey Ohm's law. A microscopic view suggests that this proportionality comes from the fact that an applied electric field superimposes a small drift velocity on the free electrons in a metal, for example. The current density (electric current per unit area, $J = \frac{I}{A}$)

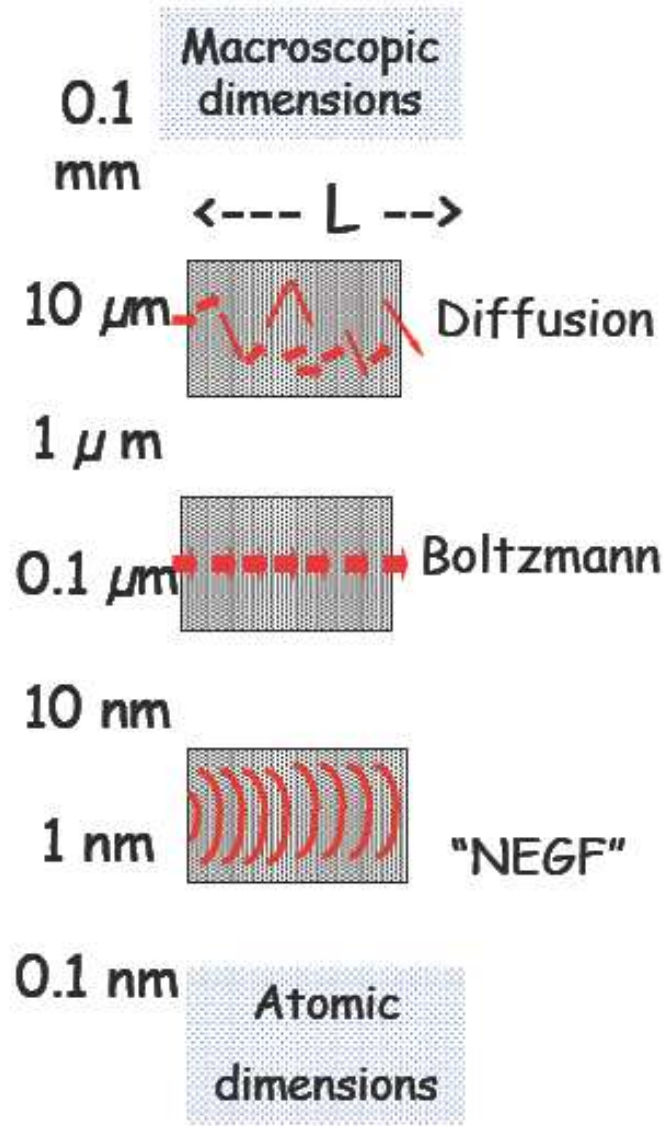


Figure 1.1: Paradigms of transport theories spanning from macroscopic to atomic scales [75].[†]

can be expressed in terms of the free electron density as

$$J = nev_d \quad (1.1)$$

[†]Reprinted with permission from S. Datta, Online Lecture Notes: Concepts of Quantum Transport I - Nanodevices and Maxwell's Demon, <http://www.nanohub.org/resources/2041>.

where n is free electron density, and v_d is the drift velocity. The drift velocity is related to the electron speed, which can be approximated by the Fermi speed: $v_F = \sqrt{\frac{2E_F}{m}}$ (usually in the order of 10^6 m/s for metals).

$$v_d = \frac{eE}{m} \cdot \tau = \frac{eE}{m} \cdot \frac{d}{v_F} \quad (1.2)$$

where E is the external electric field, m is the electron mass and τ the characteristic time between collisions. It can be calculated from the mean free path of an electron in the metal d divided by the Fermi speed v_F . From Ohm's law $J = \sigma E$, the conductivity of the material can be expressed by

$$\sigma = \frac{ne^2d}{mv_F} \quad (1.3)$$

This is only valid when the dimension of the conductor is much larger than the mean free path of electrons in this material. For ordinary currents, this drift velocity is on the order of millimeters per second in contrast to the speeds of the electrons themselves which are on the order of a million meters per second. Even the electron speeds are themselves small compared to the speed of transmission of an electrical signal down a wire, which is on the order of the speed of light, 300 million meters per second.

The electrons are actually not "free" in solids with periodic lattices. To understand electronic properties of solids, one needs to describe the behavior of the valence elec-

trons in the presence of the internal potentials due to the lattice as well as external potential due to any applied voltage. This is, in general, a many-body problem. Fortunately, most of the phenomena in transport can be described using a one-electron description. One can treat the system quantum mechanically and calculate the band structure (energy vs. k -vector) of solids very easily these days, based on the time-independent density functional theory (DFT). The one-electron wavefunction in the crystalline periodic potential can be written as $\psi(\vec{r}) = e^{i\vec{k}\cdot\vec{r}}u_k(\vec{r})$, the well-known Bloch theorem. Nonetheless, in semiconductor transport theory, we again end up with a quasi-particle picture. Consider the motion of an electron in the crystal under the influence of an applied electric field. The group velocity associated with the "electron wavepacket" is given by

$$v_g = \frac{d\omega}{dk} = \frac{1}{\hbar} \frac{dE}{dk} \quad (1.4)$$

Differentiate the expression for v_g with respect to time, and use Newton's second law, one can get

$$\frac{dv_g}{dt} = \frac{1}{\hbar} \frac{d}{dk} \left(\frac{dE}{dk} \right) \frac{dk}{dt} = \frac{1}{\hbar} \frac{d^2E}{dk^2} \frac{F}{\hbar} = \frac{F}{m^*} \quad (1.5)$$

where m^* is defined as the effective mass. It is shown to have the form:

$$\frac{1}{m^*} = \frac{1}{\hbar^2} \frac{d^2E}{dk^2} \quad (1.6)$$

In general, the effective mass tensor is

$$\frac{1}{m_{ij}^*} = \frac{1}{\hbar^2} \frac{\partial^2 E}{\partial k_i \partial k_j} \quad (1.7)$$

So, to a first-order approximation, the entire effect of the periodic crystal potential is to replace the free electron mass with an effective mass. Electrons transport as quasiparticles, but with a mass different from that of free electrons. In case of a negative effective mass (a nearly full energy band curve in a concave shape), it can be considered as a positive particle of positive mass that is accelerated in the direction of the field, called a hole. The velocity and momenta of the holes are those corresponding to the unoccupied states in the band. Effective mass is a very important characteristic parameter for semiconductors, which in turn determines the mobility of electrons (holes as well), thereby the conductivity of the material.

1.2.2 Boltzmann equation: Particle-based semiclassical transport

Doping plays a central role in semiconductor electronics. The electrical resistivity from impurity scattering is easily derived by using the Boltzmann transport equation [76]. In the Boltzmann theory, the electrons are described by a classical distribution function $f(\vec{r}, \vec{p}, t)$, the probability of finding a carrier with crystal momentum \vec{p} at position \vec{r} at time t . The time rate of change of this distribution function is governed

by the Boltzmann equation

$$\frac{\partial f}{\partial t} + \vec{v} \cdot \nabla_r f + \vec{F} \cdot \nabla_p f = \left(\frac{df}{dt}\right)_{collisions} \quad (1.8)$$

where \vec{v} is the velocity of electrons, \vec{F} is the force field acting on electrons, and the term on the right hand side is the time rate of change due to collisions with the impurities or phonons. The electrical current density

$$J = ne \langle \vec{v} \rangle = e \int \frac{d^3 k}{(2\pi)^3} f(\vec{k}) \frac{\hbar \vec{k}}{m} \quad (1.9)$$

where the product of the electron density n and the average velocity $\langle \vec{v} \rangle$ is obtained by averaging over the electron distribution $f(\vec{k})$. The solvation of the Boltzmann transport equation is usually done by Monte-Carlo simulations.

Limitations of the Boltzmann transport equation are as follows [77]. First, semiclassical treatment of carriers as particles having well defined positions and momenta, obeying Newton's law. According to the Heisenberg uncertainty principle, this is only applicable when the mean free path is longer than the thermal de Broglie wavelength ($\lambda_B = \frac{\hbar}{\sqrt{2m^* k_B T}}$, usually in the order of 100-200 Å for most common semiconductors), and slow variation of potentials over distance comparable to λ_B (no quantum mechanical reflections at the barrier). Secondly, it is a statistical description of a many-particle system. This means that this transport scheme might break down if there are few carriers in the system. Thirdly, correlations between carriers are

neglected - no scattering/collision between electrons is considered.

1.2.3 Quantum transport: Wave-like characted electrons

Nevertheless, these conditions may be strongly violated when the size of the conductor is reduced to the order of the de Broglie wavelength of electrons. As such, the wave-like character of electrons become dominant. We have to be rescued by quantum mechanics. Because waves are non-local, all objects are non-local too (exist in many places at once) . Under the Heisenberg uncertainty principle, the electrons do not have well defined position or momentum. The use of the classical distribution function is not suitable any more above the classical limits. Secondly, in mesoscopic systems, the confining (or quasi-confining) dimensions of these structures, are of the order of the De Broglie wavelength of the electrons, so that energy quantization occurs. Confined electrons occupy discrete energy levels instead of a quasi-continuous energy band. Thirdly, the quantum-phase coherence is preserved over a length with size comparable to that of the sample, and the interference effect between different electron waves, or differing electrons on their individual trajectories become important. Lastly, the interface between the electrode and the conductor, e.g. a molecule, will also play a significant role in the electron transport [78, 79]. For a more detailed discussion, see the lecture notes from Goodnick and Vasileska [80].

Electrons are seen as waves extending from one electrode to the other. The transport

of electrons is now the scattering of electrons under the potential of the atomic nuclei and the potential due to other electrons, as well as the external bias-induced potential. The semiclassical Boltzmann equation has made the assumption that carriers do equilibrate with the underlying thermal fluctuations, while it is not true in mesoscopic and molecular transport, where the carrier equilibration occurs almost exclusively within the contact reservoirs and the transition across the device is mostly coherent [28, 81].

The current through a conductor is expressed in terms of the *probability* that an electron can transmit through it [82]. In other words, the conductance of a sample is proportional to the ease with which electrons can transmit through it. It seems to be a natural choice, but indeed it is also a big step from a microscopic particle view in describing currents to a quantum mechanical view in describing conductance based on electron transmission coefficient.

Landauer first related the linear response conductance to the transmission probability [83, 84]. Shortly after that, Büttiker extended the approach to describe multi-terminal measurements in magnetic fields [85, 86]. This formulation (generally referred to as the Landauer Büttiker formalism) has been widely used in the interpretation of mesoscopic experiments. Here the total current is expressed as

$$I = \frac{2e}{h} \int_{-\infty}^{\infty} T(E, V) [f(E, \mu_1) - f(E, \mu_2)] dE \quad (1.10)$$

where h is Planck constant; e is the charge of an electron; μ_1 and μ_2 are the electrochemical potentials of the left and right electrodes under an external bias V , respectively; $f(E)$ is the Fermi-Dirac distribution function; a prefactor of 2 is used to take into account the spin degree of freedom. The transmission function $T(E, V)$ describing the quantum mechanical transmission probabilities for electrons, determines electron transport properties unambiguously. Generally speaking, it depends not only on the electron energy E but also upon the applied external bias V .

Molecular electronics has triggered intensive studies on the quantum transport theoretical schemes. A multitude of theoretical methods are available in calculating the $I-V$ characteristics. More specifically, three approaches have been used in the studies presented in this thesis.

- *Bardeen, Tersoff and Hamann Formalism* (based on Tunneling Hamiltonian method)

It is applicable to weakly-coupled systems. Nowadays, it is widely used in the interpretation of STM images, where there is usually a significant vacuum between the probing tip (as one of the electrodes) and the sample. We have applied this approach to the study of organic spin valves in a setup analogous to STM experiments (Chapter 3).

- *Landauer-Büttiker Formalism*

It is used for strongly-coupled systems, but only applicable to small bias voltages

within the linear response regime. Despite the lack of rigorous determination of Fermi level, this method provides a simple and straightforward way of calculating the transmission function as well as the conductance of the system. It is still widely used for large-scale ballistic and multi-terminal transport calculations. We have applied this approach to the study of the GMR effect in a realistic candidate C_{60} strongly coupled to two Au electrodes (Chapter 4); and the study of unimolecular diodes and transistors (Chapter 5).

- *Non-equilibrium Green's Function (NEGF) method*

This is the state-of-the-art and most general approach. It can treat a system far from equilibrium by including the exact treatment of an external potential and solving the Poisson's equation self-consistently. We have applied this approach to the study of fast DNA sequencing by embedding functionalized electrodes in a nanopore (Chapter 6).

These methods will be discussed in detail in the next chapter.

Chapter 2

Theoretical Methods

Throughout this thesis, we are going to consider typically two-terminal electronic devices. An illustration of such a device is shown in Fig. 2.1, where a molecule is sandwiched between two electrodes. When no bias is applied across the two electrodes, the electrode-molecule-electrode system is in equilibrium having a common Fermi level, and no current flows through it. When we apply an external bias voltage V to the electrodes (e.g. using a battery), two different electrochemical potentials μ_1 and μ_2 are maintained at the left and the right electrodes ($\mu_1 - \mu_2 = eV$), driving the channel into a non-equilibrium state and electrons flow from the left electrode to the right. The two metallic contacts are seen as connecting to big electron reservoirs, which are semi-infinite in principle. Far away from the contacts, they are in the state of local equilibrium with electrons following the Fermi-Dirac distribution, but around

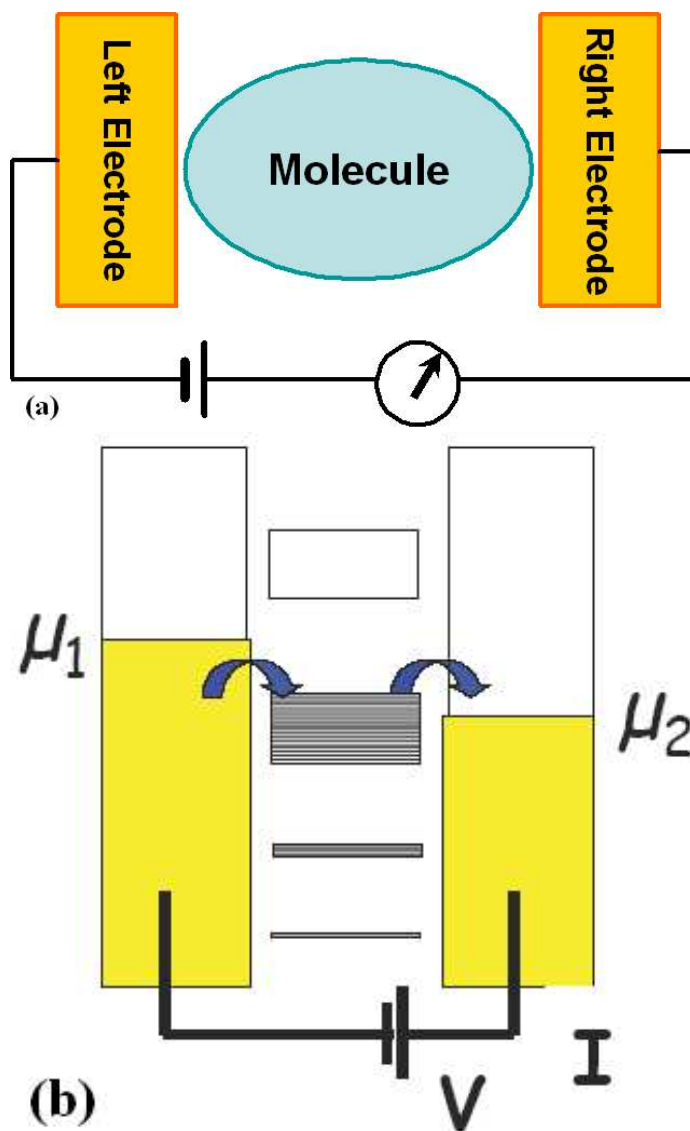


Figure 2.1: Illustration of (a) a two-terminal molecular electronic device, and (b) electron current flow under a bias of V with the electrochemical potentials at the left and the right electrodes maintained at μ_1 and μ_2 , respectively [75].[†]

two different electrochemical potentials μ_1 and μ_2 . For metals, they usually have continuous energy levels. However, the molecule(s) in between has discrete energy

[†]Figure 2.1(b) is reprinted with permission from S. Datta, Online Lecture Notes: Concepts of Quantum Transport I - Nanodevices and Maxwell's Demon, <http://www.nanohub.org/resources/2041>.

levels.

There are two distinct features of molecular electronic devices. (1) the effect of the electronic structure and (2) the effect of the interface to the external contact. Since the molecule can freely exchange energy and electrons with the electrodes, a rigorous treatment of molecular electronic device can only be achieved including these effects in the context of an open system. As a result, a successful modeling of molecular electronic devices in general calls for combining the theory of quantum transport and the theory of electronic structure starting from first principles [81].

2.1 Coherent Electron Transport

Broadly speaking, there are a variety of transport mechanisms for molecular electronic devices [87]. For small molecule constituted devices working at low biases and low temperatures, however, coherent transport is dominant. The studies in this thesis work fall into this category. We will exclusively talk about this transport mechanism and its application throughout this thesis. Many of the following discussions of theory and equations are adapted from Supriyo Datta's book on "Electronic transport in mesoscopic systems" [82].

As suggested by its name, in coherent transport, a wave-like electron transverses the device without losing its phase and the exchange of energy for getting into equi-

libration occurs exclusively within the contact reservoirs. In other words, it is a non-dissipative transport.

As one of the characteristic lengths in transport, phase relaxation length defines the distance that an electron travels before it changes its phase. The transport is coherent when the length of the conductor (one-dimension device) is smaller than the phase relaxation length. There are three common sources for phase-breaking relaxation: a dynamic scatterer like lattice vibration (phonons), electron-electron interactions and impurities having internal degree of freedom like magnetic impurities with an internal spin. So basically, rigid scatterers do not contribute to phase-relaxation, while only fluctuating scatterers can.

2.1.1 Tunneling Hamiltonian formalism

The tunneling Hamiltonian formalism is now widely used to describe tunneling processes involving electron transfer between two electrodes separated by a thick barrier, which can be an insulator as in a tunneling junction, or a vacuum in a scanning tunneling microscopy (STM) experiment. The electron transport is treated in terms of electronic transitions between weakly coupled reservoirs. This paradigm is first illustrated by Bardeen in his seminal paper in 1961[88]. Assuming a barrier with a thickness of t_b between the left and right electrode, we consider two many-particle states of the entire system, Ψ_0 and Ψ_{mn} , which differ in the transfer of an electron

from the left to the right. We suppose that Ψ_0 and Ψ_{mn} may be defined in terms of quasi-particle occupation numbers of left and right electrodes, so that Ψ_{mn} differs from Ψ_0 in the transfer of an electron from state m in the left to state n in the right. A time-dependent solution can be constructed as a linear combination of Ψ_0 and various final states, Ψ_{mn} ,

$$\Psi = a(t)\Psi_0 e^{\frac{-iE_0 t}{\hbar}} + \sum_{mn} b_{mn}(t)\Psi_{mn} e^{\frac{-iE_{mn} t}{\hbar}} \quad (2.1)$$

By substituting into the Schrödinger equation, the matrix element for the transition is given by

$$M_{mn} = \int_L [\Psi_0^* H \Psi_{mn} - \Psi_{mn} H \Psi_0^*] d\tau \quad (2.2)$$

where the subscript L indicates that the integration is to be taken over the region to the left of the barrier. This can be further reduced to a surface integration [89]

$$M_{mn} = -\frac{\hbar^2}{2m} \int [\Psi_0^* \nabla \Psi_{mn} - \Psi_{mn} \nabla \Psi_0^*] \cdot d\vec{S} \quad (2.3)$$

where the integral is over any surface lying entirely within the barrier region separating the two sides. The form of the matrix element is closely related to the current density operator J by the relation

$$M_{mn} = -\frac{\hbar}{e} J_{mn} \quad (2.4)$$

The tunneling current is often calculated in terms of the wave functions determined

separately for each electrode in the absence of the other [89, 90]. By first-order perturbation theory, the current is expressed as

$$I = \frac{4\pi e}{\hbar} \sum_{\mu\nu} f(E_\mu)[1 - f(E_\nu + eV)]M_{\mu\nu}^2\delta(E_\mu - E_\nu) \quad (2.5)$$

where $f(E)$ is the Fermi function, V is the applied voltage, $M_{\mu\nu}$ is the tunneling matrix element between states ψ_μ of the left electrode and ψ_ν of the right electrode. In a similar fashion as in Bardeen's treatment, it can be written as

$$M_{\mu\nu} = -\frac{\hbar^2}{2m} \int d\vec{S} \cdot [\psi_\mu^* \nabla \psi_\nu - \psi_\nu \nabla \psi_\mu^*] \quad (2.6)$$

The calculation of the exact value of $M_{\mu\nu}$ still demands knowledge of atomic details of the surface and probe in case of a STM experiment. A reasonable approximation based on surface wave function expansion in a form of Bloch function with exponential decay into the vacuum (barrier) and tip wave function in an asymptotic spherical form [89, 90] leads to a simple form of current, called Bardeen, Tersoff and Hamann formalism (BTH)

$$I = \frac{4\pi e}{\hbar} \gamma \int_{-\infty}^{\infty} \rho_s(E + \frac{eV}{2}) \rho_t(E - \frac{eV}{2}) e^{-2d\sqrt{\frac{2m}{\hbar^2}(\phi_{av} - E)}} \{[f(E - \frac{eV}{2})[1 - f(E + \frac{eV}{2})]] - [f(E - \frac{eV}{2})[1 - f(E + \frac{eV}{2})]]\} dE \quad (2.7)$$

where $\rho_{s,t}$ is the sample and tip density of states respectively, d is the distance of

the tip from the sample surface, V is the applied bias voltage, E is the injection energy of the tunneling electron, ϕ_{av} is the average work function of the sample and tip, f is the Fermi distribution function. To match the respective electrochemical potentials of two electrodes at equilibrium (zero bias), the Fermi energies are aligned and taken to be the reference energy. The exponential decaying factor assumes a rectangular vacuum potential barrier and uses WKB (Wentzel-Kramers-Brillouin) approximation to obtain the transmission coefficient. The probabilities of tunneling of electrons from the sample to the tip, and from the tip to the sample at finite temperature are explicitly taken into account by the inclusion of the term involving Fermi distribution functions in the equation. γ , a proportionality constant, is assumed to be 1, giving a physical meaning to the calculated tunnel current within the error allowed in the s -wave model approximation of Tersoff-Hamann. Essentially, in this simple approximation, the tunneling current represents the integral of convolution of the tip density of states (DOS) with the sample density of states at the tip position. So the difference in the DOSs of samples can be reflected in the detecting currents. Vice versa, tunneling experiments have also been used as a probe for the density of states in unknown materials.

2.1.2 Landauer-Büttiker formalism

The Landauer-Büttiker formalism treats the transport of electrons as a scattering problem from one electrode to the other, and the transmission T becomes the relevant quantity. Electrons in a metallic electrode usually fill out continuous energy levels following the Fermi-Dirac distribution at local equilibrium. After applying an external bias voltage, electrons propagate through the transverse channel or modes of the molecule, which has discrete energy levels. If we consider the case of zero temperature and assume there are N channels in the range of $\mu_1 > E > \mu_2$ (Note that in a strongly-coupled electrode-molecule-electrode system, there may not be a clearcut for the number of channels.) having the same transmission coefficient of T_1 for each channel, then the current

$$I = \frac{2e}{h} N T_1 (\mu_1 - \mu_2) = \frac{2e^2}{h} N T_1 V \quad (2.8)$$

This is called the Landauer formalism. And it in turn gives the conductance

$$G = \frac{2e^2}{h} N T_1 \quad (2.9)$$

Now an interesting phenomenon to see is that even though one has a perfect conductor (ballistic transport having no scattering in the conductor) with transmission coefficient $T_1 = 1$, the conductance is still a finite value $\frac{2e^2}{h} N$ for a small-width sample

where the transverse channel N is a finite number. The causal resistance is called contact resistance, which seldom causes attention in macroscopic or even microscopic devices because it is usually negligibly small. It arises from the interface between the molecule and the contacts. The current is carried in the contacts by infinitely many transverse channels, but inside the molecule by only a few channels. This requires a redistribution of the current among the current-carrying channels at the interface leading to the interface resistance. In the case of one channel available only, one has the conductance

$$G = \frac{2e^2}{h} \quad (2.10)$$

which implies a resistance of $R = 1/G = 12.9k\Omega$. This quantity of conductance is called *quantum conductance*. It was first observed in metallic point contact [91], then in semiconductors when the width of the constriction was reduced [92, 93]. The conductance quantum was measured for a molecular system for the first time in 1998 when a multiwalled carbon nanotube, glued to a conducting AFM tip, was lowered into liquid Hg at room temperature [28]. In these experiments, as one increase the voltage, the conductance increases by discrete steps of a quantum conductance.

The conductance formula $G = \frac{2e^2}{h}NT_1$ clearly shows that scatterers of the molecule give rise to resistance by reducing the transmission coefficient T_1 . Under the linear response assumption and the validity of Ohm's law, conceptually one can differentiate the total resistance into two parts, the contact resistance G_C^{-1} which is intrinsic to

any narrow conductor (like a molecule) due to the size constriction in series with the actual resistance of the molecule G_S^{-1} .

$$G^{-1} = \frac{h}{2e^2NT_1} = \frac{h}{2e^2N} + \frac{h}{2e^2N} \frac{1 - T_1}{T_1} \quad (2.11)$$

with the first term equals to G_C^{-1} and the second G_S^{-1} . We can see that the value of G_S^{-1} is totally determined by the transmission properties of the molecule connecting to two electrodes. From this partition, it is good to see the role of the molecule as a conducting bridge. However, it is somehow misleading to spatially associate G_S^{-1} with the molecular part of the system, which may lead to the conclusion that the Joule heat I^2/G_S associated with this resistance is dissipated in the molecule. This may have catastrophic consequences that the high current density in the molecular system (10^9 A/m²) will burn it up. So it is worthwhile to point out the conceptual difference in the transport scheme at such a molecular scale. In coherent transport, electrons are not coupled to phonons. The scatterers remain rigid and elastic, having no internal degree of freedom to dissipate energy. Instead, the dissipation of energy occurs in the electrode reservoirs.

The transmission function $T = NT_1$ in general can be obtained by knowledge of the molecular orbital energy levels and their coupling to the two electrodes. In the case of non-zero temperature, electrons in the two electrodes are in the state of local equilibrium following the Fermi-Dirac distribution $f(E)$ at an electrochemical potential

of μ_1 and μ_2 respectively. The total current can be written as

$$I = \frac{2e}{h} \int_{-\infty}^{\infty} T(E, V) [f(E - \mu_1) - f(E - \mu_2)] dE \quad (2.12)$$

(which was briefly presented in Chap 1.) The transmission function T varies with both the energy E and the external bias V .

Büttiker extended this approach to describe multi-terminal measurements. For multi-terminal devices, the tunneling current is expressed as (different terminals are indexed by p and q having different electrochemical potentials)[83, 86, 82]

$$I_p = \int i_p(E) dE$$

$$i_p(E) = \frac{2e}{h} \sum_q [T_{q \leftarrow p}(E) f_p(E) - T_{p \leftarrow q}(E) f_q(E)] \quad (2.13)$$

where $T_{q \leftarrow p}(E)$ represents the total transmission from terminal p to terminal q at the energy E and $f_p(E)$ is the Fermi function for terminal p having an electrochemical potential of μ_p . In the case of two terminals, since the current is zero at zero bias ($\mu_1 = \mu_2$), the transmission functions have the relation $T_{12} = T_{21}$. Again we come back to the same expression as the Landauer formalism in Eqn. 2.12.

The Landauer-Büttiker formalism is widely used in the coherent regime without worrying about the exclusion-principle effect. As Datta has also pointed out that it is applicable to incoherent transport too if the vertical flow of electrons from one energy

level to the other is negligible.

Now the key in coherent transport comes to the calculation of transmission function T .

2.1.3 Green's function (GF) method

The system of a transport problem is an open system, with a center scattering region and two semi-infinite electrodes. Such a problem can be tackled by the Green's function method.

The Green's function describe the response at a point due to the excitation at any other. In an electrode-molecule-electrode system, the Hamiltonian of the entire system is written as [94]

$$H = H_1 + H_2 + H_S \quad (2.14)$$

where H_1 , H_2 and H_S are the Hamiltonians of three separate sections: the left, right electrodes and the molecule. The retarded Green's function can be defined by the usual relation

$$G^R = [ES - H + i\eta]^{-1} = [ES - (H_1 + H_2 + H_S) + i\eta]^{-1} \quad (2.15)$$

where S is the overlap matrix of wavefunctions in case of orthogonalization is not satisfied. An infinitesimal imaginary part $i\eta$ ($\eta > 0$) is added to the energy in this

equation to incorporate the boundary conditions for a retarded Green's function which corresponds to outgoing waves from the excitation point. This imaginary part makes the advanced Green's function G^A grow indefinitely as it moves away from the point of excitation, and leaves the retarded Green's function the only acceptable solution. Similarly we can work out for the advanced Green's function by introducing a negative infinitesimal imaginary part in the energy. But it is easily shown that

$$G^A = [G^R]^+ \quad (2.16)$$

i.e. G^A is the Hermitian conjugate of G^R .

If we could write down the form of the Hamiltonian, then it seems to be trivial to work out the corresponding Green's function for the whole system, which is only the inverse of the H matrix. But we are really dealing with a system with infinite size of H matrix, because the sizes of $H_{1,2}$ matrices of electrodes are infinite. Assuming the coupling between the left/right electrode with the scattering region is C_{1S}/C_{2S} and no coupling between two electrodes, then one can partition the whole Green's function G^R into three parts (superscript label of R is removed for simplicity in the

rest of this thesis)

$$\begin{pmatrix} G_1 & G_{1S} & G_{12} \\ G_{S1} & G_S & G_{S2} \\ G_{21} & G_{2S} & G_2 \end{pmatrix} = \begin{pmatrix} ES + i\eta I - H_1 & C_{1S} & 0 \\ C_{1S}^+ & ES - H_S & C_{2S}^+ \\ 0 & C_{2S} & ES + i\eta I - H_2 \end{pmatrix} \quad (2.17)$$

Then it is possible to derive an explicit expression for the sub-matrix G_S

$$\begin{aligned} G_S &= [ES - H_S - C_{1S}^+ g_1 C_{1S} - C_{2S}^+ g_2 C_{2S}]^{-1} \\ g_1 &= [ES + i\eta I - H_1]^{-1} \\ g_2 &= [ES + i\eta I - H_2]^{-1} \end{aligned} \quad (2.18)$$

The last two terms on the right hand side of the first equation are often referred as self-energies due to the electrodes

$$\begin{aligned} \Sigma_1 &= C_{1S}^+ g_1 C_{1S} \\ \Sigma_2 &= C_{2S}^+ g_2 C_{2S} \end{aligned} \quad (2.19)$$

which describes the semi-infinite effect of electrodes. This quantity can be calculated from the Green's function of the isolated electrodes $g_{1,2}$, which usually have periodic structures. It can be determined based on surface physics [95, 96], Bethe lattice model [97] or proper approximations [98]. So now we have a finite system to work on. And

the Hamiltonian $H_S + \Sigma_1 + \Sigma_2$ can be seen as an effective Hamiltonian of the system. But the solution of this Schrödinger equation $[H_S + \Sigma_1 + \Sigma_2]\psi = E\psi$ generates complex eigenenergies, because the self-energies are in general not Hermitian. However, constructing from the Green's function, we can get the spectral function

$$A = i[G_S - G_S^+] = G_S(\Gamma_1 + \Gamma_2)G_S^+ \quad (2.20)$$

where we have

$$\begin{aligned} \Gamma_1 &= i[\Sigma_1 - \Sigma_1^+] \\ \Gamma_2 &= i[\Sigma_2 - \Sigma_2^+] \end{aligned} \quad (2.21)$$

The quantity $\Gamma_{1,2}$ describes the coupling of the molecule to the electrodes. The diagonal elements of the spectral function $A(E)$ produce the local density of states (DOS)

$$\rho(E) = \frac{1}{2\pi}A(E) \quad (2.22)$$

If the coupling between the electrode and molecule is weak, the so-obtained DOS reproduces the eigenvalues of the isolated molecule. As increasing the coupling strength, the DOS peaks shift and broaden.

Using Green's function to construct the scattering states, from the Fisher-Lee relation [99], one can express the elements of the scattering matrix (S-matrix) in terms of the

Green's functions. As a result, the transmission function can be derived to a well compact form

$$T = Tr[\Gamma_1 G_S \Gamma_2 G_S^+] \quad (2.23)$$

where the trace runs over all the orbitals. The variation of $T(E)$ is closely correlated with the variation of $A(E)$ as a function of E .

2.1.4 Non-equilibrium Green's function (NEGF) method

The non-equilibrium Green's function (NEGF) method is a combination of the GF method with non-equilibrium statistics [100]. With this method, one could treat a system far from equilibrium in a self-consistent way by including the exact treatment of an external field, responsible for driving the system in a non-equilibrium condition. Such a self-consistent solution may be important in the evaluation of charge transfer at the metal/molecule interface, electrostatic potential profiles, band alignment and current induced forces, etc. [81].

In the coherent transport scheme, actually we do not need to change anything in the formalism of transmission and current described in the last two sections. The retarded Green's function describes the coherent evolution of an electron from the moment it is injected till it loses coherence either by disappearing into a lead or by scattering into a different state (due to electron-phonon or electron-electron interactions) where a new coherent trajectory is initiated. It is only when we want to

consider interaction-involved (electron-phonon, electron-electron or strong correlation interactions) transport processes that a more general formulation is required. Since our interest is confined to coherent transport through this whole thesis work, we will skip the delicate derivation of the NEGF formalism, but rather focus on the self-consistent scheme provided by the NEGF, which is equally important in the rigorous coherent transport calculation.

The Hamiltonian of the central scattering region H_S depends on the density matrix of the system, which in turn, is determined by the Hamiltonian. Due to the presence of the leads and the external bias voltage, the electron occupation number in a state is different from that of the equilibrium population. So it is necessary to introduce such a quantity in order to calculate the actual density matrix of a non-equilibrium system. For this purpose, the NEGF method introduces the lesser Green's function $G_S^<$ to calculate the density matrix

$$\rho = \frac{1}{\pi i} \int G_S^<(E) dE \quad (2.24)$$

where a factor of 2 is multiplied to take into account the spin degeneracy. $G_S^<$ is also called correlation Green's function. In steady state problems as we are interested in, it is energy-dependent. The diagonal elements of $G_S^<$ account for the number of electrons occupying a particular state. It can be related to the retarded Green's function G_S

(superscript R is removed for simplicity) by the following form [100, 82, 101]

$$G_S^<(E) = iG_S(E)[\Gamma_1 f(E - \mu_1) + \Gamma_2 f(E - \mu_2)]G_S^+(E) \quad (2.25)$$

Note that $\mu_{1,2} = \pm \frac{eV}{2}$, $\Gamma_{1,2}$ stands for $\Gamma_{1,2}(E \pm \frac{eV}{2})$, and $G_S(E)$ is given by the Eqn. 2.18 by replacing $\Sigma_{1,2}(E)$ with $\Sigma_{1,2}(E \pm \frac{eV}{2})$ [96].

The integration in Eqn. 2.24 to obtain the density matrix ρ , however, is not trivial at all, since the integral is unbound and the Green's function has van Hooe singularities over the real energy axis. This problem is usually solved by adding/subtracting the term $G_S \Gamma_2 G_S^+ f(E - \mu_1)$ and partitioning the integral into two parts.

$$\begin{aligned} \rho &= \rho_{eq} + \rho_V \\ \rho_{eq} &= \frac{1}{\pi} \int [G_S \Gamma_1 G_S^+ f(E - \mu_1) + G_S \Gamma_2 G_S^+ f(E - \mu_1)] dE \\ &= -\frac{2}{\pi} \int \text{Im}[G_S] f(E - \mu_1) dE \\ \rho_V &= \frac{1}{\pi} \int G_S \Gamma_2 G_S^+ [f(E - \mu_2) - f(E - \mu_1)] dE \end{aligned} \quad (2.26)$$

ρ_{eq} represents the density matrix at equilibrium when both the electrodes have the same chemical potential of μ_1 , while ρ_V takes into account all the corrections from non-equilibrium conditions. The integration of ρ_{eq} can be performed on an equivalent contour in the complex plane to avoid the singularities [102, 96]. Although this is not applicable to ρ_V , its integration is limited over a finite energy range, mainly within

the two electrochemical potentials of the electrodes.

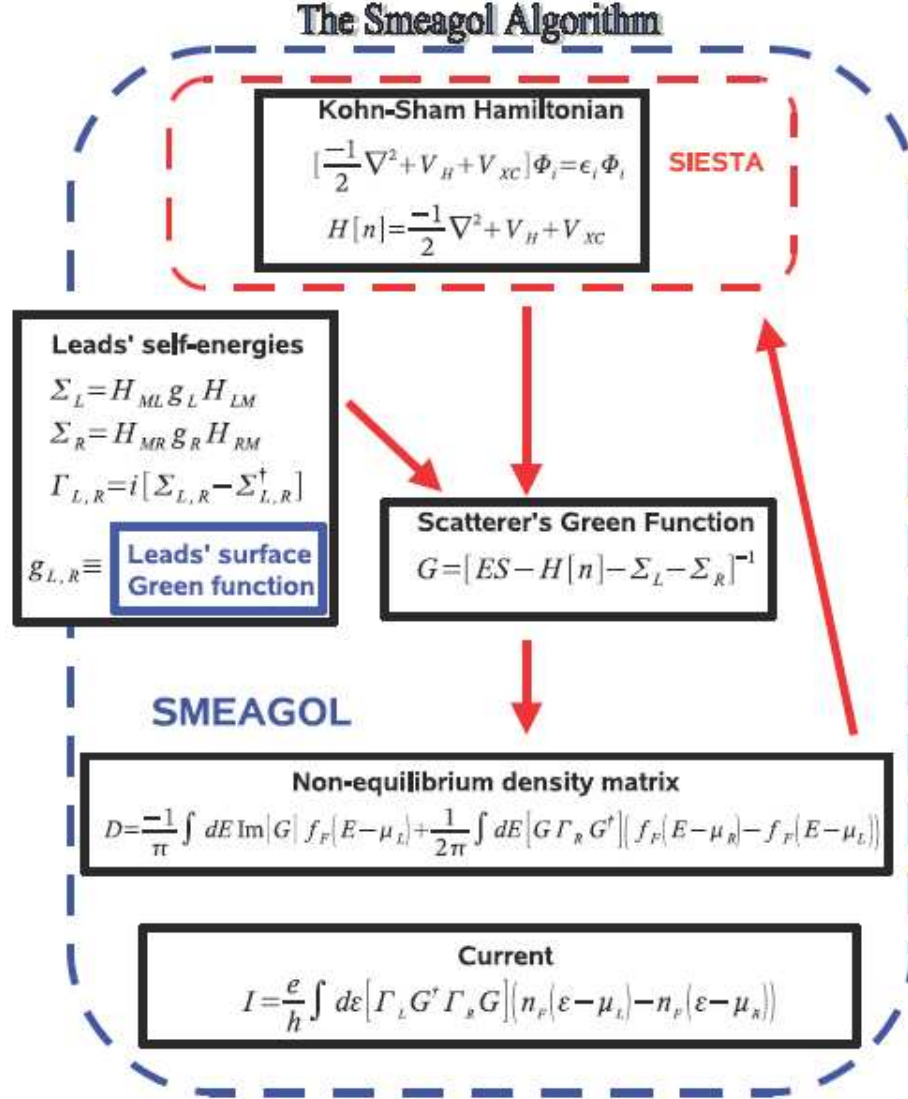


Figure 2.2: An example of the flow chart of the NEGF self-consistent procedure as implemented in an *ab initio* quantum transport code SMEAGOL based on the electronic structure code SIESTA [45].[§]

The self-consistent procedure is illustrated in the diagram of Fig.2.2. It shows similar

[§]Reprinted with permission from Alexandre R. Rocha, Ph. D dissertation: Theoretical and Computational Aspects of Electronic Transport at the Nanoscale, University of Dublin, Trinity College, Ireland (2007).

routes as in a self-consistent calculation from first-principles for a general equilibrium system. One starts from an initial guess of the density matrix, and this in turn gives the real-space charge density, which can be used to calculate the Hamiltonian. By incorporating the effect of the semi-infinite electrodes (self-energies from separate calculations of the electrodes), from the effective Hamiltonian of the center scattering region, one may calculate the new density matrix according to the NEGF method. Then one compares the difference between the new and old density matrix. If it is above certain criterion, one feeds in the new density matrix and continues the loop until the difference satisfies the criterion. Nonetheless, there are also unique things in this self-consistent procedure. Firstly, the way of calculating the density matrix is based on the NEGF method. We take a detour of the conventional diagonalization of the Hamiltonian. In such an approach, one needs to follow these steps: calculate the self-energy functions of the electrodes, calculate the retarded Green's function, then the correlation Green's function, and finally the density matrix. Secondly, there are two parts in the potential of the Hamiltonian. One is the exchange-correlation potential, which is common for density functional theory (DFT) based approach. The other is the Hartree (electrostatic) potential, usually obtained as a solution of the Poisson equation with proper boundary conditions given by the contact potentials. The Poisson equation can be solved either in real-space [103] or in k -space using the fast Fourier transform algorithm [104, 96].

The passage from a particulate Newtonian viewpoint to a wavelike Schrödinger view-

point is the "first quantization". Second quantization (the NEGF method) completes the formalism by incorporating both the particulate view and the wavelike view [105].

2.1.5 Beyond coherent transport

The NEGF formalism is needed to extend quantum transport models beyond the coherent regime. Phase-breaking scattering processes, like electron-phonon interaction, can be treated systematically in this quantum transport scheme by explicitly including the self-energy and the scattering functions due to these interactions [106, 107, 108]. Another merit of the NEGF method is its compatibility with many-body theory. In the case of electron-electron interaction, it is possible to evaluate the self-energy and scattering functions to higher orders using many-body perturbation theory [109]. We also know that the mean field theory breaks down in case of strongly correlated systems. The transport picture that is based on the single-particle wavefunctions is not suitable either in the interpretation of transport phenomena in these systems, e.g. the single-electron tunneling [35]. The NEGF method makes it possible to treat the system consistently using many-body theory such as the GW method [110].

2.2 Electronic Structure From First-Principles

When we consider a system down to the atomic or molecular scale, it is indispensable to treat the system quantum mechanically. The state of a many-body (including a number of electrons and/or nuclei) system can be described by a many-body wave function Ψ^{MB} . For a static problem, the wave function can be obtained by solving the time-independent Schrödinger equation

$$H^{MB}\Psi^{MB} = E^{MB}\Psi^{MB} \quad (2.27)$$

The wave-particle duality is fully incorporated in this equation. The quantum mechanical Hamiltonian of the system H^{MB} has the form:

$$\begin{aligned} H^{MB} = & \sum_i^{N_e} \frac{-\hbar^2}{2m_e} \nabla_{\vec{r}_i}^2 + \sum_I^{N_N} \frac{-\hbar^2}{2M_I} \nabla_{\vec{R}_I}^2 + \frac{1}{2} \sum_{I \neq J}^{N_N} \frac{e^2 Z_I Z_J}{|\vec{R}_I - \vec{R}_J|} \\ & - \sum_{i,I}^{N_e, N_N} \frac{e^2 Z_I}{|\vec{r}_i - \vec{R}_I|} + \frac{1}{2} \sum_{i \neq j}^{N_e} \frac{e^2}{|\vec{r}_i - \vec{r}_j|} \end{aligned} \quad (2.28)$$

where \vec{r}_i is the position of the i -th electron, \vec{R}_I is the position of the I -th nucleus, m_e is the mass of an electron, M_I is the mass of the I -th nucleus, Z_I is the atomic number of the nucleus (the number of positive charge carried by the nucleus). In this expression, the first term represents the kinetic energy of the electrons; the second term the kinetic energy of the nuclei; the third term the Coulomb interaction between different nuclei; the fourth term the electrostatic attraction between nuclei

and electrons; and the last term the interaction between electrons. Despite all the advances in modern quantum mechanics, however, by no means this equation can be solved exactly for a system more than two particles. But it is possible and feasible to find an approximated solution based on appropriate approximations.

2.2.1 Basic approximations

The first step in simplifying the problem is to separate the electronic and nuclear degrees of freedom. In observing that the masses of the nuclei are much larger (10^3 - 10^5 times an electron's mass) than those of the electrons, and the fact that the forces on the interacting particles are the same, the electron cloud can be assumed to respond instantaneously to the motion of the nuclei or the changes in the nuclear configuration. Therefore, the motions of electrons and nuclei can be treated independently and the many-body wave function of the system can be decoupled into a product of two parts

$$\Psi^{MB}(\vec{r}, \vec{R}) = \Psi(\vec{r}, \vec{R})\Phi(\vec{R}) \quad (2.29)$$

where $\Psi(\vec{r}, \vec{R})$ is the electronic wave function at a certain nuclear configuration \vec{R} , and $\Phi(\vec{R})$ is the nuclear wave function. This is the Born-Oppenheimer approximation [111, 112]. Based on this approximation, the main task of the electronic structure calculations is now reduced to solving the electronic Schrödinger equation under a

fixed atomic configuration

$$H\Psi(\vec{r}, \vec{R}) = E\Psi(\vec{r}, \vec{R}) \quad (2.30)$$

with a shortened form for the electronic Hamiltonian H

$$H = \sum_i^{N_e} \frac{-\hbar^2}{2m_e} \nabla_{\vec{r}_i}^2 - \sum_{i,I}^{N_e, N_N} \frac{e^2 Z_I}{|\vec{r}_i - \vec{R}_I|} + \frac{1}{2} \sum_{i \neq j}^{N_e} \frac{e^2}{|\vec{r}_i - \vec{r}_j|} \quad (2.31)$$

For a zero-temperature treatment, the kinetic energy of nuclei is omitted, and the total energy of the system can be written as

$$E^{MB} = E + \frac{1}{2} \sum_{I \neq J}^{N_N} \frac{e^2 Z_I Z_J}{|\vec{R}_I - \vec{R}_J|} \quad (2.32)$$

As we can see from the above discussion, the electron wave function is both a solution of the Schrödinger equation and a determinant factor of the electron Hamiltonian of the system. So it must be solved self-consistently at an external electrostatic potential generated by the frozen nuclei.

The relaxation of the nuclei, however, is driven by atomic forces on the nuclei. According to the Hellmann-Feynman Theorem [112], the k -component of the force on the I -th nucleus is given by

$$\vec{F}_{I,k} = -\nabla_{I, \vec{R}_k} E^{MB} \quad (2.33)$$

The ground state of a system locates at the global minimum of the potential energy surface (the dimension of it is the number of degrees of freedom in nucleus positions). The forces at this point, in principle, should reach zero. Such configuration is usually obtained by calculating the atomic forces and relaxing their coordinates using classical equations of motion. Generally speaking, it is important to achieve an equilibrium structure before evaluating the electronic structure and physical/chemical properties of the system.

Now it comes to the core of electronic structure calculation: the solution of the electronic Schrödinger equation. Since the electrons are only weakly-coupled in the systems of interest (organic molecules), it is justified to use another assumption that the electrons interact only via the effects of an average potential. This is also called the mean-field theory [111]. It leads to the single-particle description of the state of the system. Basically, there are two approaches, the Hartree-Fock theory and the density functional theory (DFT).

2.2.2 Hartree-Fock theory

The assumption of independently moving electrons and the requirement of satisfying Pauli exclusion principle implies that the total wave-function of the many-electron system can be approximated as an antisymmetric product of the orthonormal single-

electron wave functions $\psi_i(\vec{x}_i)$ [111]

$$\Psi^{HF}(\vec{x}_1, \vec{x}_2 \dots \vec{x}_N) = \frac{1}{\sqrt{N!}} \begin{vmatrix} \psi_1(\vec{x}_1) & \psi_2(\vec{x}_1) & \dots & \psi_N(\vec{x}_1) \\ \psi_1(\vec{x}_2) & \psi_2(\vec{x}_2) & \dots & \psi_N(\vec{x}_2) \\ \dots & \dots & \dots & \dots \\ \psi_1(\vec{x}_N) & \psi_2(\vec{x}_N) & \dots & \psi_N(\vec{x}_N) \end{vmatrix} \quad (2.34)$$

Here the spin orbital $\psi_i(\vec{x}_i)$ describes both the spatial distribution and the spin of an electron. We use \vec{x}_i to represent both space (\vec{r}_i) and spin coordinates. This method of using the single Slater determinant as a solution for the wavefunction is known as the Hartree-Fock (HF) method. According to the variational principle, the spin orbitals are determined by minimizing the electronic energy of the system

$$E_0 = \langle \Psi_0 | H | \Psi_0 \rangle \quad (2.35)$$

Based on this, the HF equation can be derived to an one-electron eigenvalue equation

$$F_1 \psi_i(\vec{x}_1) = \varepsilon_i \psi_i(\vec{x}_1) \quad (2.36)$$

The orbital energy of the spin orbital ψ_i is ε_i . The Fock operator is defined as

$$F_1 = \frac{-\hbar^2}{2m_e} \nabla_{\vec{x}_1}^2 - \sum_I \frac{e^2 Z_I}{|\vec{r}_1 - \vec{R}_I|} + \sum_{j \neq i}^{N_e} \int d\vec{x}_2 \psi_j^*(\vec{x}_2) \frac{e^2}{|\vec{r}_1 - \vec{r}_2|} (1 - P_{12}) \psi_j(\vec{x}_2) \quad (2.37)$$

The first term is the kinetic energy of a chosen electron; the second term is the potential energy for attraction to the nuclei of this electron; the third term is the so-called HF potential which describes the interaction of the chosen electron with the rest of electrons in a way of average potential experienced by it. This potential includes two parts, the coulomb potential and the exchange potential, which is written in terms of an operator P_{12} operating to the right and interchanging electron 1 and electron 2.

Besides the fact that Hartree-Fock theory does not take into the account the correlation between electrons except the parallel-spin electron correlation via Pauli exclusion principle, this wavefunction-based method can be computationally very expensive for large scale electronic structure calculations, in particular for molecular electronics problems. The size of a Hartree-Fock calculation increases with N^5 , where N is the system size (the number of basis functions) [113]. The largest computational cost is related to the calculation of the Fock matrix, the matrix representation of the many-body Hamiltonian of a system. Nevertheless, it is still of great merit to introduce the HF theory. The HF approximation, which is equivalent to the molecular orbital approximation, is central to our understanding of chemical bonding, atomic and molecular spectra, physical/chemical interactions, interfacial features between dissimilar materials, etc.

An extension of the HF method is to include the excited determinants as N -electron basis functions. This is known as Configuration Interaction (CI). With this method,

one could obtain the correlation energy which is missing in the single-determinant HF approach. But it is even much more expensive than the HF method, and almost unaffordable for a relatively large system.

2.2.3 Density functional theory (DFT)

In 1964, Hohenberg and Kohn [114] demonstrated a theorem in which the problem of finding the many-body wavefunction is reduced to that of calculating the equilibrium charge density $\rho(\vec{r})$. This is called the density functional theory (DFT) [115].

2.2.3.1 Hohenberg-Kohn theorem

The Hohenberg-Kohn Theorem states that every observable in a quantum system can be calculated from the electron density of the system alone. Firstly, the ground state energy of a N -electron system is a unique functional of the charge density $\rho(\vec{x})$.

$$E = E[\rho] = T[\rho] + V_{ext}[\rho] + V_{Ne}[\rho] + V_{ee}[\rho] \quad (2.38)$$

Here, the four terms are the electron kinetic energy, the potential due to the external applied electric field, the electron-nucleus interaction and the electron-electron interaction. That is to say, the electronic density unequivocally determines the potential energy, thereby also determines the ground state wave function. Secondly, the ground

state density minimizes the energy functional. In other words, for any trial density $\rho'(\vec{x})$, with the variational principle, it satisfies that

$$E_0 \leq E[\rho'(\vec{x})] \quad (2.39)$$

This provides a way of solving the equilibrium problem.

DFT is a significant contribution in computational physics and chemistry. It shifts our focus from the quantum wave function to the classical electron charge density. In this case, the number of parameters involved is greatly reduced. Instead of dealing with the coordinates of each particle, three spacial parameters are used to describe the electron density in real space. Now if only one could know the density functional, one would solve the variational problem for the electron density and obtain all the ground state properties, including the wave function. Yet, by no means, could we get the exact density functional form. An approximate, yet practical approach was suggested by Kohn and Sham in 1965 [116].

2.2.3.2 Kohn-Sham theorem

The Kohn-Sham Theorem states that the density of the interacting system can be approximated by the density of an auxiliary system of noninteracting particles which do not interact with each other, and just move in an effective external field, V_{eff} . The problem of finding the ground state electron density is reduced to solving a set

of single particle Schrödinger-like equations:

$$\left[\frac{-\hbar^2}{2m_e}\nabla^2 + V_{eff}(\vec{x})\right]\psi_i(\vec{x}) = \varepsilon_i\psi_i(\vec{x}) \quad (2.40)$$

where the effective potential V_{eff} can usually be written as a summation of the external potential originating from the nuclei as well as an external applied electric field if any, the Hartree potential and the exchange-correlation potential

$$V_{eff}[\rho(\vec{x})] = V_{ext}[\rho(\vec{x})] + V_{Hartree}[\rho(\vec{x})] + V_{XC}[\rho(\vec{x})] \quad (2.41)$$

The exact form of the exchange-correlation potential V_{XC} (formally defined as $V_{XC} = \frac{\delta E_{XC}}{\delta \rho}$) is, however, unknown. There have been a lot of efforts in generating approximate, yet suitable functional forms for $V_{XC}[\rho]$ since the very birth of DFT up to now. We will discuss this in more detail in the next section.

These equations are called the Kohn-Sham (KS) equations, which are similar to the HF equations, yet they include both exchange and correlation effects in principle. The set of eigenstates ψ_i are known as Kohn-Sham states. The total energy of the system can be obtained by the summation over all the KS eigenvalues ε_i of the occupied states. The effective potential V_{eff} , also known as the KS potential, has a functional dependence on the electron density ρ , which is defined in terms of the KS wave

functions by

$$\rho(\vec{x}) = \sum_i^{occupied} |\psi_i(\vec{x})|^2 \quad (2.42)$$

These equations are solved through iterating until self-consistency is achieved. One starts with an initial guess of the electron density ρ_0 . For instance, one can construct ρ_0 from a sum of superposition of atomic charge densities. Then one evaluates the effective potential V_{eff} with this density and solve the KS equation. This, in turn, generates a new set of KS wave functions, thereby a new electron density ρ_1 . As a convergence criterion, if $|E_1 - E_0| < \epsilon_E$ or $\int d^3x |\rho_1 - \rho_0| < \epsilon_\rho$ (ϵ_E and ϵ_ρ are small values preset for energy and density matrix convergence, respectively), the self-consistency is achieved and the SCF cycle stops. Otherwise, the cycle continues until the convergence criterion is met.

It is worth pointing out that strictly speaking, the KS orbitals are not molecular orbitals of the many-electron system. In principle, DFT is good for description only the ground-state properties. A systematic comparison of DFT methods for molecular orbital eigenvalue calculations was done by Zhang *et al.*[117]. It is shown that after an empirical linear correction, all 11 functionals considered in their study predict accurate HOMO orbital energies and accurate HOMO-LUMO gaps. Nevertheless, besides the fact that the DFT approach has been employed widely to the calculation of electronic band structures in solids and molecular energy levels in molecules or clusters in the scientific community with great success in many cases, we should

always be aware of the limitations when using DFT.

The electron transport properties of molecular systems are, to a large extent, determined by three factors: the band structure of the electrodes, the positions of the energy levels of the scattering region and the level alignment between the two [45]. Therefore, the accuracy of a transport calculation using DFT Hamiltonians depends on the accuracy of band structure and/or molecular energy level calculations.

2.2.3.3 Exchange-correlation functional forms

The exchange-correlation term in energy E_{XC} describes all the difference between the energy of the exact ground state and the energy of a "classic" form: kinetic + Coulomb interaction. Within the variety of functional forms proposed today, they can be categorized into three groups: the local density approximation (LDA), the generalized gradient approximation (GGA) and the hybrid exchange functional form.

LDA was the first proposed and simplest of all. In LDA, E_{XC} is given in terms of local electron density only

$$E_{XC}^{LDA} = \int \rho(\vec{x}) e_{XC}[\rho] d^3x \quad (2.43)$$

where e_{XC} is the exchange-correlation energy density for a uniform electron gas. Such examples include Von Barth-Hedin (VBH) [118], Perdew-Zunger (PZ or CA) [119],

etc.

An improvement based on this is GGA, which introduces terms depending upon the gradient of the electron density

$$E_{XC}^{GGA} = \int \chi_{XC}[\rho, \nabla \rho] d^3x \quad (2.44)$$

Examples of GGA include Perdew-Wang (PW91) [120], Perdew-Burke-Ernzerhof (PBE) [121], etc. The gradient-corrected form usually gives more accurate results than LDA, although not always [122].

The intrinsic drawback of both these two categories is that they are local approximations, while the exact exchange-correlation potential may be non-local. A third class of functional forms takes a compromise step by choosing the exchange functional as a linear combination of Hartree-Fock, local and gradient-corrected exchange term, like in B3LYP, i.e. Becke 3-Parameter exchange [123] and Lee, Yang and Parr correlation [124] functional form. The orbital interpretation seems more rigorous in this case, because of the HF exact exchange. In many cases, it has shown to overtake LDA and GGA in reproducing the right band-gap of semiconductors [125]. But it is not always a practical choice for many DFT codes. It is more than a single rule to choose a right exchange-correlation functional form. And it is always a good practice to try with different functional forms before choosing one for a certain system.

2.2.4 Molecular orbital theory and basis sets

2.2.4.1 Molecular orbital theory

Another indispensable ingredient in solving the Fock or the Kohn-Sham equations is the accurate representation of the electron wavefunctions ψ_i , which we use to describe many-electron systems. The most prevailing approach in quantum chemistry is called the Molecular Orbital Theory, also known as the Linear Combination of Atomic Orbitals (LCAO) approach. From physics point of view, it is an extension of the Bohr's theory of electron configurations of atoms to an electron configuration description of molecules, which is central to our understanding of chemical bonding and physical/chemical interactions. It has proved to be very successful over the years, especially for non-strongly-coupled systems.

In this theory, the molecular orbitals are described by

$$\psi_i = \sum_{\mu} a_{\mu i} \phi_{\mu} \quad (2.45)$$

where ϕ_{μ} are atomic orbitals, and $a_{\mu i}$ are the corresponding atomic orbital expansion coefficients. Furthermore, the atomic orbitals can be expanded as a linear combination of a set of basis functions χ_j

$$\phi_{\mu} = \sum_j d_{j\mu} \chi_j \quad (2.46)$$

where $d_{j\mu}$ are the basis function expansion coefficients. The set of basis functions

is usually called a basis set. The idea of expanding a function linearly in a set of properly defined functions, however, is rather common. There are a variety of basis functions available in today's electronic structure calculation codes. By and large, they can be classified into two categories: localized and delocalized basis sets. And their form can either be analytical or numerical. In this thesis work, we have employed three typical basis sets: Gaussian type, numerical and plane wave basis sets for different applications. In some cases, the core electrons are described by effective core potentials or pseudopotentials. The characteristics of basis sets and the features of pseudopotentials will be discussed in the following sections.

For the completeness of this discussion, it is noteworthy to point out that the LCAO approach can also be adapted to the description of a periodic system, such as crystalline orbitals. In this case, a crystalline orbital, $\psi_i(\vec{r}, \vec{k})$, can be expressed as a linear combination of Bloch functions, ϕ_μ^{BF} , which, in turn, is defined in terms of local atomic orbitals, ϕ_μ :

$$\psi_i(\vec{r}, \vec{k}) = \sum_{\mu} a_{\mu i}(\vec{k}) \phi_\mu^{BF}(\vec{r}, \vec{k}) \quad (2.47)$$

$$\phi_\mu^{BF}(\vec{r}, \vec{k}) = \sum_{\vec{L}} \phi_\mu(\vec{r} - \vec{A}_\mu - \vec{L}) e^{i\vec{k} \cdot \vec{L}} \quad (2.48)$$

where \vec{A}_μ denotes the position vector of the μ th nucleus in the zero reference cell, and the summation is extended to all the lattice vectors \vec{L} .

2.2.4.2 Basis sets

Strictly speaking, a mathematical complete expansion of an exact wavefunction requires an infinite size of basis set. However, in real calculations, the basis set has to converge to a certain accuracy at a point so that it can be truncated to include only a finite number of basis functions. A computational study is always a juggling between the accuracy and the computational cost. There are two main considerations in the choice of a basis set [111]. The first is to use the fewest possible terms for an accurate representation of the molecular orbital. The second is to consider the speed of two-electron integral evaluation.

Over the years, a large variety of basis sets have been developed. In the following sections, we will introduce three typical basis sets: Gaussian type, numerical and plane wave basis sets, as were used explicitly in the thesis topics. A concise rather than comprehensive overview is provided here.

A. Gaussian type basis sets

Gaussian type orbitals, first introduced by Boys [126], are used extensively in the quantum chemistry and computational physics communities nowadays. Gaussian functions (GF) can be written in either polar or Cartesian coordinates:

$$\chi^{GF}(r, \theta, \phi) = NY_{l,m}(\theta, \phi)r^{2n-2-l}e^{-\alpha r^2} \quad (2.49)$$

$$\chi^{GF}(x, y, z) = Nx^{l_x}y^{l_y}z^{l_z}e^{-\alpha r^2} \quad (2.50)$$

where the exponent α defines the radial extent of the function, N is the normalization factor, and the sum of l_x , l_y and l_z gives the angular momentum l . GFs have the advantage of having an analytical form to evaluate the two-electron integrals (reducing four-center integrals to two-center integrals). In this respect, it is better than the Slater type orbitals. Nevertheless, a single Gaussian function does not describe the physics of orbitals correctly for both the tails of the orbital and in the vicinity of the nucleus. Therefore, a common approach is to use a fixed linear combination (contraction) of Gaussian functions (primitives), namely the contracted Gaussian function (CGF) as the basis function. It has the form

$$\chi^{CGF} = \sum_{i=1}^{N_P} c_i \chi_i^{GF}(\alpha_i) \quad (2.51)$$

where α_i and c_i are the contraction exponents and coefficients of primitives, and the summation runs over N_P primitive Gaussian functions. A common way of determining contractions is from the results of atomic SCF calculations [111].

There is a hierarchy of Gaussian type basis sets depending upon the size, thereby the accuracy. For example, STO-3G is a minimal basis set, with only one basis function for an occupied atomic orbital. Since most interactions come from the valence electrons, the split valence basis sets provide more flexibility in treating chemical bonding,

such as 6-31G. Here, each valence orbital is represented by two basis functions with the first one contracted (3 primitives) and the second one uncontracted. A further improvement is to include higher angular momenta than those of the valence orbitals to accommodate the deformation of orbitals in the presence of external perturbation, like other atoms, electric field and so on. These are called polarization functions. For instance, one uses the notation of 6-31G* or 6-31(d) for adding *d*-type functions to the first row atoms Li-F and the notation of 6-31G** or 6-31(d, p) for adding more *p*-type functions to H. In case of molecules with lone pairs and anions, highly diffuse (small α_i) basis functions can be added, such as 6-31+G* with *s*-, *p*-type functions added to non-hydrogen atoms.

The Gaussian program [127] comes with the Gaussian type basis sets. We have explicitly used this program in the studies presented in Chapter 4 and 5.

B. Plane wave basis sets

In contrast to Gaussian type basis sets, plane wave falls into the category of delocalized basis sets. Based on the concept of supercell, the plane wave basis set is defined as a function of the reciprocal lattice vector \vec{G}

$$\chi(\vec{r}) = e^{i\vec{G}\cdot\vec{r}} \quad (2.52)$$

where \vec{G} satisfies $\vec{G} \cdot \vec{L} = 2n\pi$ (\vec{L} is the supercell lattice vector and n is an integer).

As we can see, the plane wave basis set complies naturally with the Bloch's theorem, which states that in a periodic system, each electronic wavefunction can be written as a product of the periodic function and a plane-wave envelope function [112]. Thereby, the various potential energy terms in the Kohn-Sham equations can be evaluated in terms of their Fourier transforms and the Kohn-Sham secular equations can be solved very efficiently using Fast Fourier Transform (FFT) technique. This makes the plane wave basis sets a good option for periodic or relatively large molecular systems.

The size of the basis set is usually determined by the so called cut-off energy E_{max} to include a discrete set of plane waves with their kinetic energy $\frac{\hbar^2}{2m} |\vec{k} + \vec{G}|^2 \leq E_{max}$. The choice of the value of E_{max} is again a compromise between the accuracy and the computational cost.

It needs to point out that a plane wave basis set is usually very poor in expanding the electronic wavefunctions because a very large number of plane waves (a high E_{max}) are required to accurately describe the rapidly oscillating wavefunctions of electrons in the core region. Fortunately, most physical/chemical properties depend upon the valence electrons to a much greater degree than upon the tightly bound core electrons of constituent atoms. The use of plane wave basis sets is accompanied by introducing the pseudopotential approximation to remove the core electrons and the strong nuclear potential and replace them with a weaker pseudopotential which acts on a set of pseudo wavefunctions rather than the true valence wavefunctions. This makes it possible to use a relatively small number of plane waves to describe an

electron wavefunction within reasonable accuracy. We will discuss pseudopotentials in the following section. The use of the concept of pseudopotentials, however, is not limited to plane wave basis sets.

The VASP (Vienna Ab initio Simulation Package) program [128] comes with the plane wave basis sets and pseudopotentials. We have explicitly used this program in the studies presented in Chapter 3.

C. Numerical basis sets

In this case, the basis functions are represented numerically on atomic centered grids, with cubic spline interpolations between mesh points. These atomic basis orbitals are strictly confined orbitals, i.e. orbitals that are zero beyond a certain radius r_s . Within this radius, they are expressed as products of a numerical radial function and a spherical harmonic. For atom I located at R_I , they have the form [129]

$$\chi_{Ilmn}(\vec{r}_I) = \eta_{Il n}(\vec{r}_I) Y_{lm}(\hat{r}_I) \quad (2.53)$$

where $\vec{r}_I = \vec{r} - \vec{R}_I$. Just like in Gaussian type orbitals, there will be several orbitals (labeled by index n) with the same angular (l, m) dependence, but different radial dependence, which is conventionally called a "multiple- ζ " basis. Each radial function may have a different cutoff radius and, up to that radius, its shape is completely free and are defined by a cubic spline interpolation from the values given on a fine

radial mesh. These basis functions are usually generated by numerically solving the atomic Kohn-Sham equations for different ionization states with the corresponding approximate exchange-correlation functional [130, 129]. Polarization orbitals may also be included to account for the deformation induced by bond formation.

Using numerical basis sets, the electron density is projected on a real-space grid, in order to calculate the Hartree and exchange-correlation potentials and matrix elements. The efficiency of such a program depends on the numerical techniques for solving the integrals over basis functions. The SIESTA (Spanish Initiative for Electronic Simulations with Thousands of Atoms) program [129] implements a self-consistent density functional method using norm-conserving pseudopotentials and numerical atomic orbitals basis sets. The use of pseudopotentials is not strictly necessary with atomic basis sets. They are employed here, however, to get rid of the core electrons and, more importantly, to allow for the expansion of a smooth (pseudo-) charge density on a uniform spatial grid. We have explicitly used this program in the studies presented in Chapter 6.

D. Pseudopotentials

It is well known that the computational cost of a calculation is normally scaled as a power function of the system size N . Pseudopotentials are used to model the energetically deep-lying and chemically mostly inert core electrons. Usually only valence electrons (sometimes semicore electrons as well) are included in the system

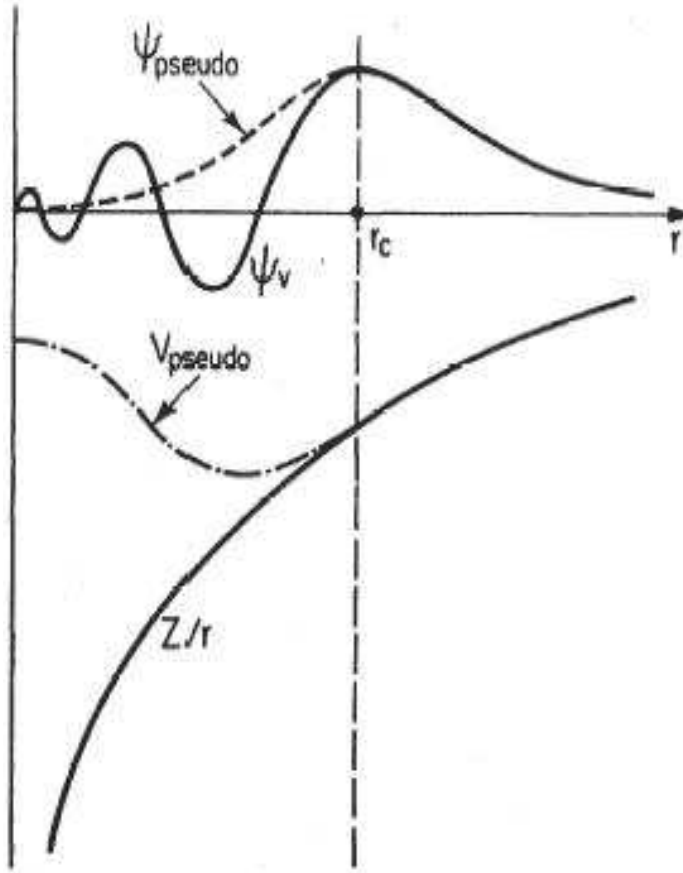


Figure 2.3: Schematic illustration of all-electron (solid lines) and pseudoelectron (dashed lines) potentials and their corresponding wavefunctions. The radius at which all-electron and pseudoelectron values match is defined as r_c [112].^{||}

and the electron-nucleus interaction is replaced by the interaction of valence electrons with the pseudopotential due to the core (nucleus + inner electrons). So the total number of electrons included for the calculation of the system is largely reduced. Such a calculation is expected to greatly enhance the simulation speed without losing its accuracy as compared to an all-electron calculation.

^{||}Reprinted with permission from M. C. Payne, M. P. Teter, D. C. Allan, T. A. Arias, and J. D. Joannopoulos, *Review of Modern Physics*, **64**, 1045-1097 (1992) ©1992 The American Physical Society. URL: <http://link.aps.org/doi/10.1103/RevModPhys.64.1045>

An pseudopotential is introduced to remove the core electrons and the strong nuclear potential and replace them with a weaker pseudopotential which acts on a set of pseudo wavefunctions rather than the true valence wavefunctions [112]. An ionic potential, valence wavefunction and the corresponding pseudopotential and pseudo wavefunction are illustrated schematically in Fig. 2.3. The true wavefunctions now are approximated by smoothly varying, node less pseudo wavefunctions. Outside a defined cutoff radius r_c , the pseudo wavefunction agrees with the all-electron wave function, and the two potentials are identical. The pseudopotential is constructed in such a way that its scattering properties or phase shifts for the pseudo wavefunctions are identical to the scattering properties of the nucleus and the core electrons for the valence wavefunctions. *Ab-initio* pseudopotentials and pseudo wavefunctions are usually generated by fitting into the valence properties of atomic calculations using the corresponding exchange and correlation functional.

Pseudopotentials, however, are not unique and a lot of different flavors have been developed over the years [131]. There are two forms of pseudopotentials most commonly used in the community, norm-conserving pseudopotentials [132, 133, 134] and ultrasoft pseudopotentials [135]. The outstanding feature of norm-conserving pseudopotentials is that the total charge enclosed within r_c should be the same for pseudo and all electron wavefunctions, which ensures the pseudo wavefunction is equal to the all-electron wavefunction outside of r_c (not only identical in their spatial dependences but also the same in their absolute magnitudes), so that the real charge density out-

side of r_c is reproduced. This is highly desirable if the exchange-correlation energy is required to be accurate. Besides, the norm-conservation helps the transferability. Nonetheless, there is always a balance between the transferability and the softness (the softer the potential, the less the computer cost). In this regard, an alternative choice is the ultrasoft pseudopotential developed by Vanderbilt in the early 1990s [135] by releasing the norm-conserving constraint. Instead, one corrects for the resulting difference between the real and the pseudo charge density using localized augmentation functions centered on each atom. A much smaller basis set is required to generate the smoother pseudo wavefunction. In case of plane waves, only about one-third of plane waves are needed for calculations of the same accuracy as compared to the norm-conserving pseudopotentials.

Ultrasoft pseudopotentials are used in all our VASP calculations (Chapter 3). And norm-conserving pseudopotentials are used in our SIESTA calculations (Chapter 6), where the use of ultrasoft pseudopotentials together with the numerical atomic orbitals does not lead to as much gain as in other cases [129].

Chapter 3

Organic Spin Valve - Role of Molecular Spacer

3.1 Introduction

The giant magnetoresistance (GMR) effect was first discovered in (001)Fe/(001)Cr multilayer structures in the late 1980's [42], where large resistance changes, up to 50%, were observed when an external magnetic field was applied. The authors ascribed the GMR to spin-dependent transmission of the conduction electrons between the magnetic Fe layers (which were antiferromagnetically coupled in the absence of a magnetic field) through non-magnetic Cr layers. This discovery opened the era of the study of the GMR effect in a variety of materials and their possible applications

in devices. Later the effect was found in systems other than multilayers, such as granular films, sandwiches and tunnel structures (TMR). The prototypical structure consisting of two magnetic layers bridged by a non-magnetic spacer F1/S/F2 is called a spin valve [136]. The resistance of such a device can be changed by manipulating the relative orientation of the magnetizations in the ferromagnetic layers F1 and F2, and this is the so-called spin-valve effect. The spin orientation of conduction electrons survives for a relatively long period of time (\sim ns), which makes spintronic devices attractive for many potential applications ranging from memory storage and magnetic sensors to quantum computing devices.

In the last few decades, the spacer materials in most spin-valve studies are metals. Intense research efforts are now devoted to extending these spin-dependent effects to semiconductor materials, because of the qualities of semiconductors, such as their ability to be "doped" with substances that make them carry more or less electricity, or make them able to emit light, and so on. While there have been noteworthy advances in spin injection and detection using inorganic semiconductors, little progress has been made on spin-valve devices with semiconducting spacers. A major problem in integrating the magnetic materials of spintronics with conventional semiconductors such as silicon or gallium arsenide is that conventional semiconductors must be fabricated at high temperatures, making it difficult to produce the ultra-thin layers necessary to make a spin valve. In contrast to conventional semiconductors, π -conjugated organic semiconductors may offer a promising alternative approach to semiconductor spin-

tronics, by virtue of their relatively large spin coherence, as reported by Xiong et al. recently in Nature [43]. In their study, a significantly large value of GMR 40% was found in the spin-valve structure using an organic semiconductor (8-hydroxyquinoline aluminum or Alq3) as the spacer.

As semiconductor devices are approaching their physical limits, the use of individual (organic) molecules to perform functions in electronic circuitry provides a promising alternative to conventional semiconductors. Now one would ask the question: Do we observe a similar spin valve effect (parallel spin configuration giving higher current) in an F1/S/F2 spin-valve structure using organic molecules as the spacer (S)? What are the optimum options for choosing such a molecular spacer?

Recently, using a tight-binding model, Zwolak and Di Ventra [52] predicted that spin-dependent transport can be observed in short DNA molecules sandwiched between ferromagnetic contacts. Emberly *et al.* [47] proposed that this spin-valve effect might be readily observable in Ni-BDT (benzene-1-4-dithiolate molecule)-Ni junctions using a tight-binding model. Pati *et al.* [48] first applied first-principles density functional (DFT) method and Landauer formalism to study the effect of spin alignment on the transport properties in a molecular wire Au-Ni-BDT-Ni-Au and came to the same conclusion that the spin-valve effect can be observed in this system. The resistance of such a system is predicted to be an order of magnitude larger in the anti-parallel spin configuration than in the parallel spin alignment. Rocha *et al.* [49] published a comparison study on the GMR effect having triphenyl-dithiolate or octane-dithiolate

sandwiched between two Ni(001) electrodes using the state-of-the-art NEGF method. But all the reported first-principles calculations on molecular spintronics so far deal with strongly coupled metal-molecule-metal junctions. Despite the theoretical prediction of spin-valve effect through organic molecules, there is a dearth of experimental evidence, mainly because of the challenge in producing reproducible connections between molecule and electrodes with well-characterized interfaces. Only very recently, spin-valve effect in magnetic tunnel junctions using a self-assembled-monolayer of octanethiol as the spacer was reported experimentally by Ralph’s group [44].

Due to the ease of fabrication, one of the frequently used experimental techniques in molecular electronics is to tether the molecule to a metal substrate via self-assembly of a molecular monolayer (SAM) and measure the transport properties of such a system using surface probe microscopy, like atomic force microscopy (AFM) and scanning tunneling microscopy (STM), whose ability to manipulate single atoms and molecules on the substrate has added a new dimension to the study of molecular electronics. In fact, STM has been widely used in recent years to study electronic properties of single molecules and self-assembled molecular nanostructures [137, 138, 139]. In STM measurements involving a SAM, the sample is usually separated from the probing tip by a vacuum gap, and only weakly coupled to the tip working as one of the two electrodes in a circuit. The electrons tunnel through the vacuum under an applied bias leading to a finite tunneling current. Most tunneling experiments [27, 140, 137, 138, 139] and theory on molecular devices [141, 142, 143, 144, 145], however, have

been concerned with the charge state of the electron. Limited attention is given to a system involving a SAM on a magnetic substrate probed by a non-bonded magnetic tip.

In this chapter, we have two main objectives. One is to see the feasibility of using spin-polarized STM to detect the spin-valve effect. We use a SAM of a prototypical molecule benzene-1-4 dithiol (BDT), which has been studied extensively from the theoretical perspective, on a Ni (111) substrate and probe the spin-polarized tunneling current via the SAM using a non-bonded Ni tip. The specific questions we would like to address are: First of all, can we observe a similar spin valve effect (parallel spin configuration giving higher current) as observed in strongly coupled metal-molecule-metal system? A positive answer to this question would lead to the experimental application of STM in exploring the intriguing possibilities of using the large variety of organic molecules to control spin-polarized currents. Secondly, how does the non-bonded configuration at one end of the molecule affect the spin-polarized current? Finally, does the magnetoresistance increase or decrease by introducing the SAM on the Ni substrate?

The second objective is to investigate different organic molecules in fulfilling the role of a non-magnetic spacer in a spin-valve structure. BDT is a typical π -electron conjugated molecule. Since electronic transport characteristics of molecular systems are determined by their electronic and geometrical structures represented by electron charge distribution, chemical bonding, and molecular orbital energies, it is of interest

to examine the effect of a SAM of σ -bonded molecules on spin-dependent electron tunneling between two magnetic electrodes. Here in comparison, we report the results of such a study, where the SAM consists of, bicyclo[2.2.2]octane-1,4-dithiol (BCODT) molecule, a σ -bonded cage system that has been predicted to have a very small electron transfer coefficient [146] due to strained chemical bonds and highly confined electrons. The molecular length of the BDT and the BCODT SAMs are about the same (~ 12 Å), which allows us to compare the results of the two systems focusing on the electronic structure difference.

In order to address these questions, we have used density functional theory in conjunction with the Bardeen, Tersoff, and Hamann (BTH) formalism (Eqn. 2.7) of electron tunneling to calculate the spin polarized current in a metal-SAM-vacuum-metal architecture. In such an architecture, sophisticated first-principles based Keldysh non equilibrium Green's function formalism in which the tip, SAM, and the substrate is treated by considering a single cell, may not be suitable because of the inherent difficulty in treating the long range, non-bonded interaction in the density functional approach.

3.2 Simulation Model and Computational Details*

3.2.1 Current formalism for spin-polarized electron transport

Assuming elastic scattering and neglecting spin-flip scattering and spin precession in the tunneling process because of the weak spin-orbit and hyperfine interaction expected in the π -conjugated organic layer [43], the spin-polarized electron tunneling current between two magnetic electrodes can be written as $I = I^\uparrow + I^\downarrow$, where I^\uparrow and I^\downarrow are contributions from spin-up and spin-down states. In the low bias limit, $I^{\uparrow(\downarrow)}$ for the system considered in this study can be calculated in the framework of the Bardeen, Tersoff and Hamann formalism (discussed in Section 2.1.1) as follows:

$$I^{\uparrow(\downarrow)} = \frac{2\pi e}{\hbar} \gamma \int_{-\infty}^{\infty} \rho_s^{\uparrow(\downarrow)}(E + \frac{eV}{2}) \rho_t^{\uparrow(\downarrow)}(E - \frac{eV}{2}) e^{-2d\sqrt{\frac{2m}{\hbar^2}(\phi_{av}-E)}} \{ [f(E - \frac{eV}{2})[1 - f(E + \frac{eV}{2})] - [f(E + \frac{eV}{2})[1 - f(E - \frac{eV}{2})]] \} dE \quad (3.1)$$

where $\rho_s^{\uparrow(\downarrow)}$ and $\rho_t^{\uparrow(\downarrow)}$ are the spin-up (down) projected density of states (DOS) of the monolayer and the tip cap, respectively, d is the distance of the tip from the monolayer, E is the injection energy of the tunneling electron, ϕ_{av} is the average work function of the monolayer and the tip. Refer to Eqn. 2.7 in Section 2.1.1 for the rest of the symbolic meanings. As we are interested in the low bias regime (e.g. $E <$

*Part of Section 3.2 and 3.3 is reproduced with permission from H. He, R. Pandey, R. Pati, and S. P. Karna, *Physical Review B*, **73**, 195311 (2006) Copyright©2006 The American Physical Society

0.5 eV), the effective mass of the electron (m) and the average work function (ϕ_{av}) are assumed to be constant under applied bias. To match the respective electrochemical potentials at zero bias, the Fermi energy of the monolayer on Ni and the probe tip is aligned and taken to be the reference energy in Eqn. 3.1. It should be pointed out that we have not included the bias induced changes on the DOS of SAM, which is important in case of high applied bias. In such cases, one also needs to include spin-flip effect. In case of molecular systems, in the presence of low applied bias, no significant shift in molecular spectra were reported from previous theoretical studies [145, 48], suggesting that one does not expect a significant change in tunneling current in the low bias regime that we have considered here.

3.2.2 Computational details

We chose a supercell of size $2 \times \sqrt{3} \text{ \AA}$ in the xy plane parallel to the surface and a vacuum of 10 \AA in the z -direction for both the Ni(111) bare surface and the SAM on Ni(111) substrate for electronic structure calculations. A three-layer slab with four Ni atoms per layer is used to simulate the bare Ni substrate, while a BDT or BCODT molecule adsorbed perpendicularly at the three-fold fcc site [147] of Ni(111) is used to model the SAM (see for example, Fig. 3.1). Since the adsorption-related relaxation effect in the substrate is expected to be small as we move away from the top layer of the slab, the innermost layer of Ni is kept fixed at the bulk equilibrium

geometry. The structural relaxation is carried out with a maximum force criterion of $0.03 \text{ eV}/\text{\AA}$ on individual atoms. The Ni tip is assumed to be separated from the SAM by a rectangular vacuum barrier of width 5 \AA . To model a realistic description of the tip shape, its cap configuration is varied from a single Ni atom to a Ni cluster involving 5 and 13 atoms respectively to study the shape dependent electron tunneling feature of the tip. It is important to point out here that the Ni substrate and the monolayer together are considered as a single magnetic domain. We artificially broadened the density of states for various cap configurations using Gaussian broadening scheme of width 0.2 eV (a few $k_B T$ at room temperature) to take into account the broadening due to semi-infinite nature of the tip. Be advised that it has been reported from scanning tunneling spectroscopy (STS) experiment that the life time broadening of the electrons in a cluster on a surface (which may be used to mimic a STM tip) is of the order of $\geq 0.2 \text{ eV}$ [148].

The self-consistent spin-polarized electronic structure calculations were performed using the plane-wave pseudopotential[135] approach within general-gradient-approximated (GGA) DFT as implemented in the VASP program package [128]. The exchange and correlation effects are treated by the Perdew-Wang (PW91) exchange and correlation functional form[120]. Initially, a $(4 \times 4 \times 1)$ Monkhorst-Pack grid was used for k -point sampling of the Brillouin zone which was extended to $(10 \times 10 \times 1)$ grid for calculations of density of states. The cutoff for plane waves is 242 eV , and that for the augmented electron density is 449 eV in these calculations.

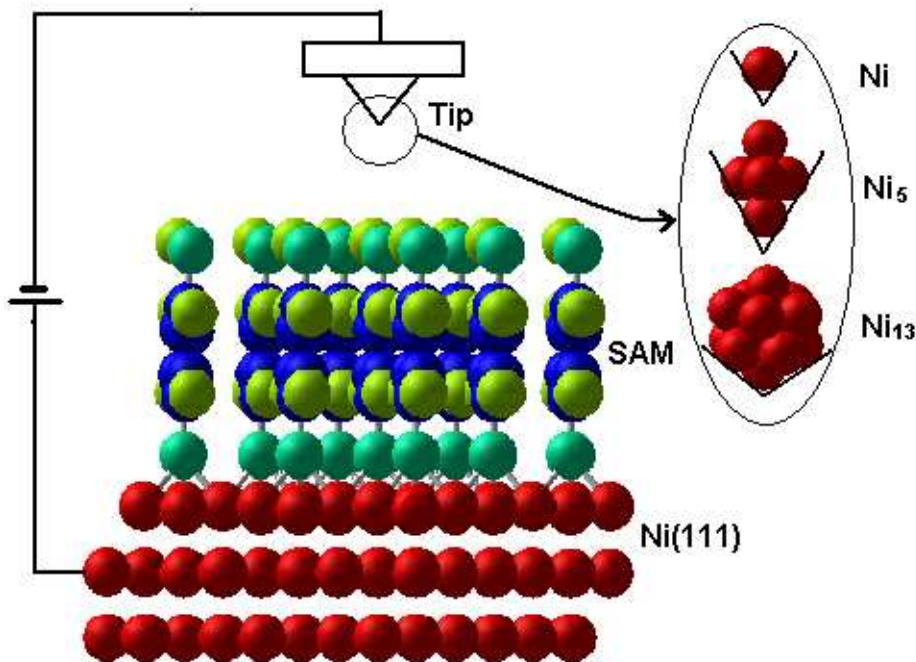


Figure 3.1: A schematic illustration of the self-assembled BDT monolayer on the Ni(111) substrate and the Ni probe tip separated by vacuum in a STM experiment. Notation of symbols: red - Ni; cyan - S; blue - C; green - H.

3.3 Spin-Valve Effect in a Ni-BDT...Ni System

3.3.1 Structural and magnetic properties

For the adsorbed BDT at the three-fold fcc site of Ni(111), the calculated Ni-S bond length is ~ 2.18 Å. It agrees well with the length of 2.20 ± 0.02 Å reported for the Ni-S bond in alkane thiolate adsorbed on the Ni (111) substrate [147]. For the Ni (111) substrate, a very small ($\sim 1\%$) contraction of the bond distance from its bulk value is obtained, while an outward expansion of about 0.4% in the direction of the adsorbed

molecule is predicted for the case of the SAM on Ni. For the bare Ni (111) surface, the magnetic moment per atom is $0.69 \mu_B$, which is in agreement with the previously reported value of $0.66 \mu_B$ obtained using the full potential linearized augmented plane wave (FLAPW) method [149]. In the case of SAM on Ni, the magnetic moment per Ni atom is reduced to $0.62 \mu_B$. It is clear that the magnetic moment of Ni is quenched after the adsorption of BDT.

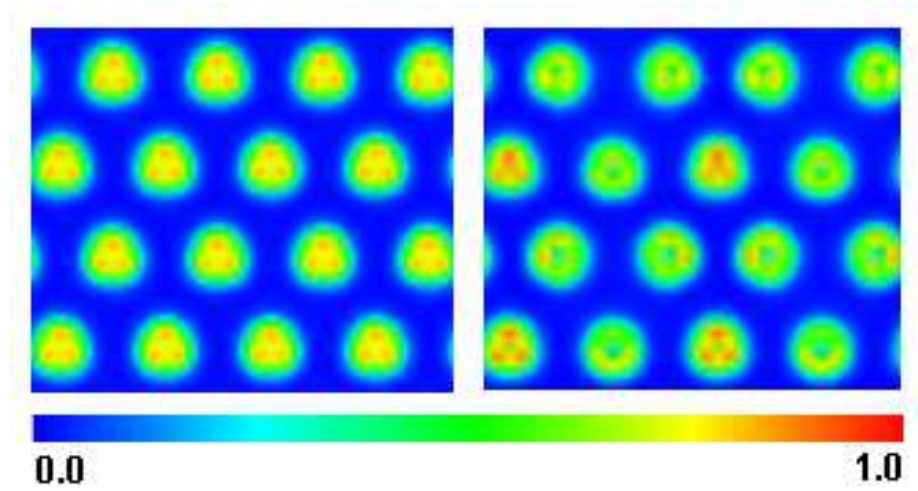


Figure 3.2: The magnetization density of the Ni surface layer (a) before (left), and (b) after (right) the deposition of the SAM.

The magnetization density (also called spin density) calculated on the Ni (111) surface before and after the adsorption of the BDT molecular SAM is shown in Fig. 3.2. The bare Ni (111) surface clearly shows a uniform magnetization. In contrast, the surface with the SAM has non-uniformity in the magnetization density. Furthermore, the three Ni atoms that are bonded to the S atom of the molecule have lower magnetization density compared to the non-bonded Ni atom. This is due to the electron

transfer from the monolayer to the d -down band of the bonded Ni atoms on the substrate arising from the hybridization between the Ni d -orbital and the p -orbital of S, suggesting a dominant bond-mediated electron tunneling mechanism at the interface.

3.3.2 Work function

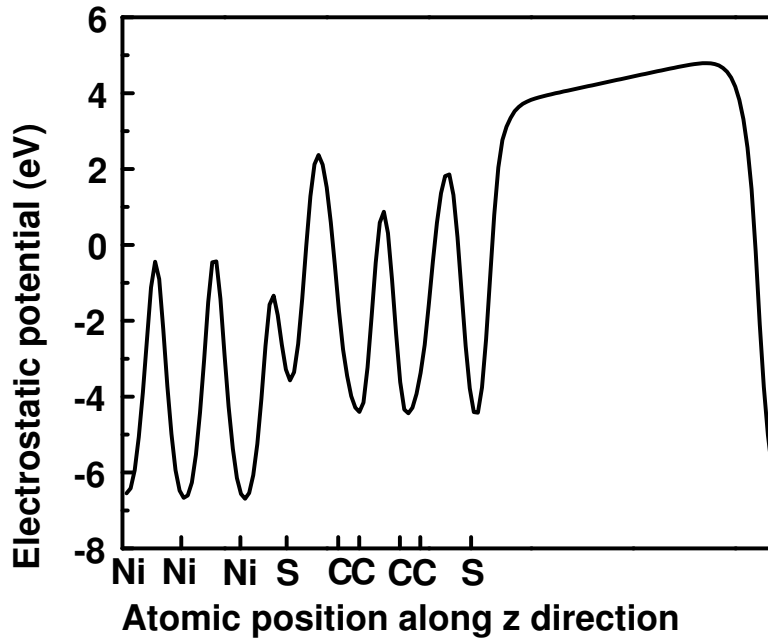


Figure 3.3: The planar average electrostatic potential along the z direction for one unit cell of the BDT monolayer coated on Ni(111).

The work function of the SAM, defined as the energy difference between the vacuum-level potential and the Fermi energy level of its surface, is calculated to be ~ 4.4 eV. The vacuum-level potential is calculated from the planar average of the electrostatic

potential in the unit cell (Fig. 3.3). Since the shape of the cap configuration of the tip is varied, one would expect the potential required to remove an electron from the tip having different cap to be different. In order to take this shape-dependent feature of the tip into account in this simple model, we have used their respective ionization potentials (i.e. 7.62, 6.22, and 5.88 eV for Ni, Ni₅ and Ni₁₃ respectively [150]) and have added the work function of the SAM surface to it to obtain the average work function (ϕ_{av}).

3.3.3 Tunneling current

Figure 3.4 shows the calculated current under a positive bias on the sample for the configuration in which the spin of the tip is aligned parallel (anti-parallel) to that of the substrate. The different current for the spin-up and spin-down states (shown in the inset of Fig. 3.4) can be attributed to the large imbalance between the spin-up and spin-down DOS of the SAM (Fig. 3.5) and the tip (Fig. 3.6) in the immediate vicinity of the Fermi energy. The exchange interaction between the parallel spins of the valence and core states of the Ni atom induces a strong spin polarization in the DOS of the tip and the Ni substrate. After molecular adsorption, the spin polarized *d*-states of the Ni substrate hybridizes with the *p*-states of the S atom of the BDT molecule, polarizing the spin in the monolayer. The spin polarization factor, $P = (DOS^\uparrow - DOS^\downarrow)/(DOS^\uparrow + DOS^\downarrow)$, in the monolayer is found to fluctuate from

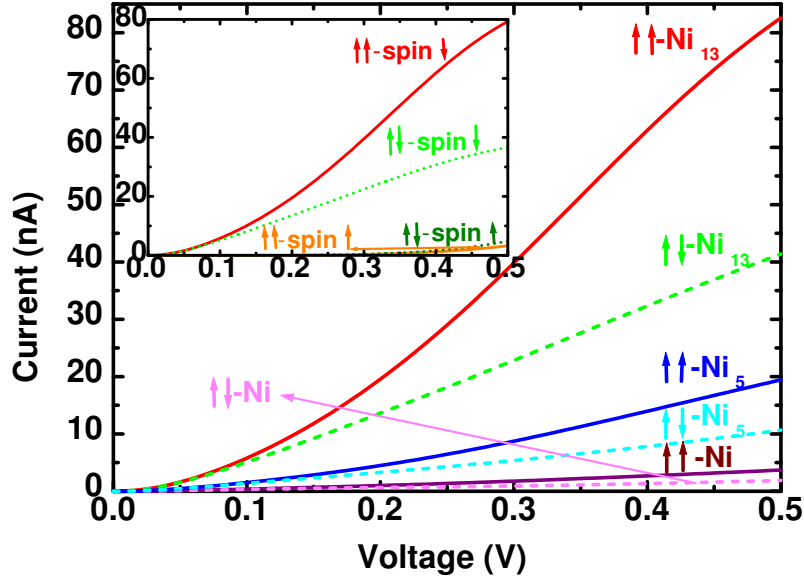


Figure 3.4: $I - V$ curves for the parallel ($\uparrow\uparrow$) and anti-parallel ($\uparrow\downarrow$) alignments of spins of the tip-molecular wire system. The contribution to the total currents from spin-up (\uparrow) and spin-down (\downarrow) states in both parallel and anti-parallel spin alignments is shown in the inset for using Ni_{13} as the tip cap.

4% to 45% corresponding to the variation in the injection energy from 0.0 eV to 0.3 eV. Because of the spin polarization both at the magnetic substrate and the organic monolayer, the spin-up and spin-down carriers experience different scattering potentials, and hence yield a different current. A higher I^\downarrow suggests that the spin down electrons are the majority carrier in the configuration considered in which the spin down π^* (π anti-bonding) molecular orbital of the monolayer appears to be the primary channel for the tunnel current.

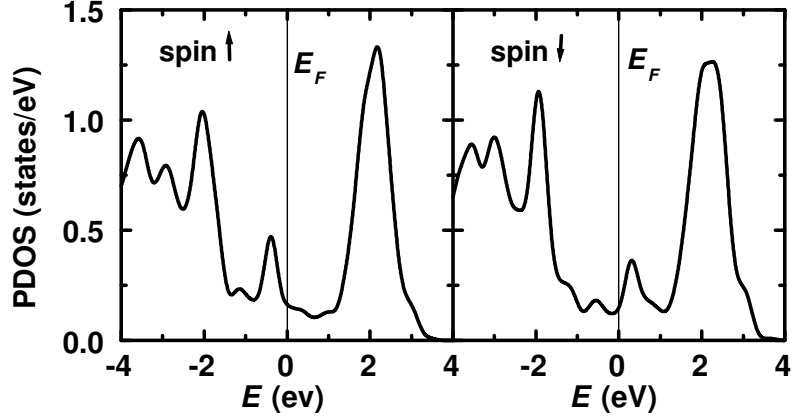


Figure 3.5: The projected density of states of the BDT monolayer on Ni(111). Zero of the energy is aligned to the Fermi energy.

It is important to point out that since the a priori information about the exact broadening of the energy spectra of the cap due to semi-infinite nature of the tip is not available, we considered a Gaussian broadening of 0.2 eV for the cap configuration. To study the effect of the broadening width on the tunneling and magnetoresistance, we calculated the spin-polarized tunneling current for the Ni₅ atomic cap configuration by considering a different smearing width of 0.3 eV. The results are summarized in Fig. 3.7. The increase in current for both parallel and anti-parallel spin configuration is evident in the case of stronger broadening as expected. But the increase in current due to larger broadening is found to be the same for both parallel and anti-parallel configuration suggesting the magnetoresistance value is not affected by broadening.

It is found that the tunneling current in parallel alignment of spins between the tip

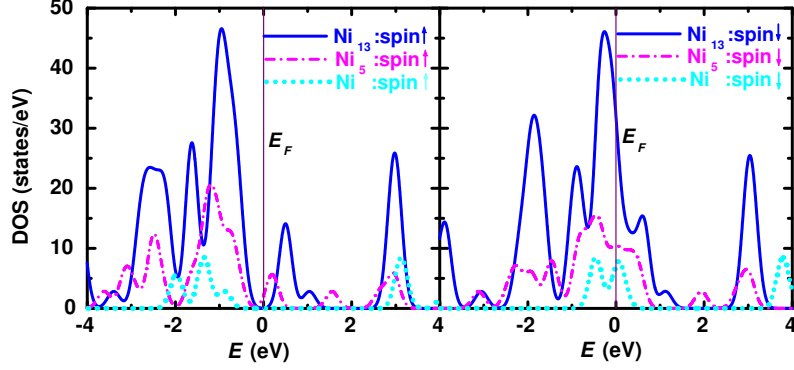


Figure 3.6: The projected density of states of the probe tip cap consisting of a Ni atom, a Ni₅ cluster and a Ni₁₃ cluster respectively. The energy levels are broadened using the Gaussian smearing of width 0.2 eV.

and the substrate is significantly higher than the current in the anti-parallel alignment. For example, the tunneling current in the parallel alignment is found to be about 99.5% higher in the case for a Ni₁₃ cap at 0.5 V. A similar effect has been observed earlier in magnetic-single molecule junctions [48, 49] and has recently been demonstrated experimentally in magnetic-organic monolayer junctions [44]. The electron tunneling probability from the tip to the SAM can be characterized by a response at the SAM due to a perturbation at the tip under applied bias, which depends primarily upon the convolution of the projected density of states of the tip cap and the SAM at the position of the tip. The larger current in the parallel configuration is due to stronger convolution of the occupied spin-up (down) DOS of the tip cap with the unoccupied spin-up (down) DOS of SAM at the position of the tip. Take the Ni₁₃ case for example (see Fig. 3.8). In the near- E_F region, both SAM/substrate and tip are

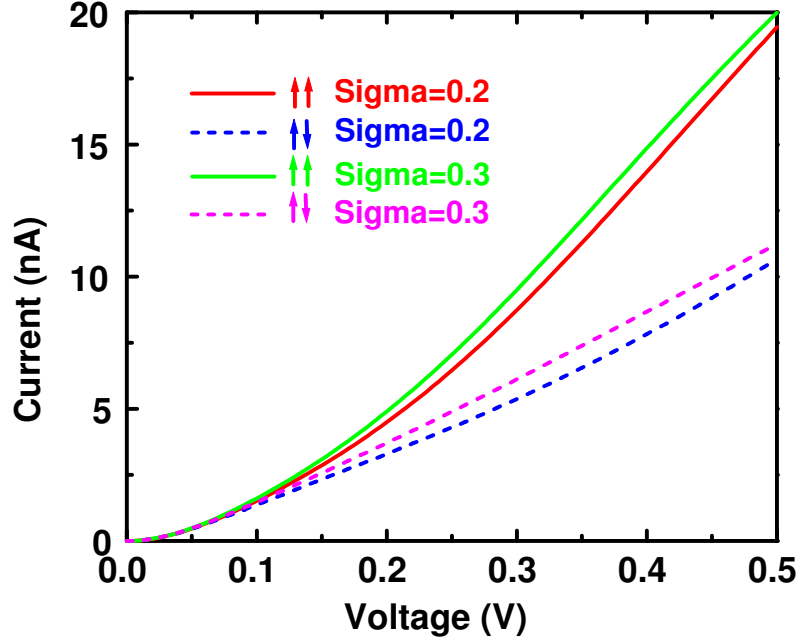


Figure 3.7: I-V curves for the parallel ($\uparrow\uparrow$) and anti-parallel ($\uparrow\downarrow$) alignments of spins of the tip-molecular wire system with Ni_5 as the cap configuration. Sigma represents the width of the Gaussian smearing used to take into account the semi-infinite nature of the tip.

characterized by a large DOS for electrons with minority spin and given a symbolic value of 1; while a small DOS for electrons with majority spin and given a symbolic value of 0. Therefore, when the net magnetic moments (or majority spins) of substrate and tip are aligned in parallel, the total current can be expressed as $1 \times 1 + 0 \times 0 = 1$; while aligned in anti-parallel, the total current gives $1 \times 0 + 0 \times 1 = 0$. This is just an analogue way of expressing Fig. 3.8.

By fitting the linear part of the $I - V$ curve, the resistances associated with parallel

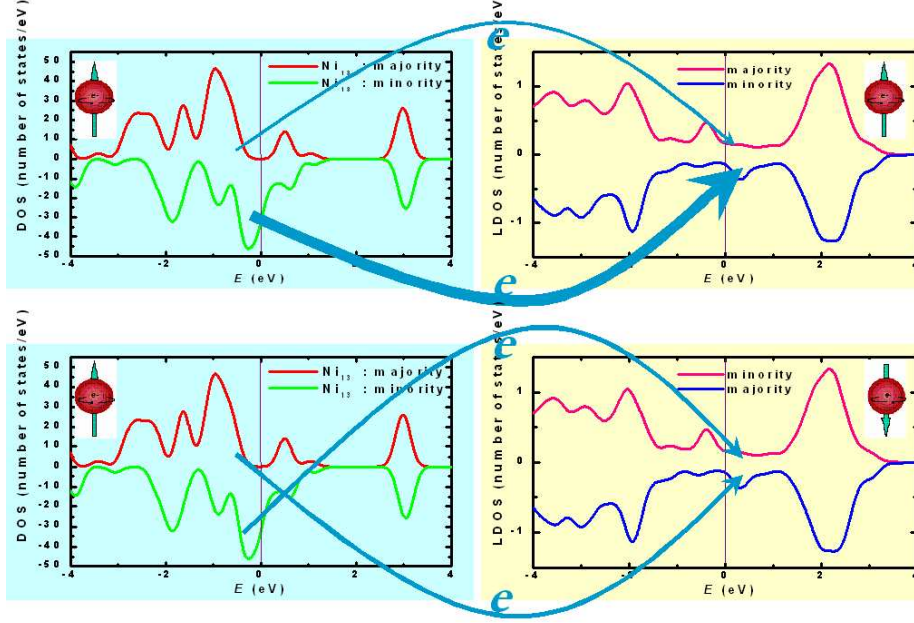


Figure 3.8: A diagram showing the origin of spin-valve effect in the tip-molecular wire system with Ni_{13} as the cap configuration under a positive bias on the sample. The arc arrow represents the electron current flow, expressing both the direction and magnitude.

(R_P) and anti-parallel (R_{AP}) spin alignments are obtained. The calculated values for R_P and R_{AP} are 4.5 M Ω and 10.7 M Ω , respectively for a Ni_{13} cap, leading to a change in magnetoresistance $\frac{R_{AP}-R_P}{R_{AP}}$ of about 57%. The calculated change in magnetoresistance for Ni and Ni_5 cap configurations are 54% and 51%, respectively.

As shown in Fig. 3.4, the absolute magnitude of tunneling current is found to depend sensitively on the shape of the tip cap. The increase in current for the Ni_{13} cap configuration is solely due to the increase in projected density of states of the Ni_{13} cap near the Fermi energy (Fig. 3.6) and the smaller average work function for Ni_{13} cap configuration. It is noteworthy to point out here that our emphasis is on the rel-

ative difference in the tunnel current calculated for the parallel and anti-parallel spin configurations, not on the absolute magnitude of the tunnel current as calculations assume the proportionality factor γ to be 1 in Eqn. 3.1. The change in magnetoresistance essentially remain the same for the three different cap configurations of the tip.

Note that the calculated tunnel current between the probe tip and the magnetic substrate without the organic monolayer (i.e. $\sim 13 \text{ \AA}$ vacuum barrier) is relatively very small, though the current in the parallel alignment is significantly higher than that in the anti-parallel alignment, suggesting higher magnetoresistance ($\sim 90\%$) in case of bare Ni-vacuum-Ni tip configuration. It is obviously due to the presence of a larger polarization in density of states associated with the Ni surface atoms in the absence of the monolayer. A passive barrier is therefore offered by the organic monolayer in the magnetic tip-SAM (substrate) configuration considered in the present study. It is important to point out that though Ni substrate-vacuum-Ni architecture provides higher magnetoresistance, it will not be of practical use as controlled spin polarized transport through the vacuum can not be feasible. On the other hand different molecules will endure different degree of spin polarization due to their interaction with the magnetic substrate, thus offering a viable medium for controlled spin-polarized transport, a main theme in molecular spintronics.

3.3.4 Summary

In summary, we have investigated the spin-polarized electron tunneling mediated by an organic molecule between two magnetic electrodes (one being the non bonded electrode) using periodic DFT in conjunction with BTH electron tunneling formalism. The calculations show that the absolute magnitude of the tunnel current depends sensitively upon shape of the tip cap, suggesting that a spatially broadened wave function at the tip is more effective in electron transport than a constrained wave function. However, the change in magnetoresistance is essentially found to be the same for the three different cap configurations of the tip. The calculated results also show that the spin-polarized electron tunneling strongly depends on the relative orientation of the spin at the substrate and the probe tip. A parallel alignment of the spin at the probe tip with respect to that at the substrate results in a higher magnitude of the tunnel current than the anti-parallel alignment - an effect prerequisite for an organic spin valve. It is expected that the present calculation will have a direct relevance to the widely used STM experiment in which a non bonded tip is usually used to measure the tunneling current. We suggest that by considering a magnetic tip and magnetic substrate, one would be able to observe such switching effect. Since the magnetic tip dimension is much smaller than the dimension of the substrate, the coercive field for it would be different from that of the substrate. Thus one can easily change the spin configuration at the tip with respect to the substrate using external magnetic field.

3.4 Spin-Valve Effect in a Ni-BCODT...Ni System[†]

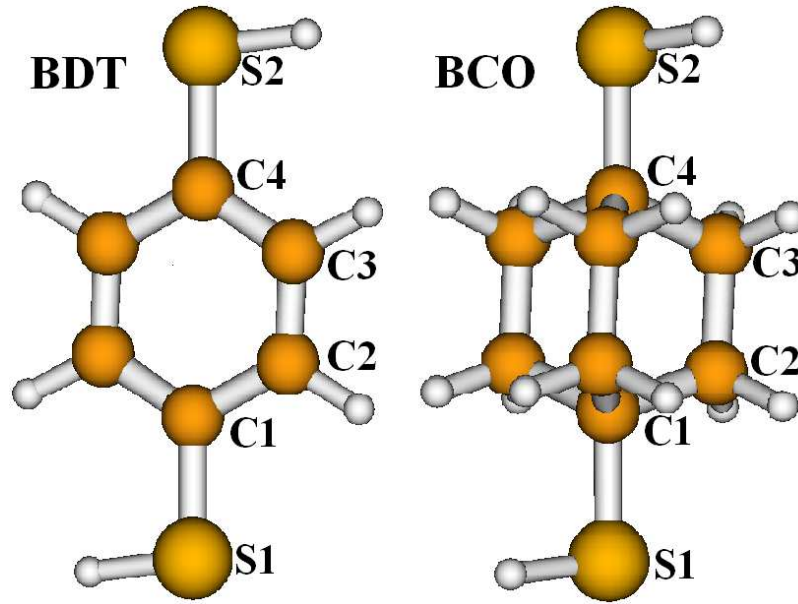


Figure 3.9: A sketch of the geometrical configurations of benzene-1,4 dithiol (BDT) and bicyclo[2.2.2]octane-1,4-dithiol (BCODT) molecules. Notations of S1, S2 and C1 - C4 are referred to the sulfur or carbon atoms in the molecules in an ascending order of the distance away from the Ni(111) substrate.

A non-magnetic spacer in a spintronics device is found to play a role more than just a simple barrier [151, 152]. It is suggested that the nature of the electronic states in both spacer element and magnetic electrodes can be important in determining the tunneling conductance of a given device. However, up to date, little is known about the nature of such states in the proposed molecular spintronics devices. It is well known that the electronic property of molecules generally determines their classifi-

[†]Reproduced with permission from H. He, R. Pandey, and S. P. Karna, *Chemical Physics Letters*, **428**, 411 (2006) Copyright©2006 Elsevier B.V.

cation as semiconductors or insulators. The first category consists of the conjugated molecules with delocalized π -electrons where the energy gap between the highest occupied molecular orbital (HOMO) and the lowest unoccupied molecular orbital (LUMO) is usually about 2-4 eV. The molecules in the second category are generally the σ -bonded alkanes in linear chain or cage structures with a relatively larger HOMO-LUMO gap (> 6 eV). In this section, we report the results of a comparison study using a SAM consisting of BCODT molecules with σ -bonded cage structure (see Fig. 3.9).

A similar STM setup was applied except use of a larger supercell 3×3 $\mathbf{R}60^\circ$, with 9 Ni atoms/layer due to the larger xy dimension of BCODT. A calculation on BDT mediated spin-polarized electron transport was repeated using the same sized supercell for comparison.

3.4.1 Structure and energetics

Table 3.1: Bond lengths (R) and binding energy (E_b) of bicyclo[2.2.2]octane-1,4-dithiol (BCODT) and benzene-1-4-dithiol (BDT) adsorbed on Ni(111).

Molecule	R_{C-C} (Å)		R_{C-S} (Å)	R_{Ni-S} (Å)	E_b (eV)
BCODT	1.54	1.57	1.84, 1.89	2.18	2.85
BDT	1.41	1.42	1.76, 1.79	2.19	2.24

The calculated bond lengths together with binding energy for the BCODT system

are listed in Table 3.1. Also listed in the table for comparison are the corresponding parameters for BDT adsorbed on Ni. The BCODT molecule consists of C-C single bonds with a bond length (R_{C-C}) in the range of 1.54~1.57 Å, whereas in the BDT molecule three π bonds are shared by the six C atoms in addition to the C-C σ bonds yield a shorter bond length (R_{C-C}) of about 1.42 Å. The C-S bond length in BCODT is slightly larger than that in BDT implying a relatively smaller overlap of atomic orbitals between C and S atoms in the former. The adsorption of molecules via S-Ni bond on the substrate further stretches the C-S bond by 0.06 and 0.02 Å for BCODT and BDT, respectively. The calculated Ni-S bond length (~ 2.18 Å) remains the same for the two systems.

The surface binding energy of the molecule is calculated by subtracting the energies of an isolated molecule and the Ni (111) bare surface from the total energy of the combined system. As shown in Table 3.1, the bulky molecule BCODT appears to form a relatively more stable monolayer on Ni (111) than BDT by an energy of 0.61 eV. It is clear that despite the same anchor atom S, the difference in the overall structure of the two molecules plays a significant role on their binding and interaction with the Ni substrate.

The work function of monolayers of BCODT and BDT is calculated to be 4.77 and 4.54 eV, respectively. It suggests an easier emission of electrons from the BDT SAM. A value of 4.40 eV calculated in the last section was a result of higher surface coverage employed in the calculation. To a first order, the work function used for a current

calculation (i.e. ϕ_{av}) is an average of those of the monolayer surface and the probe tip, as we have described in the last section.

3.4.2 Tunneling currents

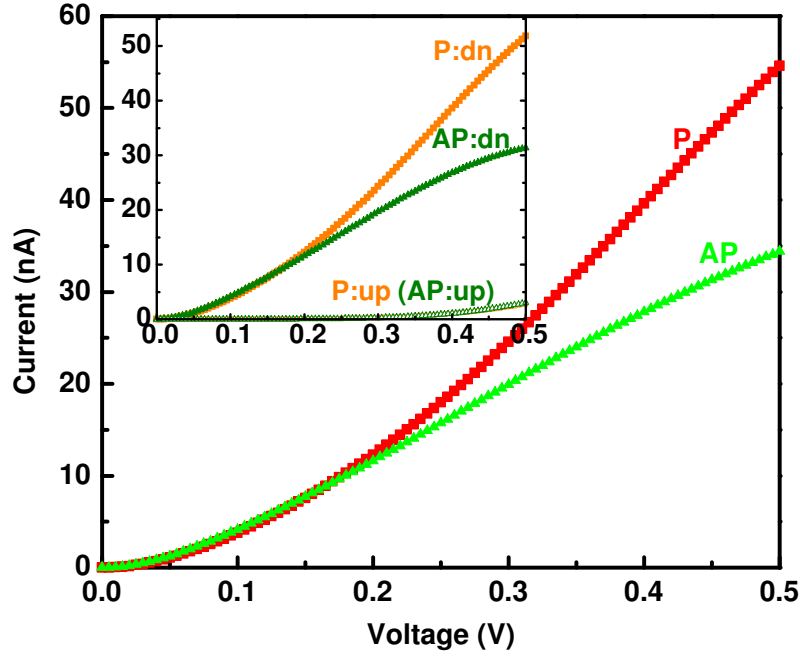


Figure 3.10: $I - V$ curves for the parallel (P) and anti-parallel (AP) spin configurations of the tip-vacuum-SAM-substrate system. The contribution to the total currents from spin-up and spin-down electrons in both parallel and anti-parallel spin configurations is shown in the inset.

The total tunneling current calculated for the configurations in which the spin orientation of the magnetic tip (using Ni_{13} as the cap) is aligned either parallel (P) or anti-parallel (AP) to that of the magnetic substrate is shown in Fig. 3.10. Individual

contributions of spin-up and spin-down electrons to the tunneling current are shown in the inset of Fig. 3.10. It is apparent that at low bias voltage (up to ~ 200 mV), there is practically no effect of the spin orientation at the magnetic tip and SAM-substrate system on the tunneling current. However, as the bias increases, the parallel (P) orientation appears to offer a greater tunneling probability than the anti-parallel (AP) orientation. An important point to note in molecular-mediated tunnel current, as presented here is that, the tunneling current increases with bias in both P and AP spin orientation at the magnetic tip and the SAM-substrate complex. This is due to the quantum mechanical nature of electron tunneling, as in the current study, which unlike the GMR observed in the solid state, does not vanish and therefore does not switch off the current completely in the AP orientation.

Similar to the Ni-BDT \cdots Ni system, the electron tunneling probability depends primarily upon the convolution (mixing) of DOS of the tip cap and the SAM at the position of the tip. Under a positive bias, the electron current flows from the occupied $3d$ orbitals of the Ni tip to the unoccupied orbitals of the SAM adsorbed on the Ni substrate. As shown by the projected density of states (PDOS) given in Fig. 3.11, the spin polarized d -states of the Ni substrate hybridizes with the p -states of the S atom of the BCO molecule, polarizing the spin in the monolayer. We note that a higher spin polarization of the orbitals appears only in the immediate vicinity of the Fermi energy ($|\Delta E| < 1$ eV). In both P and AP spin configurations, spin-down electrons are found to be the major carrier, leading to a much higher current than

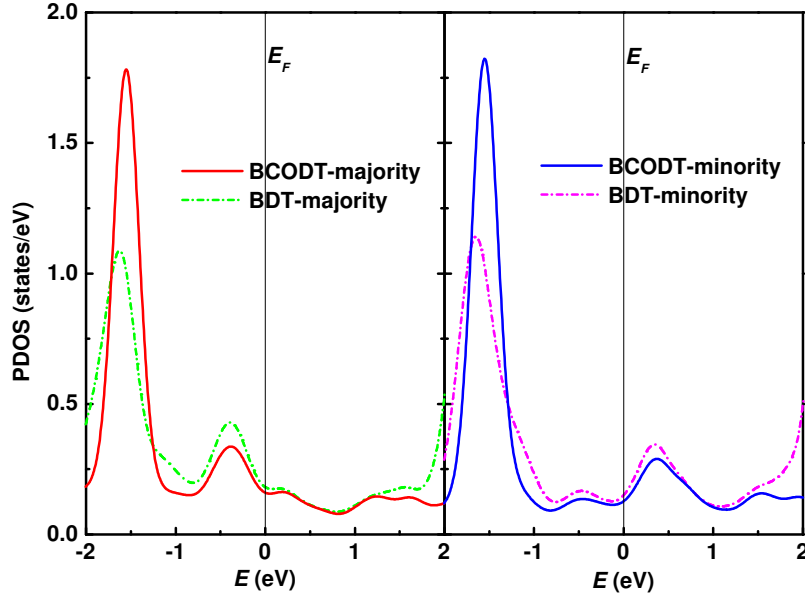


Figure 3.11: The projected density of states (PDOS) of the BCODT and BDT monolayers on Ni(111). Zero of the energy is aligned to the Fermi energy.

spin-up electrons (Fig. 3.10).

A comparison of the results of the transport calculations obtained for BCODT with those obtained for BDT shows, as expected, a higher tunneling current in the case of latter, due to a highly conjugated delocalized electrons. Another striking difference between the two molecular systems (BCODT and BDT) is seen in terms of the change in the magnitude of the tunneling current when the spin alignment of the tip and substrate switches from AP to P. It is attributed to the presence of a higher spin polarization in BDT above the Fermi level E_F (also see Fig. 3.11). For example, the tunneling current in the P alignment is about 60% higher for the case of BCODT,

whereas it is about 80% higher for BDT relative to that in the AP alignment at 0.5 V.

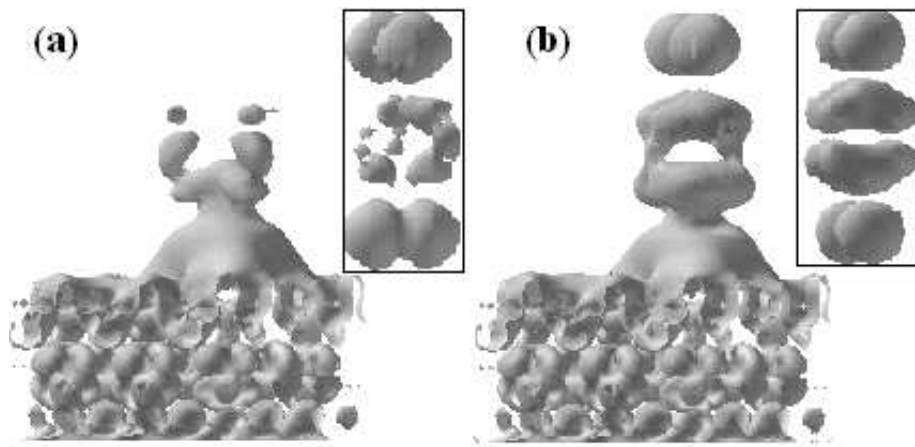


Figure 3.12: The spin density isosurface of (a) BCODT and (b) BDT monolayers deposited on Ni(111) substrate. The charge density of the HOMO of the corresponding molecule is also shown in the inserted box.

Figure 3.12 shows the spin density for molecular SAM on Ni substrate displaying a significant polarization associated with the S atom bonded to three Ni atoms. Comparison of the spin density on the backbone of C atoms, however, reveals a difference between BCODT (SAM)-Ni (substrate) and BDT (SAM)-Ni (Substrate). In the case of BDT, the spin polarization is distributed uniformly over the entire molecule, whereas in the case of BCODT it is non-uniform, decreasing rapidly away from the S-Ni bonding site in the molecule. This feature is again strongly correlated with the electronic structure of the molecules: the delocalized electrons in π -bonds in BDT have higher magnetization susceptibility than the localized electrons in σ bonds

in BCODT. The spin density distribution is a reminiscence of the HOMO of the molecule, which is also shown in the inset of Fig. 3.12 for both BCODT and BDT. The HOMO of BDT is a hybrid state of one of the π -orbitals of six C atoms and the lone pair p -orbitals of two S atoms and highly delocalized. In contrast, the HOMO of BCODT is mainly a combination of p -orbitals of two S atoms without any overlap.

3.4.3 Summary

We have investigated the effect of a σ -bonded, electronically "rigid" molecule in mediating spin-dependent tunneling between two magnetic electrodes in the weak coupling regime, in comparison with the case of a π -conjugated molecule. Our calculations reveal that at low bias potential there is little or no difference in the tunnel current across the tip-SAM junction for different spin configurations at the two electrodes. This is due to a very low electron-transfer coefficient of the BCO molecule due to highly confined electrons. At increased bias, both P and AP orientations of electron spin at the tip and SAM-substrate complex yield higher tunnel currents. However, the P orientation offers a higher current in comparison with the AP orientation. This is because the spin polarization of DOS induced in the SAM has the same sign as that in the tip as well as in the substrate, thereby a constructive convolution of DOS between the SAM and the tip is generated when the majority spins are aligned in parallel. The calculated spin-dependent electron transport mediated by σ -bonded

BCODT SAM on Ni, though qualitatively similar to the π -bonded BDT SAM on Ni, is quantitatively different. The total calculated tunnel current is much lower in the BCODT case than the BDT case. Further the difference in P and AP currents is also smaller by 20% in the BCODT system than that in the case of BDT due to a smaller and more localized spin polarization in DOS which mimics its intrinsic chemical bonding features. Comparison of studies for the two systems suggests that the magnitude of the tunnel current as well as the spin-dependent current is strongly influenced by the nature of the chemical bonds in the molecular structure.

Chapter 4

Giant Magnetoresistive Effect in a Carbon Fullerene - Interface Effect*

4.1 Introduction

The current field of molecular electronics/spintronics is driven by the potential of shrinking electronic/magnetic units down to the scale of a single or a few molecules. It is of interest to point out that in a strongly coupled metal-molecule-metal junction, the change in the atomic configuration and the formation of chemical bonding at the metal-molecule interface usually occur over several atomic distances, a scale that is in the same order of the dimension of the molecule itself. So the metal-molecule

*Partly reproduced with permission from H. He, R. Pandey, and S. P. Karna, *Chemical Physics Letters*, **439**, 110 (2007) Copyright©2007 Elsevier B.V.

interfacial features are at least as important as the molecular core in defining the $I - V$ characteristics of a molecular junction [79]. This chapter is devoted to study the detailed atomic structure at the molecule-electrode interface and understand its critical role in the electron tunneling in a molecular scale spintronic device.

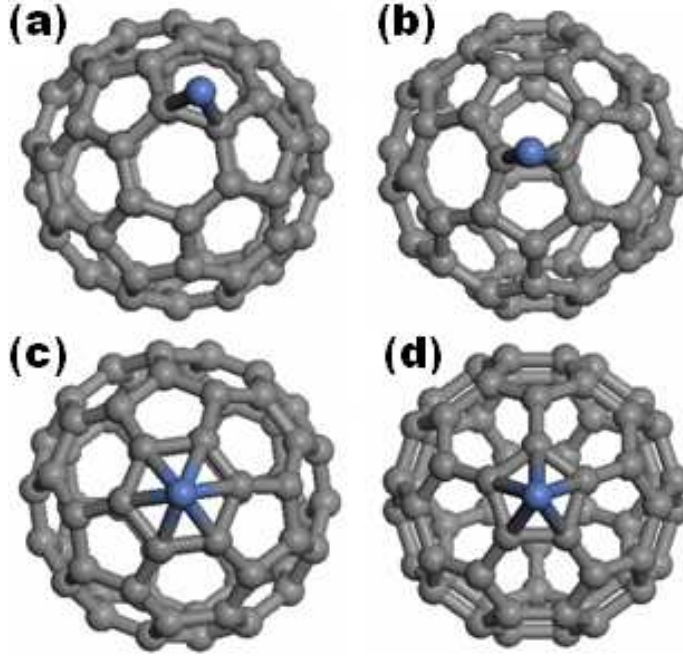


Figure 4.1: Binding sites of Ni on C₆₀: (a) B66 - a bridge site over a C=C double bond; (b) B56 - a bridge site over a C-C single bond ; (c) H6 - a hole site above the center of a hexagonal ring of C atoms; (d) H5 - a hole site above the center of a pentagonal ring of C atoms.

The particular molecule that we are interested in is C₆₀ fullerene molecule. In a recent experiment, Pasupathy *et al.* [153] reported the observation of C₆₀-mediated spin-dependent tunneling between ferromagnetic electrodes. Among other interesting features, the experiment demonstrated that C₆₀ molecules strongly couple with Ni electrodes, a key requirement for the Kondo effect. The observed zero-bias anomaly

in the conductance was in agreement with the results of theoretical predictions in similar systems[154]. At molecular scale, a goal of achieving a controlled assembly of such spintronic devices, however, requires a detailed and systematic understanding of the interfacial chemistry of the molecule and contact configurations and its role in the spin-polarized electron transport. This becomes even more important in the case of C₆₀ fullerene, which offers a number of chemically different binding sites on the cage surface. It has a high symmetry of icosahedra I_h consisting of twelve regular pentagons and twenty regular hexagons. All the C atoms are equivalent with sp^2 hybridization and each C atom is bonded to another three C atoms with two single bonds and one double bond. The C₆₀ molecule therefore has a variety of binding sites. As shown in Fig. 4.1, the B66 site is the bridge site over a C=C double bond between the 6-member and 6-member carbon rings, the B56 site is the bridge site over a C-C single bond between the 5-member and 6-member carbon rings, the H5 site is the hole site above the center of a pentagonal ring of C atoms, and the H6 site is the hole site above the center of a hexagonal ring of C atoms.

Besides, the C₆₀ fullerene is an electron-rich system with 240 valence electrons for 60 atoms, and a small HOMO (Highest Occupied Molecular Orbital) - LUMO (Lowest Unoccupied Molecular Orbital) gap around 2 eV. The fabrication of C₆₀ is well established and it is thermodynamically stable. All these merits put it in a good position of a realistic candidate in real-world applications.

In a photoelectron diffraction study of identification of the molecular orientation of the

adsorbed fullerenes with respect to the substrate, adsorption on the H6 site together with the B56 site as well as on edge atoms has been found for C_{60} on Cu(111) and Al(111), Cu(110) and Al(001), respectively [155]. In considering the wide versatility of the contact configuration for an electronic device, in a strong coupling regime involving Ni- C_{60} -Ni, various possibilities of bonding exists between the Ni atoms of the lead and a C_{60} cage. The nature of the metal-molecule interface is controlled by the geometry of the metal electrode and the binding site of the C_{60} molecule which makes connection of the molecular core to the electrodes. We consider here the case of break junctions made by stretching metal wires [156] where atomic-sized contacts are created by a metallic atom at each side as a contact. The nature of chemical bonding and its effect on spin-polarized electron transport via a variety of binding sites in Ni- C_{60} -Ni are studied using density functional theory in conjunction with the Landauer-Büttiker formalism.

4.2 Simulation Model and Computational Details

The electronic transport calculations on a C_{60} molecule coupled to semi-infinite Ni electrodes (Fig. 4.2) are performed using DFT with B3LYP exchange-correlation functional form [123, 124] using the Gaussian03 program package[127] in conjunction with the Landauer-Büttiker multi-channel formalism (as described in Section 2.1.2) encoded in a home-made program. The core scattering region was simulated by the

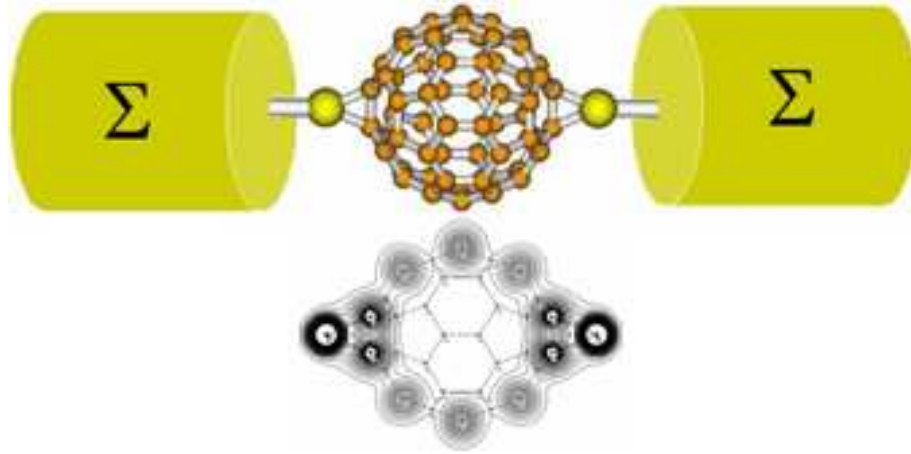


Figure 4.2: A schematic illustration of a Ni-C₆₀-Ni molecular device. Top: The left/ right contact region is modeled by a Ni atom and the rest of the semi-infinite electrode is a Ni bulk reservoir, described by an effective self-energy Σ . Bottom: A slice of the charge density plots of the core scattering region is shown for the B66 binding site of C₆₀.

extended molecular complex Ni_n-C₆₀-Ni_n where atomic scale contacts were used for the molecule. The LanL2DZ basis sets were used for both C and Ni atoms. Here again we neglect spin-flip scattering and spin precession in the tunneling process like we did in the last chapter (Section 3.2.1). And the spin-polarized electron tunnel current between two magnetic electrodes comes from contributions of both spin-up and spin-down electrons. The expression of each component of currents can be adapted from Eqn. 2.12 by simply removing the multiplying factor of 2. We notice that the most important factor in determining the tunneling current is the electron transmission function T , which can be calculated from a knowledge of the molecular energy levels and their coupling to the metallic contacts (see Section 2.1.3 for more details).

The Ni leads were modeled by a set of atoms, and its semi-infinite effect was implicitly

included by the self-energy term Σ . Several test calculations on $\text{Ni}_n\text{-C}_{60}\text{-Ni}_n$ ($n=1\text{-}3$ in shape of an atomic wire) yielded consistent results showing the convergence of the transport properties even with a single Ni atom representing the atomic contact reasonably well. We also modeled the contact electrode with Ni_4 in tetrahedron geometry. The calculated results are still reasonably close to the single Ni atom contact. This is because in Ni_4 , a single atom protrudes towards the C_{60} molecule and binds similar to the single Ni atom contact. Likewise, a small effect on the transmission function with the increase in the number of contact atoms was reported for the $\text{Al-C}_{60}\text{-Al}$ system [97]. On the other hand, due to the difficulty in achieving anti-parallel spin configuration between the two electrodes with increasing the number of Ni contact atoms, the following results are presented solely for the case of including one Ni atom at either electrode side in the central scattering region. The symmetry-constrained geometry optimization was performed for triplet spin state representing the parallel (P) spin alignment of the Ni atomic contacts in the system and kept the same for the singlet spin state representing the anti-parallel (AP) spin alignment (see Table 4.1). Transport calculations have been done on all the binding sites listed here. But in order to be concise, we will mainly focus on the discussion of two cases featured by two different typical interfacial chemical bondings - binding from B66 and H6 sites.

4.3 Site-dependency of GMR Effect in a Ni-C₆₀-Ni System

4.3.1 Ni-C₆₀-Ni bonding characteristics

Since the C₆₀ molecule offers a variety of binding sites on its surface, first-principles calculations were first performed on a single Ni atom bounded externally to C₆₀ to identify the site-preference of the Ni atom. The results predict that the bridge site over a C=C double bond (i.e. B66) to be the most stable site, which is followed by B56, H5 and H6 sites of the C₆₀ molecule. This is consistent with the behavior known of most transition metals binding towards C₆₀ [157], where the Ni atom acts as an η^2 ligand, forming two Ni-C bonds. Our calculated energetic results on Ni-C₆₀ also agree very well with an earlier study reported by Alemany *et al.* [158] using the quenching MD simulation approach.

The second Ni atom was then symmetrically added to the opposite side of the C₆₀ molecule and the Ni-C₆₀-Ni structure was optimized using symmetry constraint as listed in Table 4.1. The singlet (representing AP) and triplet (representing P) spin states were considered for the Ni-C₆₀-Ni system. The total energy of Ni-C₆₀-Ni follows the same order as that found for the Ni-C₆₀ molecular complex. The singlet spin state is always found to be lower in energy compared to the triplet spin state for all the binding configurations. We note here that the Ni atoms have non-zero magnetic

Table 4.1: Symmetry, bond lengths (R_{Ni-C}), relative total energy (E_t) with the total energy of the triplet state at the B66 binding site set to zero, magnetic moment of Ni (μ) and extra charges on Ni atoms (Q_{Ni}), on nearest neighbor C atoms (Q_{nn-C}), on second nearest neighbor C atoms (Q_{2nn-C}) of Ni-C₆₀-Ni extended molecular complex with different binding sites of Ni on the C₆₀ cage surface.

Binding site	B66	B56	H5	H6
Symmetry	D _{2h}	C _{2h}	D _{5d}	D _{3d}
R_{Ni-C} (Å)	1.94	1.96	2.19	2.25
R_{Ni-Ni} (Å)	10.76	10.78	10.25	9.93
E_t (eV)	0.0	0.27	1.00	1.82
μ (μ_B /atom)	0.69	0.58	0.87	0.55
Triplet Q_{Ni} (e)	0.38	0.32	0.58	0.45
Q_{nn-C} (e)	-0.28	-0.29	0.09	0.03
Q_{2nn-C} (e)	0.12	0.15	-0.17	-0.08
E_t (eV)	-1.16	-0.27	0.90	1.23
Singlet Q_{Ni} (e)	0.27	0.27	0.35	0.33
Q_{nn-C} (e)	-0.23	-0.25	0.09	0.04
Q_{2nn-C} (e)	0.10	0.14	-0.14	-0.08

moment (also listed in Table 4.1) aligned in parallel to each other in the triplet spin state. On the other hand, a strong hybridization of Ni-3*d* states with C-2*p* states leads to almost zero magnetic moment on Ni atoms in the singlet spin state of the system. The binding energy of Ni-C₆₀-Ni with respect to the constituent atoms is positive (6 eV) indicating the stability of the system. The bond length, R_{Ni-C} shows dependence on the binding site; it increases with the increase in the Ni coordination number from 2 associated with the B66 and B56 sites to 6 associated with the H6 site. At the B66 site, the bridge C=C bond is actually broken, and the bond length R_{C-C} increases from 1.40 to 1.49 Å which is in the magnitude order of the C-C single bond length. The Natural Bond Orbital (NBO) analysis suggests the formation of

Ni-C bond with a bond order of 0.7. At the H6 site, on the other hand, the $d - \pi$ orbital interaction only leads to slightly change in bond length in the hexagonal ring.

The Mulliken population analysis shows that C_{60} acts as an electron acceptor. In the ground state of an isolated C_{60} molecule, the electronic configuration has a threefold degenerate LUMO, t_u and a fivefold degenerate HOMO, h_u . The degeneracy in C_{60} -LUMO is lifted by the interaction between Ni and C atoms resulting in a partial occupation of C_{60} -LUMO orbitals in the Ni- C_{60} -Ni molecular system. Overall speaking, the charge transfer for the P and the AP spin orientations at the same binding site are very similar except a slight lower magnitude for the AP case. In addition to the fact that the charge transfer from Ni to C is slightly larger for the H6 site relative to the B66 site, it may also be worthy to point out that the charge distribution pattern is quite different for the two binding sites. In the case of the bridge site, the nearest (nn) C atoms have additional charge than what is transferred from a bonded Ni atom. The additional charge was provided by four second-neighbor (2nn) C atoms. Since the device is neutrally charged, the rest of the C atoms of the fullerene molecule were slightly negatively charged. For hole binding sites, six 2nn C atoms accept the charge transfer from the bonded Ni atom, while the six nn-C atoms remain slightly positively charged. The rest of the C atoms of the fullerene molecule remain almost neutral. The binding of Ni contact atom(s) at B66 and H6 sites therefore exhibits different interfacial features in Ni- C_{60} -Ni. At the bridge site, the charge transfer occurs mostly at the interface atoms where bonding between Ni and fullerene takes place,

whereas 2nn C atoms are mainly involved in the charge transfer process at the H6 site. This unique feature at the H6 site reflects a long-range interaction, which is a reminiscence of the long-range bound state in a Ni-benzene complex predicted by both electric deflection experiments and CASSCF + MRCI calculations [159].

4.3.2 Tunnel current and GMR

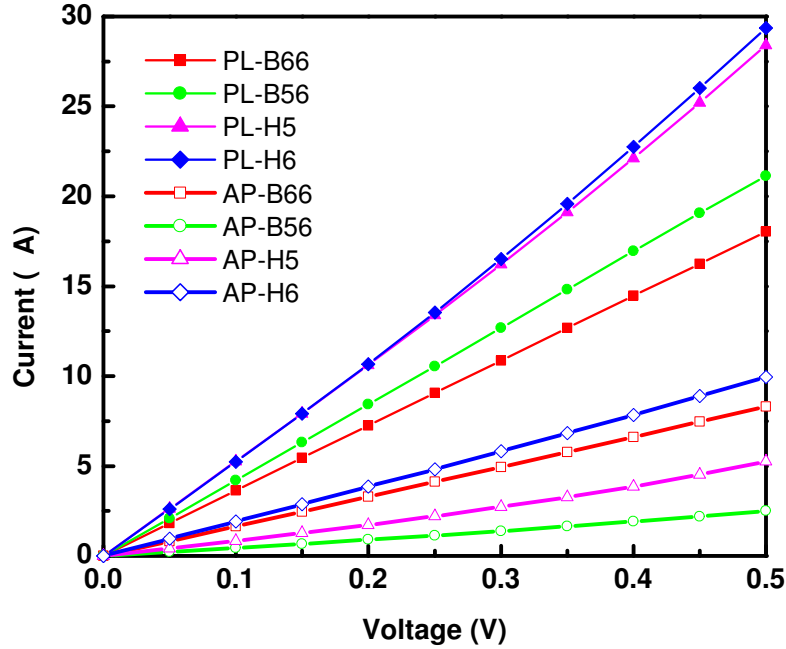


Figure 4.3: Current-voltage curves for parallel (PL) and anti-parallel (AP) spin orientations of Ni leads in Ni-C₆₀-Ni. The B66, B56, H5 and H6 are binding sites of C₆₀.

The calculated tunneling currents for all the four binding sites are shown in Fig.

4.3. The current is significantly higher in the P spin configuration than that in the AP spin configuration for both, the bridge and the hole, binding sites. It suggests a positive GMR effect in all the molecular systems considered here. Overall speaking, the tunnel currents associated with the hole sites (H6 and H5) are higher than those associated with the bridge sites (B66 and B56) in the device.

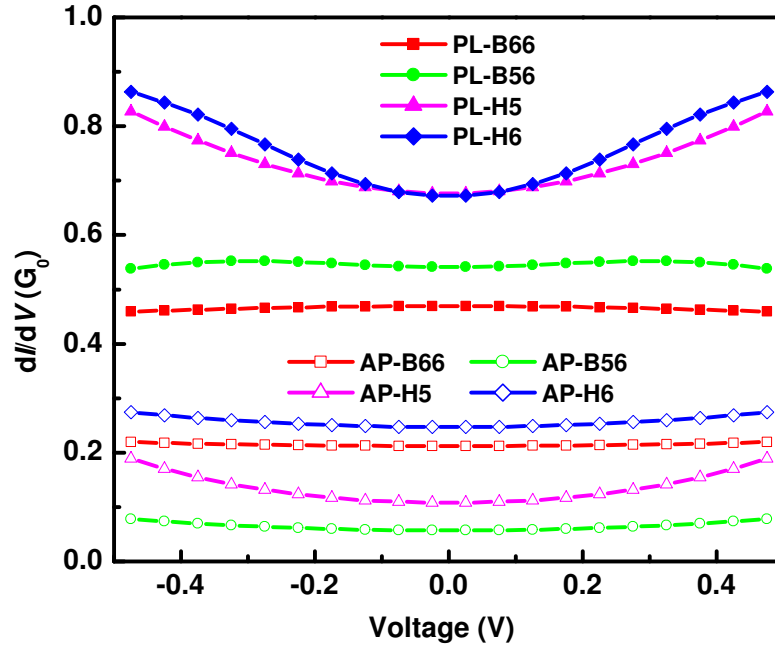


Figure 4.4: Differential conductance (dI/dV) vs. voltage curves for parallel (PL) and anti-parallel (AP) spin orientations of Ni leads in Ni-C₆₀-Ni. The B66, B56, H5 and H6 are binding sites of C₆₀.

In the low bias region (< 0.5 V), a linear response is observed for the P spin orientation, showing an Ohmic behavior. Such metal-like behavior has also been reported for Al-C₆₀-Al [160] and Au-C₆₀-Au junctions [161] in the low-bias regime. However, a

closer look at the differential conductance (dI/dV) suggests a slightly different trend in the variation of conductance with respect to external bias voltage (shown in Fig. 4.4). The conductance for the bridge interface is almost constant, showing a metal-like behavior, whereas the conductance for the hole interface has a relatively large fluctuation in going from zero to higher biases, indicating a tunneling behavior of the electron transport. This difference is a direct reflection of the sharper peak in transmission function in the vicinity region of E_F for H6 relative to B66 as we will discuss in the next section.

In the AP spin orientation, a linear response in $I - V$ curve in the low bias regime is well preserved. However, the differential conductance dI/dV decreases significantly compared to the P case, leading to a positive GMR as expected. In the P case, the equilibrium differential conductance values are 0.47, 0.54, 0.67, and 0.68 for B66, B56, H6 and H5, respectively; while in the AP case, the values are 0.21, 0.06, 0.25 and 0.11 for B66, B56, H6 and H5, respectively, in terms of $G_0 = 2e^2/h$. These values are in reasonably good agreement with those reported for Au-C₆₀-Au junctions ($\sim G_0$) [161], since Ni has a slightly larger work function (~ 5.5 eV) than Au (~ 5.3 eV). We note that the magnitude order of the predicted current in the AP case is similar to what was previously calculated for Au-C₆₀-Au [161], a non-magnetic system, and was measured for the electro-mechanic amplifier [162].

The calculated values for GMR (i.e. $\frac{G_P - G_{AP}}{G_{AP}}$) are plotted in Fig. 4.5. The magnitude of GMR in Ni-C₆₀-Ni is significantly large among the molecules so far being studied.

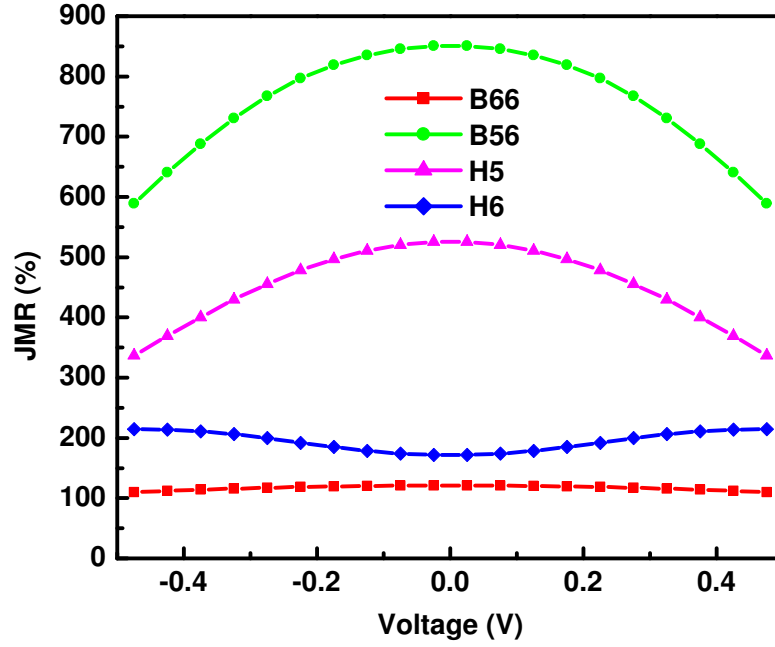


Figure 4.5: Junction magnetoresistance (JMR) vs. voltage plots for Ni- C_{60} -Ni. The B66, B56, H5 and H6 are binding sites of C_{60} .

The configuration with Ni binding at the B66 site of the fullerene molecule has the lowest GMR value of about 100%, and follows by the H6 site having a GMR value of $\sim 200\%$. Instead of remaining constant, the GMR values for the H5 and the B56 sites vary largely with the bias voltage, within the range of 300%-500% and 600%-800%, respectively.

4.3.3 Transmission function (T)

Now we step back and try to understand why we can observe GMR effect in such systems and why the GMR effect is different depending upon the specific binding geometry between the fullerene molecule and the electrodes. Specially we will discuss two cases- the B66 and the H6 binding sites in the following discussion since they represent the two dominant bonding features for electron transport.

The calculated transmission functions are shown in Fig. 4.6 for the P and AP spin orientations of the molecular system, respectively. The transmission function, in general, reflects the intrinsic transmission characteristics of the fullerene molecule despite the differences in the binding characteristics at the Ni-C₆₀ interface. The HOMO-LUMO gap of the isolated C₆₀ molecule reflects itself in a vanishing transmission gap in the near Fermi region [97].

Analysis of the scattering states near the Fermi energy reveals their character to be associated with HOMO or LUMO of the system. There appears a broad peak in the HOMO-LUMO gap region for the B66 site which becomes more pronounced for the H6 site in the case of the parallel orientation of the spin states of the atomic Ni contacts. Such a peak is usually identified as metal-induced gap states (MIGS) [163] whose origin is attributed to the interaction between the molecule and metallic electrodes. In order to explore the character of MIGS, we relate the calculated Kohn-Sham orbitals for the extended molecule to the calculated transmission function of

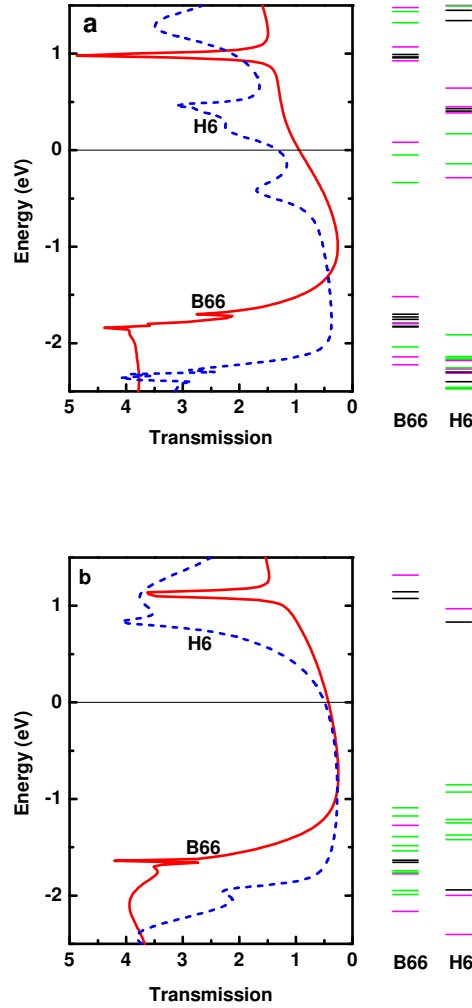


Figure 4.6: Transmission functions for (a) parallel (P) and (b) anti-parallel (AP) spin orientations of Ni leads in Ni-C₆₀-Ni. The Kohn-Sham orbitals are also given; pure C₆₀ orbitals are in black, hybrid states are in magenta, and pure Ni orbitals are in green. The B66 and H6 are binding sites, and zero of the energy is aligned to the Fermi energy.

the device in Fig. 4.6. Also shown in Fig. 4.6 are the molecular spectra of the device consisting of contributions from the pure fullerene molecule, the molecule-metal hybrid system, and the pure metallic contacts. Even though the carbon molecular

orbitals have sharp and high peaks in transmission and will be mostly responsible for the resonance tunneling, the hybrid orbitals play an important role in the low-bias regime.

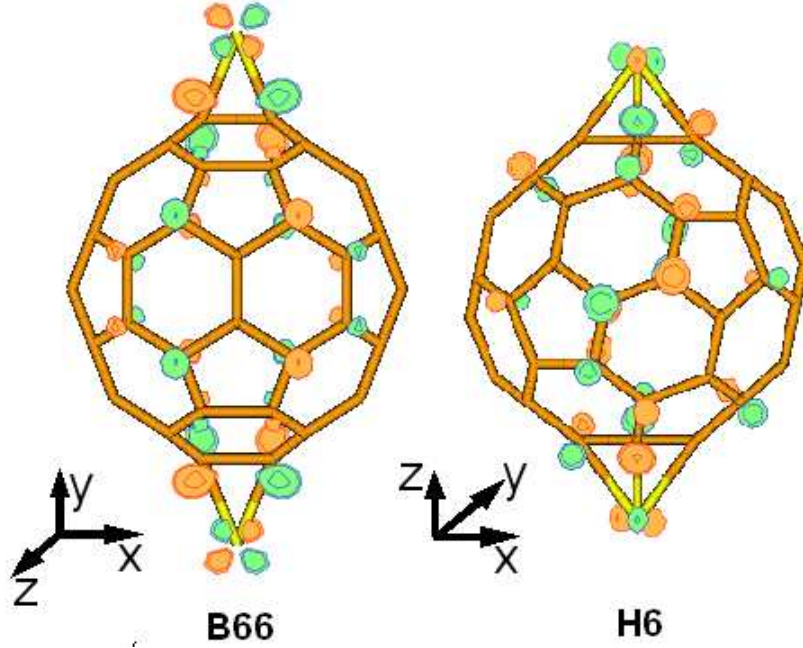


Figure 4.7: Molecular orbitals for α -HOMOs of Ni-C₆₀-Ni in which Ni is bonded at B66 (left) and H6 (right) sites in the parallel (P) case. One of C₆₀'s LUMOs takes part in the hybridization with Ni $3d_{xy}$ and $3d_{x^2-y^2}$ to generate the metal induced gap states (MIGS) in Ni-C₆₀-Ni. The orientation of Cartesian coordinates is also given here.

Analysis of molecular orbitals (Fig. 4.7) reveals that MIGS arise due to hybridization of one of the C₆₀'s LUMO orbitals with Ni's $3d$ orbital, $3d_{xy}$ and $3d_{x^2-y^2}$ for the B66 and H6 cases, respectively. In the case of H6, the hybrid LUMO is more extended leading to higher transmission for electrons tunneling through this eigen channel. A higher density of the hybrid states near the Fermi level, hence larger number of

tunneling channels, also appear to cause higher transmission for the H6 site relative to the B66 site in Ni-C₆₀-Ni.

4.4 Summary

The nature of chemical bonding at the molecule-electrode interface and its effect on spin-polarized electron transport in Ni-C₆₀-Ni are studied using DFT in conjunction with the Landauer-Büttiker formalism. The calculated results clearly show that the magnitude of the tunnel current strongly depends on the details of the molecule-electrode interface, especially the nature of the chemical bonding between the metal and C₆₀ molecule. For the Ni-C₆₀-Ni system, which allows bonding between Ni and C-atoms on C₆₀ surface at various sites, the tunnel current has a much higher magnitude when Ni is bonded to hole sites (H6, H5) than at bridge sites (B66, B56) of the fullerene cage. Furthermore, the magnitude of junction magnetoresistance is predicted to be significantly high for the molecular Ni-C₆₀-Ni system, and also shown to have a strong site-dependency. We have examined these phenomena from the electronic structure mechanism of spin-polarized electron transport in Ni-C₆₀-Ni, focusing on the role of chemical bonding in electron transport. Our calculations reveal that the prominent GMR effect in C₆₀-mediated electron tunneling between Ni electrodes is facilitated by metal-induced gap states (MIGS) between the highest occupied molecular orbital (HOMO) and lowest unoccupied molecular orbitals (LUMO), which in

turn depend strongly on the C_{60} binding sites for Ni.

Chapter 5

Unimolecular Diodes and Transistors - Functionalization of Molecules

5.1 Introduction

With the past four decades of continued miniaturization of the complementary metal-oxide-semiconductor (CMOS) transistors, the density of active devices in integrated circuits has essentially followed the so-called Moore's law [164], according to which the number of components per integrated function doubles every 18 months. According to the International Technology Roadmap for Semiconductors (ITRS) the CMOS

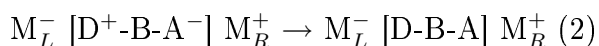
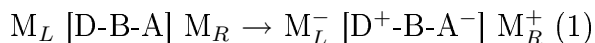
technology will reach a 18-nm node with 7-nm physical gate-length in a field-effect transistor (FET) by 2018 [165]. Further miniaturization of the CMOS feature size will likely face a roadblock due to the fundamental physical limits on the device size imposed by the laws of quantum mechanics obeyed by matter at nanometer-scale. Such an anticipated end of the Moore's curve, combined with recent advancements in instrumentation and experimental techniques to probe materials at molecular and nano-scale have attracted a great deal of attention in using organic and bio-molecules as active device elements.

The final goal of molecular electronics is to replace the role of semiconductors with molecules. Diodes and transistors are basic building blocks of an electronic architecture. In this chapter, we try to understand how these central functions can be fulfilled in molecular electronic devices. We will start with a brief introduction to what is already known and what needs further understanding.

Despite the congenital difference in the work mechanism of molecular electronic devices, where the electrons are confined to discrete energy levels, they are analogous to their semiconductor counterparts in many ways. The property of semiconductors that makes them most useful for constructing electronic devices is that their conductivity may easily be modified by doping impurities with a different valence. A donor (D) gives away some of its electrons (n-type), while an acceptor (A) withdraws weakly-bound outer electrons from the semiconductor atoms (p-type). Similarly, in organic compounds, the constituent groups of atoms may show different degrees of

electron affinity, depending upon their ability to withhold electrons. Whereby, they can also be distinguished as electron donors or acceptors. For example, in a molecule composed of one-electron donor and one-electron acceptor counterparts, the extent of charge separation varies from a value of 0 (a neutral state, D—A) to 1 as in zwitterions $D^+—A^-$.

Just like an n-p junction forming a diode, the first single-molecule diode proposed by Aviram and Ratner [2] seems to originate from a similar idea. The proposed molecule is composed of three parts D-B-A, where D is a good one-electron donor, i.e. n-type; A is a good one-electron acceptor, i.e. p-type; and B stands for a σ -bond bridge between D and A. The transport mechanism can be conjectured into two steps under a forward bias:



As shown in step (1), an electron tunnels from the right electrode M_R to A, and an electron tunnels from D to the left electrode M_L , leading to the zwitterionic excited state D^+-B-A^- . It is followed by a reversion to the neutral ground state D-B-A via an intramolecular charge transfer (step (2)). The ultimate result is that one electron is moved from M_R to M_L in this process. Following a similar logic for the reverse bias process, however, it requires that D works as an acceptor and A as a donor. A high energy barrier to an excited state D^--B-A^+ limits the electron flow.

Therefore, molecular rectification occurs. The D^+-B-A^- excited state is estimated to lie about 1-2 eV above the D-B-A ground state. The interplay of these two states is the foundation of the Aviram-Ratner model for a unimolecular diode [2].

The tenet of the Aviram-Ratner proposal is to illustrate the possibility of making unimolecular electronic devices with the same functionalities as semiconductor devices. Following this seminal work, there have been a number of theoretical and experimental studies on the electron transport through organic molecules with a D-B-A architecture in contact with semi-infinite metallic electrodes at the two ends [166, 21, 24, 26, 167, 168, 169, 170, 171]. While single-molecule architectures were shown to exhibit current rectification in several experiments [166, 21, 24, 26, 167], more recent theoretical studies have been unsuccessful in observing a discernible rectification effect in the Aviram-Ratner type of D-B-A single molecule architectures [168, 169, 170]. The failure to observe the diode behavior in D-B-A architectures from theoretical calculations has led some researchers to propose that the experimental observations of the unidirectional current in D-B-A architectures result from the asymmetric coupling between the molecule and the electrodes. In the Langmuir-Blodgett experiment, for example, an aliphatic chain is attached to one end of the molecule [168]; while in the STM experiment, one of the electrodes - the STM tip is only weakly coupled to the molecule [169].

In this chapter, we will clarify some of the controversies based on a study on the molecular rectification in a D-A substituted para-terphenyl system. The present

system differs from those of the AR model in the sense that the bridging moiety (B) is not a σ -bonded high-energy barrier structure. Rather we focus on a π -conjugated system to investigate the role of the charge distribution, presence of a permanent dipole moment due to the charge-separating D and A functional groups, and the effects of the external electric field on the energy-levels of the participating frontier orbitals. Another feature of our study is that the molecule is symmetrically and weakly coupled to the two electrodes without forming covalent bonds. This allowed us to eliminate the interfacial effects and focus on the electronic structure effects in molecule itself by conveniently isolating the molecular one-electron orbitals. We propose a new mechanism based on the fundamental property of a single molecule with D-A side groups - asymmetry in charge distribution and the permanent electrical dipole moment. Our study shows that an electron-transporting dipolar molecule will always exhibit an asymmetric current under opposite biases, while the magnitude of rectification in current depends on the details of the molecular electronic structure including spatial distribution of frontier orbitals, the effect of the external field on the frontier orbital charge distribution and the energy-level variation of these orbitals under the external potential.

Studies were then carried on to design a unimolecular transistor based on the architecture of a heterojunction bipolar transistor (HJBT) inherited from the microelectronics device designs of transistors. Based on our observation in the D-B-A diode system, the larger the polarization of the system under an applied field, the more effective the

electrical rectification is. We have designed a single-molecule transistor, where strong electrostatic coupling between the molecule and the gate is ensured, whereas only relatively weak coupling exists between the molecule and the source/drain electrode. The molecule consists of two diode units A-B-D and D-B-A interconnected by a π -conjugated capacitor (IC)- a terphenyl unit. It is symmetric along the source-drain direction (having a zero dipole component), while asymmetric in the gate direction (having a large dipole component). The idea is to translate the internal conducting states with respect to the pseudo Fermi level of the molecular system [172]. The application of a potential along the gate direction will significantly influence the current response according to this dipole-rule. The transistor behavior has been verified in such a unimolecular design. Depending upon the direction of the applied gate field, the electrical current from source to drain is either enhanced or depleted.

5.2 Simulation Model and Computational Details*

We have constructed a diode based on the D-B-A architecture with relatively weak D and A-character counterparts. As shown in Fig. 5.1(a), it consists of a D-A substituted para-terphenyl system, with 1,3-diaminobenzyl unit used as the donor (D) moiety and 1,2,4,5-tetracyanobenzyl as an acceptor (A) moiety bridged together

*Major part of Section 5.2 and 5.3 is reproduced with permission from H. He, R. Pandey, G. Mallick, and S. P. Karna, *J. Physical Chemistry C*, **in press**, (2009) Copyright©2009 The American Chemical Society

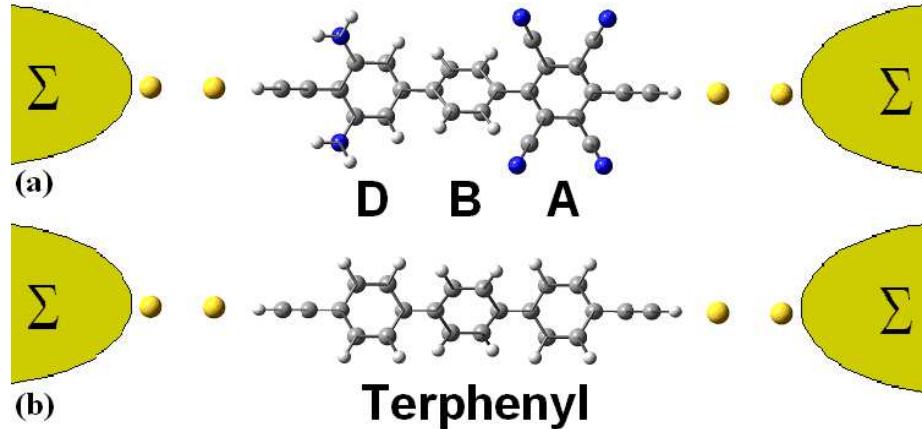


Figure 5.1: Schematic illustration of the extended molecules (a) $\text{Au}_2\text{-DBA-Au}_2$, (b) $\text{Au}_2\text{-TP-Au}_2$ coupled to the left and the right electrodes. The semi-infinite effect of the electrodes is included by the self-energy term Σ . The atoms are labeled as C in gray, N in blue, H in white and Au in yellow.

by the middle phenyl ring (B). The $I - V$ characteristics of such a system have been explicitly studied theoretically. As a control, we also performed similar calculations on a para-terphenyl (TP) molecule without the D and A side groups, as shown in Fig. 5.1(b). Thus, the D-B-A architecture and the control molecule both have the same π -conjugated backbone, differing only in the presence/absence of the donor ($-\text{NH}_2$) and the acceptor ($-\text{CN}$) functional groups at the outer phenyl rings.

We used Au as electrodes, as commonly employed in experiments and theoretical studies. Despite the fact that the metal electrode-organic molecule interface plays an important role in molecular-scale electronics, in the current study, however, we would focus on the roles played by the molecule itself. Further, in order to reduce the interface effects, we chose not to use the thiol group as the anchor of the molecule to the electrode, which is known [173, 174] to induce a large interfacial and intermolecular

charge redistribution, and is involved in the formation of frontier orbitals of the molecular system. Instead, we used the $\text{C}\equiv\text{CH}$ group to terminate the molecule at the end. The H-terminated geometry is an analogue to the Langmuir-Blodgett (LB) film deposited on a metal substrate, which is kept from direct contact with the metal electrodes. The H-Au distance is set to 2.0 Å, typical of the H-metal adsorption distance for several transition and post-transition-metal surfaces [175].

The electrical response of a molecular device was modeled under an external static electric field along the (source) D-B-A (drain) chain. It was applied in both positive and negative directions to distinguish the forward ($\text{A}\rightarrow\text{D}$) and the reverse ($\text{D}\rightarrow\text{A}$) biases. A two-Au atomic chain, i.e. 2 Au atoms in line separated by 2.90 Å (the bond length in Au bulk is 2.885 Å), was included in the central scattering region at both the left and right contacts in considering the screening length of Au electrodes.

The electronic structures were calculated in the framework of the density functional theory (DFT) with B3LYP functional form [123, 124] using Gaussian03 *ab initio* electronic structure code [127]. The core scattering region was simulated by the extended molecular complex ($\text{Au}_2\text{-DBA-Au}_2$) where atomic scale contacts were used for the molecule. The LanL2DZ basis sets were used for all atoms. A symmetry-constrained geometry optimization was performed for the zero field. At zero field, the dihedral angle between D and B rings is 35.2° , the dihedral angle between A and B rings is 53.2° . The larger dihedral angle between the A and B rings is due to the comparatively larger steric effect from the polar groups. In case of terphenyl,

the dihedral angle between rings is 32.21° . The zero-field geometry was then used for all the calculations in presence of the electric field, since the geometry change in the molecule under an external electric field is insignificant. For instance, under an electric field with a strength of 5.14×10^8 V/m, the maximum variance in the bond length is ~ 0.005 Å, in the bond angle $\sim 1^\circ$ and in the dihedral angles between two adjacent phenyl rings $\sim 2^\circ$. The current (I)-voltage (V) calculations were performed using the Green’s function-based Landauer-Büttiker formalism.

A single molecule was then designed for the purpose of working as a unimolecular transistor, combining two diode units A-B-D and D-B-A interconnected by a terphenyl unit (the IC part). A detailed description will be given in the section following the unimolecular diode study. Symmetry-constrained geometry optimization was done for the molecule at zero field and used for all the cases. The source-drain currents under a series of gating fields (applied along the direction of IC, perpendicular to the source-drain direction) were calculated on the same footing using the Landauer-Büttiker formalism.

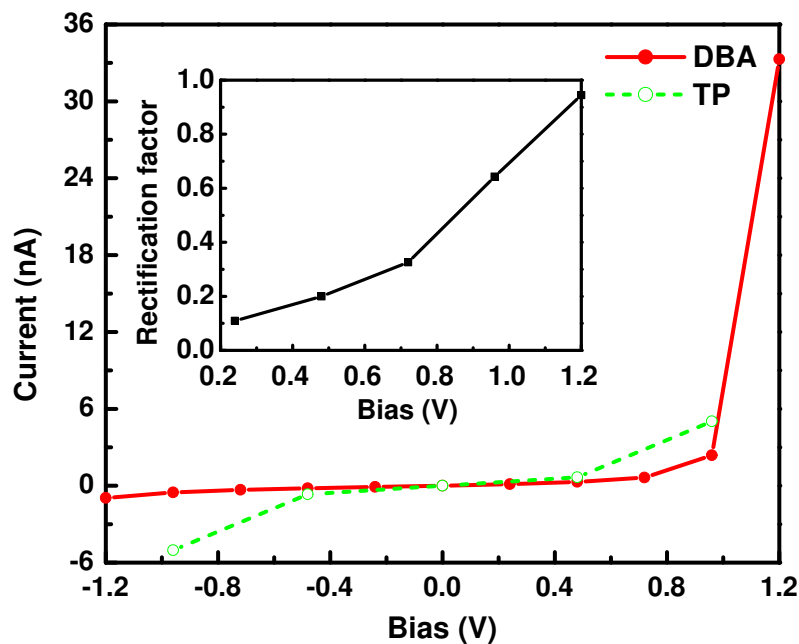


Figure 5.2: Current-voltage curves for DBA (in red solid circle and solid line) and TP (in green empty circle and dashed line). The calculated rectification factor for DBA is plotted in the inset.

5.3 Rectification Effect in a Donor-Bridge-Acceptor (DBA) Architecture

5.3.1 Asymmetric currents under forward and reverse biases

The calculated current for this D-B-A molecular system is plotted in Fig. 5.2. A significant rectification in the current is observed. As a figure of merit, the rectification ratio is defined as $\frac{I^+ - I^-}{I^+ + I^-}$, where I^+ and I^- are the currents under the forward and

the reverse bias, respectively. The calculated values are illustrated in the inset of Fig. 5.2. The rectification factor increases continuously with an increase in the bias voltage, and reaches 0.94 at a bias of 1.2 V. In contrast, the corresponding $I - V$ curve for the symmetric para-terphenyl molecule, as expected, shows highly symmetric characteristics.

5.3.2 Evolution of electronic structure under bias

Table 5.1: Summary of the dipole moments, the energy gap between the D/A frontier orbitals $\Delta(\epsilon_A - \epsilon_D)$ and the HOMO (due to the D group) energy with respect to the pseudo Fermi level $\Delta(\epsilon_D - E_F)$ of the extended molecule under a series of applied electric fields. The corresponding applied potentials are also calculated from the knowledge of the distance between two electrodes.

Field (10^8 V/m)	Applied potential (V)	Dipole moment (Debye)	$\Delta(\epsilon_A - \epsilon_D)$ (eV)	$\Delta(\epsilon_D - E_F)$ (eV)
-5.14	-1.20	-0.15	2.20	-0.50
-4.11	-0.96	0.45	2.12	-0.54
-3.09	-0.72	1.05	2.04	-0.58
-2.06	-0.48	1.66	1.96	-0.62
-1.03	-0.24	2.26	1.88	-0.66
0.00	0.00	2.87	1.80	-0.61
1.03	0.24	3.48	1.66	-0.53
2.06	0.48	4.09	1.64	-0.45
3.09	0.72	4.70	1.56	-0.38
4.11	0.96	5.32	1.48	-0.30
5.14	1.20	5.94	1.40	-0.22

In table 5.1, we list changes from several aspects. The dipole moment is a measure of charge separation in the extended molecule. It varies pronouncedly and almost linearly with the external field. The permanent dipole moment in this molecule

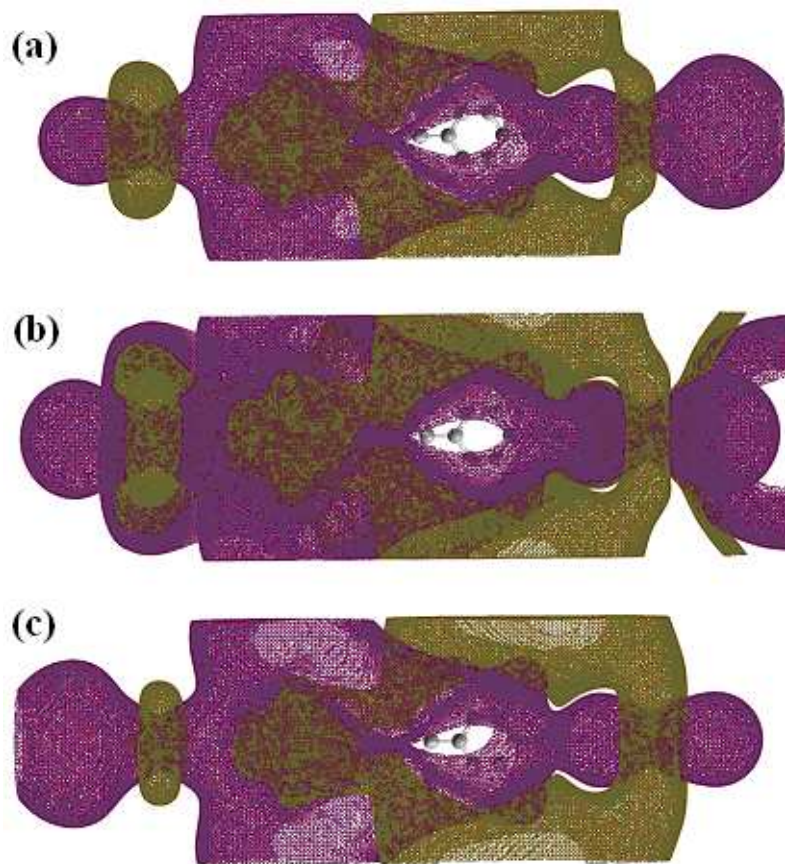


Figure 5.3: Electrostatic potential for DBA under a bias of (a) -1.20 V, (b) 0.00 V and (c) 1.20 V (excluding the linear potential drop due to the external electric field). The green surfaces correspond to the regions with a positive electrostatic potential energy of 0.1 eV, whereas the purple areas correspond to the regions with a negative electrostatic potential energy of -0.1 eV.

produces an internal electric field, due to the presence of the donor/acceptor end groups. The field strength is about the same order of magnitude as the external field under source-drain. When the applied electric field is parallel to the intrinsic dipole moment (from A to D), the molecule experiences an enhanced polarization compared to the case when the external field direction is reversed. This leads to asymmetry in polarization and in the magnitude of the current under applied opposite biases.

The variation in the electrostatic potential profile due to the intramolecular charge redistribution under bias is shown in Fig. 5.3. In contrast to this, the TP molecule does not have a dipole moment at a zero field and polarizes equally under an external field applied in either direction.

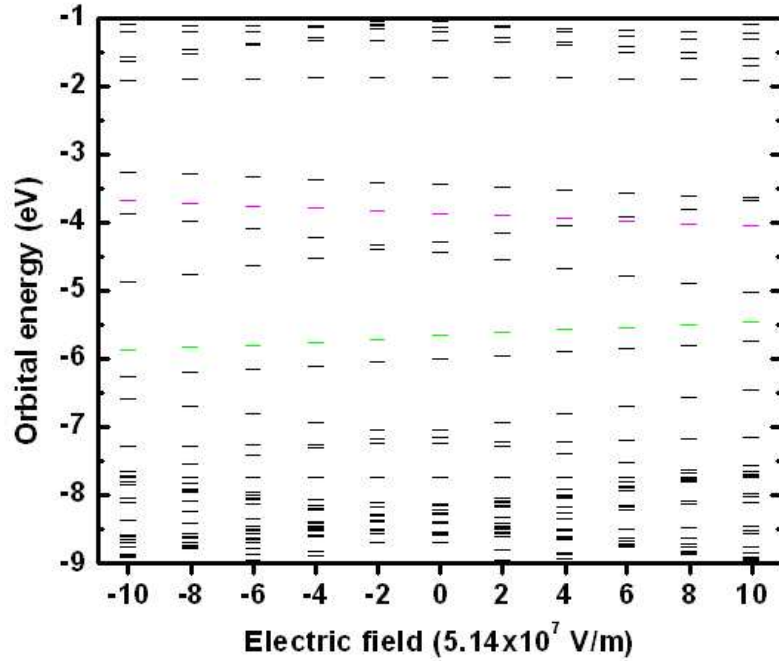


Figure 5.4: Molecular spectra of the DBA extended molecule under a series of external electric field. The HOMO orbital due to the donor group (D) is in green and the first DBA virtual orbital due to the acceptor group (A) is in magenta. The pseudo Fermi level E_F in each case is taken as the average between the HOMO (a D orbital, in green) and the LUMO (a Au orbital, in black) of the extended molecular system.

The molecular orbitals due to the donor and the acceptor are the frontier orbitals near the Fermi level (as shown in Fig. 5.4 and Fig. 5.5). If excluding the pure metallic

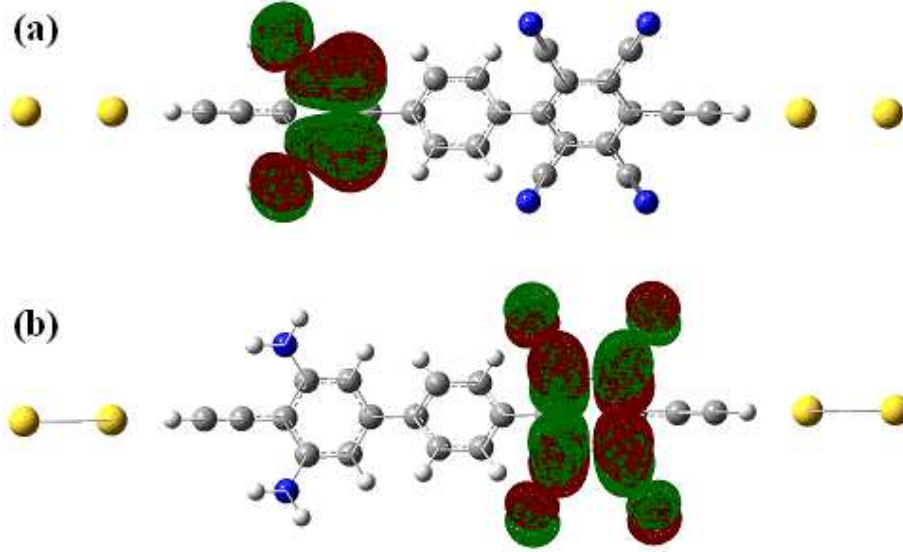


Figure 5.5: Plots of (a) the highest occupied (D-orbital) and (b) the lowest unoccupied (A-orbital) (excluding Au orbitals) molecular orbitals with the isovalue= $0.02 \text{ e}/\text{\AA}^3$.

orbitals from Au (LUMO and LUMO+1/LUMO+2), which do not contribute to the conductance of the molecule, the molecular orbitals from the D group are on the HOMO side (see Fig. 5.5(a)) and the molecular orbitals from the A group are on the LUMO side (see Fig. 5.5(b)). We see a continuous increase in the eigenvalue of the D orbital (HOMO) and a decrease in the A orbital (LUMO+2 for $E < 3.09 \times 10^8 \text{ V/m}$, or LUMO+1 for $E > 3.09 \times 10^8 \text{ V/m}$ due to the band cross) when the electric field varies from -5.14×10^8 to $5.14 \times 10^8 \text{ V/m}$. The wave characters of these orbitals, however, do not change with the applied external electric field in the range considered here. Therefore, the D-A orbital gap gets narrower with a positive applied field (along the A-D direction, i.e. p-n direction, forward bias) and opens up under a negative field (reverse bias). The values are also tabulated in Table 5.1. Overall speaking, our

results agree qualitatively with those of ref. [170] in the low bias range considered here. However, the results differ from those of ref. [171], where the narrowing of the HOMO-LUMO gap in both field directions were reported. It is worth noting, though, that despite a narrowing of HOMO-LUMO gap in either direction reported in ref. [171], the magnitude of the change due to the positive and the negative biases are different. This difference turns out to be critical in observing asymmetric current for the two opposite biases [171].

Nevertheless, this D-A gap does not close up to a positive bias of 5 V, suggesting a high barrier to the zwitterions excited state D^+-B-A^- , which implies that the Aviram-Ratner diode model cannot apply in this case. Furthermore, the Fermi level remains more or less the same, due to the Fermi pinning by the Au orbitals lying in the D-A gap.

5.3.3 Transmission functions under bias

In the low bias regime, as we have considered here, the dominant contribution to molecule conductance comes from the D orbitals (HOMO side), because the A orbitals are far above the pseudo Fermi level. Our analysis of the HOMO molecular orbital, which is attributed to the donor (D) group, shows that its wave character changes very little with the varying electric field in the range considered here. So does the character of the A orbital on the LUMO side. This observation again emphasizes the

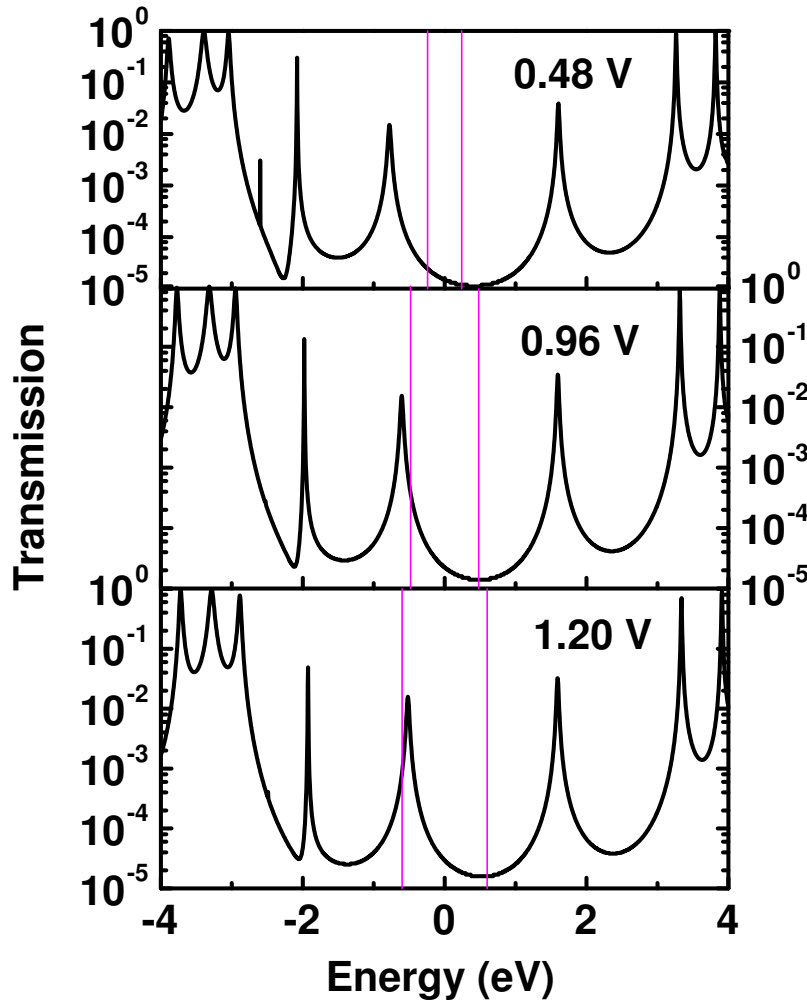


Figure 5.6: Transmission functions for DBA under a series of forward bias. The bias windows are shown in magenta lines. The pseudo Fermi level is aligned to zero.

difference in electron transport mechanism in this system and that considered in the Aviram-Ratner proposal. Instead, the position of the HOMO gets closer to the Fermi level as the positive electric field (forward bias) increases, whereas it gets further away from the Fermi level with increasing the negative field (reverse bias). Transmission

functions are shown in Fig. 5.6 for a series of biases. It is clearly seen that the resonance peak in transmission function due to the HOMO (or D) orbital is far away from the bias window at a bias of 0.48 V; approaches closer to the bias window at a bias of 0.96 V, and the tail of that peak starts to contribute to current; and falls into the bias window at a bias of 1.20 V, giving rise to a dramatic increase in current. The current is rather flat under the reverse bias within 1.00 V, and starts to lift up a bit at a bias of 1.20 V. This results in the current rectification in this system. In contrast, the HOMO-LUMO gap changes symmetrically under a forward/reverse bias in the use of TP molecule, which does not show any change upon a forward or a reverse bias. The intrinsic dipole moment of a polar molecule leads to the asymmetric variation in the energies of the D and A orbitals (especially D in this DBA case) under the forward and reverse bias, and thereby the asymmetric electrical response. It is worth noting that the sulfur atoms used for Au-molecule attachment in other studies [170, 171] reduces the dipole moment and smears out the asymmetry of charge distribution, thereby reducing the magnitude of rectification of the overall molecular system. The reason, which has seldom been called to attention before, is that the S atom also acts as a good electron donor [176]. Thus the presence of the S atom as a molecule-metal binder has a strong influence not only on the molecule-electrode chemical bonding but also on the intramolecular charge redistribution.

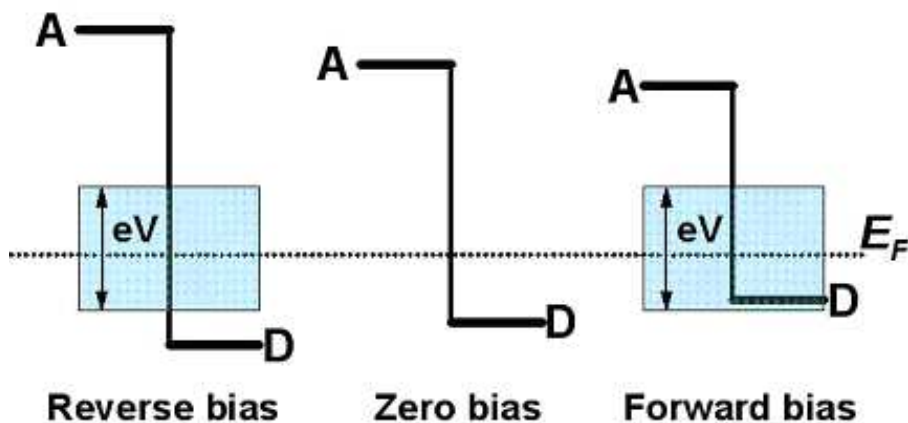


Figure 5.7: Illustration of current rectification mechanism in a D-B-A type of molecule with weak donors and acceptors. The bias window is shown in light blue.

5.3.4 Electronic structure mechanism - the dipole-rule

We would like to point out that the current study is based on an assumption of the symmetric potential drop on both electrode sides. The rectification effect we have seen here is owing to the polarity and therefore the dipole moment of the molecule itself, which along with the one-electron frontier orbital energy levels, experience enhanced modulation in the presence of an external electric field, leading to a unidirectional current flow. The electronic structure mechanism of the current rectification is shown in Fig. 5.7. In these energy diagrams, we have drawn the frontier orbitals due to the D and A groups under zero and non-zero electric fields corresponding to the forward and reverse biases, as well as the bias window in each case. At zero bias, the HOMO, due to the D group is much closer to the pseudo Fermi level. And under a forward bias, the D-A gap shrinks and the D orbital moves into the bias window contributing

to the total current; whereas under a reverse bias, the D-A gap widens and both the D and A orbitals are even further away from the bias window. The different response under opposite applied fields, leads to the rectification effect through the molecule.

It is also important to note that the effectiveness of the rectification process depends on the distribution of the frontier molecular orbitals arising from the D and A side groups as well as on the polarizability of the system under an electric field. If the HOMO-LUMO gap of the system is too large, a significant rectification in current may not be observed until a high bias voltage is applied [170]. Similarly, if the system is good in screening the applied electric field and induces a relatively small change in the dipole moment, the rectification effect will again be small [171, 177].

5.4 Transistor Behavior in an ABD-IC-DBA Architecture[†]

The most challenging and difficult goal of molecular-scale electronics has been the realization of a three-terminal molecular transistor, which can switch current across two arms by an external electric field modulation through the third arm of a single molecule. Switching effects in architectures consisting of hybrid molecular diodes,

[†]Reproduced with permission from H. He, R. Pandey, and S. P. Karna, *Nanotechnology*, **19**, 505203 (2008) Copyright©Institute of Physics and IOP Publishing Limited 2008

[†]Reproduced with permission from H. He, R. Pandey, and S. P. Karna, *Nanotechnology*, **19**, 505203 (2008) Copyright©Institute of Physics and IOP Publishing Limited 2008

where tunnel current through the molecule is modulated by chemical gating, has been demonstrated recently [178], although the underlying theory is not yet established.

There have also been reports of three-terminal devices using C_{60} fullerene molecules [179, 180], carbon nanotubes [34, 181], organic self-assembled monolayers [182], organic molecules such as benzene-1,4-dithiolate [183, 184], and transition metal coordination complex [185], in which the source-drain current is controlled by voltage through a physical electrode in contact with the molecule.

In the present study, we explore the possible means of combining both D and A substitutions to control the functionality of the molecular transistor. As we have found in the last section in the study of D-B-A type of diodes, substitution by electron donating (D) or electron withdrawing (A) groups can effectively tune the electronic behavior of organic molecules and either lead to a simple shift of the electron transmission or to a more complex resonance effect [186]. A novel, three-terminal architecture is proposed here, which is analogous to the heterojunction bipolar transistor (HJBT). In this architecture, two diode arms consisting of donor-acceptor molecular wires fuse through a ring and a base or modulating wire is a π -conjugated wire. The design of this unimolecular transistor further allows us to have a strong electrostatic coupling between the molecule and the gate, but a relatively weak coupling between the molecule and the source/drain electrode which is highly desirable in a three-terminal transistor architecture.

5.4.1 Molecular design and simulation model

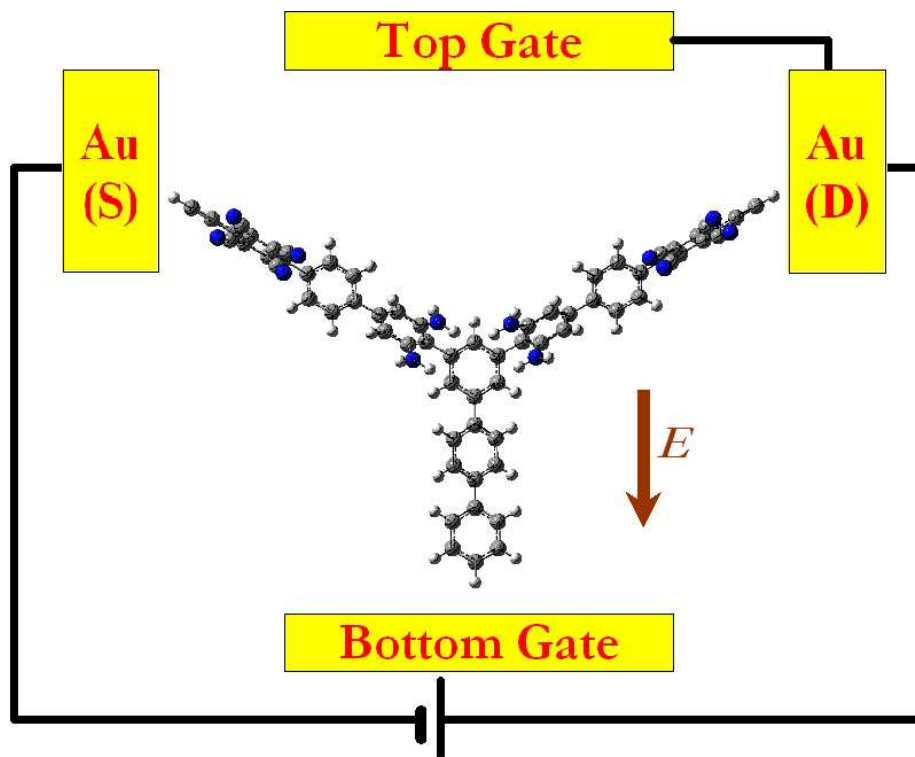


Figure 5.8: Schematic illustration of the setup of a unimolecular transistor ABD-IC-DBA in measurement. C atoms are in gray, N in blue, H in white, and Au in yellow. In this diagram, a positive bias is applied upon the source (S) and the drain (D) termini, where the drain has a higher potential (i.e. a lower potential energy). A top-and-bottom double gate is applied generating a uniform positive gate field E pointing downward in the same direction as that of the intrinsic dipole moment of the entire molecule.

In this study, we have constructed a transistor based on the bipolar-junction architecture inherited from the microelectronic devices. The proposed unimolecule consists of two diodes A-B-D and D-B-A (see the last section for details) interconnected by an insulating capacitor (IC) - a terphenyl molecule, see Fig. 5.8. The latter is supposed to be capacitively coupled to the third terminal - the gate, although it does not

physically connect to any metallic electrode. The entire molecule is fully optimized under symmetry-constraint before adding the electrodes.

Similar to the diode study, we have used Au electrodes in this work. To eliminate the interfacial effects, we avoid using the most common thiol group as the anchor of the molecule to the electrode. Instead, the $\text{C}\equiv\text{CH}$ group is used on both the source and drain termini. More details can be found in the previous diode section. No realistic form of a gate electrode is put near the terphenyl molecule. The gate effect is simply simulated by an external electric field along that direction. Both positive and negative (defined as the same and the opposite direction of the dipole moment of the entire molecule, respectively) fields are considered in the current study and it is shown that the gating effect strongly depends on the direction of the electric field.

The source-drain current is based on the two-terminal assumption, since the third terminal does not affect the overall current much (negligibly small leakage current), but only affect the circuit by electrostatic potential coupling. The core scattering region was simulated by the extended molecular complex ($\text{Au}_2\text{-ABD-IC-DBA-Au}_2$) where atomic scale contacts with two Au atoms in line with the ABD or DBA on either side were used for the molecule. The electronic structure and current calculations were done using the same approach as for the DBA diode case (see section 5.2 for details).

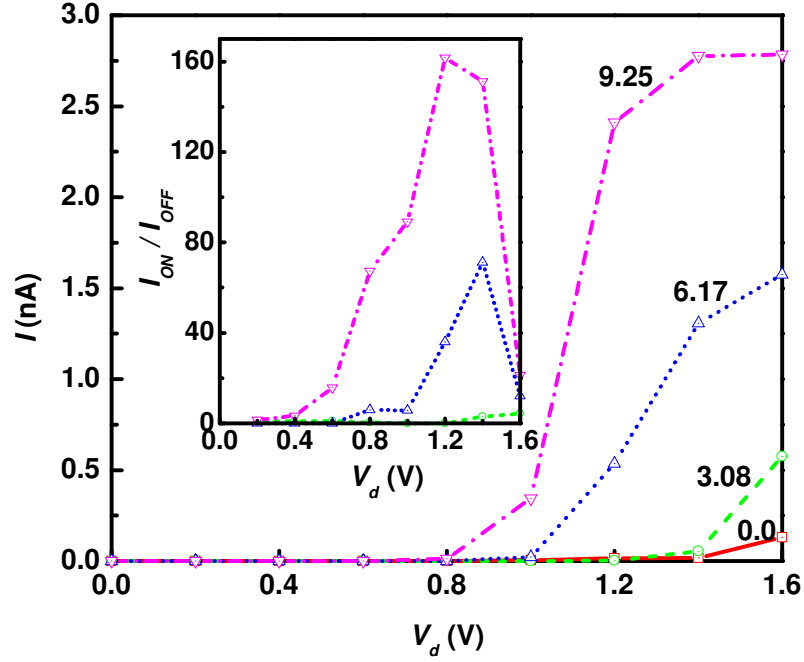


Figure 5.9: $I - V$ curves for the molecular system under an applied positive gate electric field (labeled) in the range of 0.0 to 9.25×10^8 V/m. The calculated modulation factor I_{ON}/I_{OFF} is also plotted in the inset.

5.4.2 Tunneling current - enhancement/depletion gating effect

Since in such an architecture, the designed molecule is symmetric with respect to source and drain, but asymmetric in the gate direction, the disturbance of the source-drain bias on the electronic structure of the system is much smaller than the effect of the gate potential. So the variation of source-drain current with source-drain voltage is calculated at fixed gate electric field, without applying a field in the source-drain direction in the simulation. The calculated current (I) vs. drain voltage (V_d) curves

under a various range of gate potential are plotted in Fig. 5.9. The electric field due to the gate potential varies from -9.25 to 9.25 ($\times 10^8$ V/m). If we take the top-bottom gate distance to be around 32 Å, then the maximum gate potential (V_g) considered is about 3 V. For a low bias (< 1.4 V) without applying a gate field, the current is found to be negligibly small. As the bias increases, however, the current tends to increase because of resonant tunneling. An enhancement in current is observed for the positive gating, but a depletion in current for the negative gating (not shown in Fig. 5.9).

Under positive fields, one notes a coulomb gap and then a sudden increase in the $I-V_d$ curves. The current gets saturated when the drain-source voltage is further increased. The coulomb blockade is due to the weak coupling (no chemical bonding) between the molecule and the source and drain electrodes, where the molecule works as a quantum dot. The increment and saturation of current result from resonant tunneling due to certain molecular orbitals. We will discuss it more in detail in the next two sections. Changing the gate electric field from 0 to 9.25×10^8 V/m, one can observe switching from a non-conducting state to a conducting state for a small source-drain potential (in the range of 0 to 1.4 V). The modulation of current (ON/OFF ratio) also increase drastically with an increase in the gate potential, shown in the inset of Fig. 5.9. It reaches a maximum of about 70 for a gate of 6.17×10^8 V/m ($V_g \approx 2$ V) and 160 for a gate of 9.25×10^8 V/m ($V_g \approx 3$ V) at a drain voltage around 1.4 V. A gate field of 3.08×10^8 V/m ($V_g \approx 1$ V), however, is not enough for switching on the

current, general speaking. These values are significant for a transistor working in an enhancement mode. Under negative fields, the total current is even further reduced, suggesting a depletion working mode.

5.4.3 Molecular orbital energy shift - polarization effect

While maintaining a symmetric arrangement along the source-drain direction, the polarity along the gate direction, produces a permanent dipole moment in that direction, which ensures the strong electrostatic coupling between the molecule and the gate. And in the current molecular design, the polarizability of the entire molecule is magnified by connecting two p-n junctions (the ABD molecules) tail to tail.

Table 5.2: Summary of the total energy, the dipole moment, and the HOMO (due to the D group) energy with respect to the pseudo Fermi level $\Delta(\epsilon_D - E_F)$ of the extended molecule under a series of applied electric fields along the gate direction. The corresponding applied gate potentials are also calculated from the knowledge of the distance between the top and the bottom gates, which is assumed to be 32 Å*.

Field (10^8 V/m)	Gate Potential* (V)	Energy (hartree)	Dipole moment (Debye)	$\Delta(\epsilon_D - E_F)$ (eV)
-9.25	-3	-3733.596496	0.43	-0.88
-6.17	-2	-3733.596802	2.16	-0.76
-3.08	-1	-3733.597518	3.90	-0.65
0.00	0	-3733.598644	5.64	-0.53
3.08	1	-3733.600182	7.39	-0.41
6.17	2	-3733.602135	9.15	-0.30
9.25	3	-3733.604504	10.92	-0.18

In table 5.2, we tabulate the energetic and electronic structure changes under a varying

gate field. As a label of polarization of the molecule along the applied gate field, the dipole moment in this molecule varies significantly and almost linearly with the external electric field. The positive field enhances the dipole moment, and lowers the energy of the system, while the negative field reduces the dipole moment and increases the total energy.

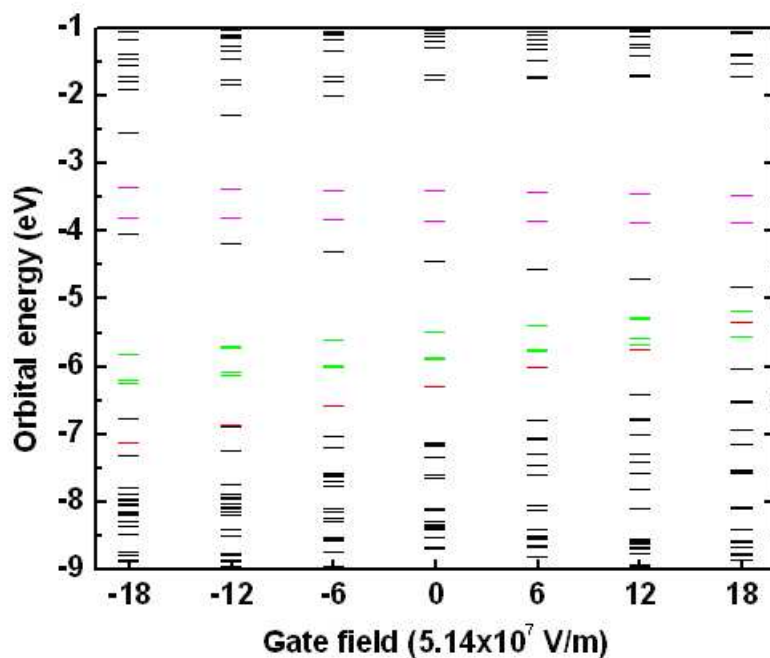


Figure 5.10: Molecular spectra of the $\text{Au}_2\text{-ABD-IC-DBA-Au}_2$ extended molecule under a series of gate fields. The highest occupied orbitals due to the donor group (D) are in green; the lowest unoccupied orbitals due to the acceptor group (A) are in magenta; the highest occupied orbital due to the IC molecule is in red.

The evolution of molecular orbital eigenvalue spectra is plotted in Fig. 5.10. The molecular orbitals due to the donor and the acceptor are the frontier orbitals near the

Fermi level. If excluding the pure metallic orbitals from Au (LUMO and LUMO+1, 2-fold degenerate), which does not contribute to the conductance of the molecule, the molecular orbitals from the D group are on the HOMO side and the molecular orbitals from the A group are on the LUMO side. We can see a continuous increase in the eigenvalue of the D orbitals (HOMO and HOMO-1 in 2-fold degeneracy; HOMO-2 and HOMO-3 for $E \leq 6.17 \times 10^8$ V/m, or HOMO-3 and HOMO-4 for $E > 6.17 \times 10^8$ V/m due to the band cross with a small energy split), while the A orbitals (LUMO+2 and LUMO+3 in 2-fold degeneracy; LUMO+4 and LUMO+5 in 2-fold degeneracy) slightly decrease when the electric field varies from -9.25×10^8 to 9.25×10^8 V/m. Therefore, the D-A orbital gap gets narrower with a positive field (enhancement mode) and opens up under a negative field (depletion mode).

In the low bias regime, as we have considered here, the actual contribution to molecule conductance comes from the D orbitals (from the HOMO side), because the A orbitals are far above the Fermi level. Since the polarization effect induced due to the positive gate potential floats the molecular energy levels up (Table 5.2), the molecular resonant states reach earlier than the one with no or smaller gate potentials. This partially accounts for the switching effect in the $I - V_d$ curve upon the application of a positive gate potential. Vice versa, the application of a negative gate potential drops the molecular energy levels down, and therefore the molecular resonant states cannot be reached until a higher drain- source potential. Thus a suppression of current is observed for all the negative gate fields.

5.4.4 Evolution of molecular orbital wave characters - gate molecule intervention effect

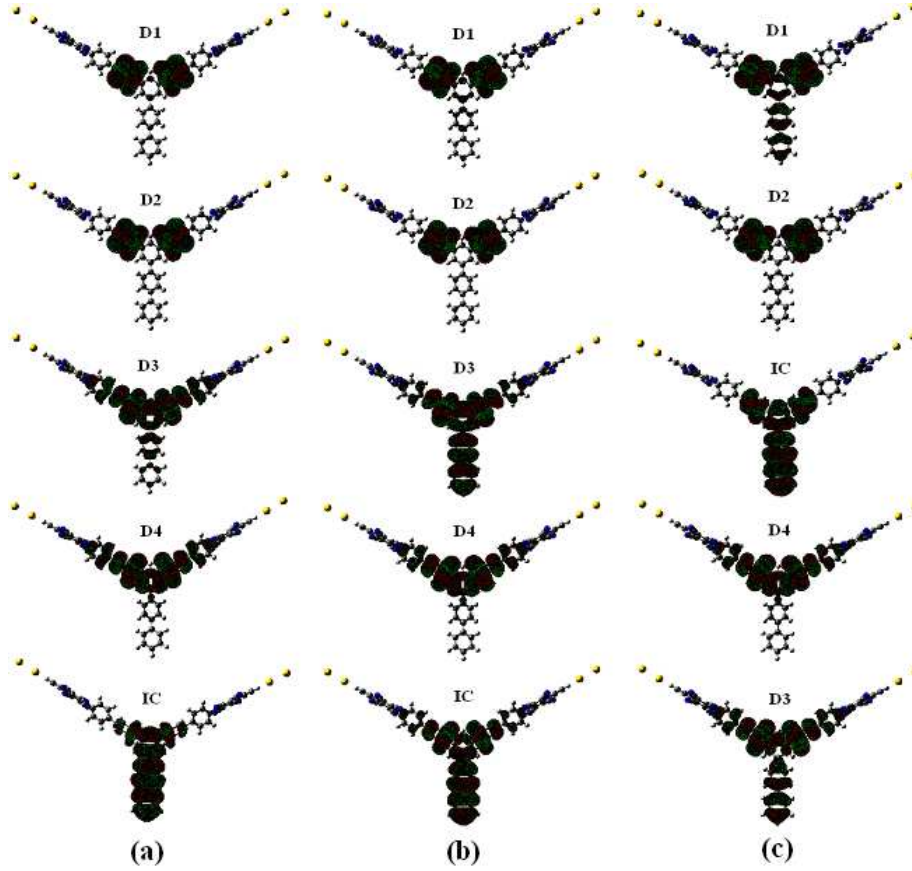


Figure 5.11: Evolution of molecular orbitals of the $\text{Au}_2\text{-ABD-IC-DBA-Au}_2$ extended molecule under a series of gate fields: (a) 0 V/m, (b) 6.17×10^8 V/m and (c) 9.25×10^8 V/m. The highest occupied orbitals due to the donor group (D) are labeled in sequence of D1, D2, D3 and D4. The highest occupied orbital due to the IC molecule is labeled as IC.

Very different from what we have found in the diode case, the analysis of the molecular orbitals reveal a significant evolution of the wave function with the varying electric field in the range considered here, as shown in Fig. 5.11. The orbital due to the IC

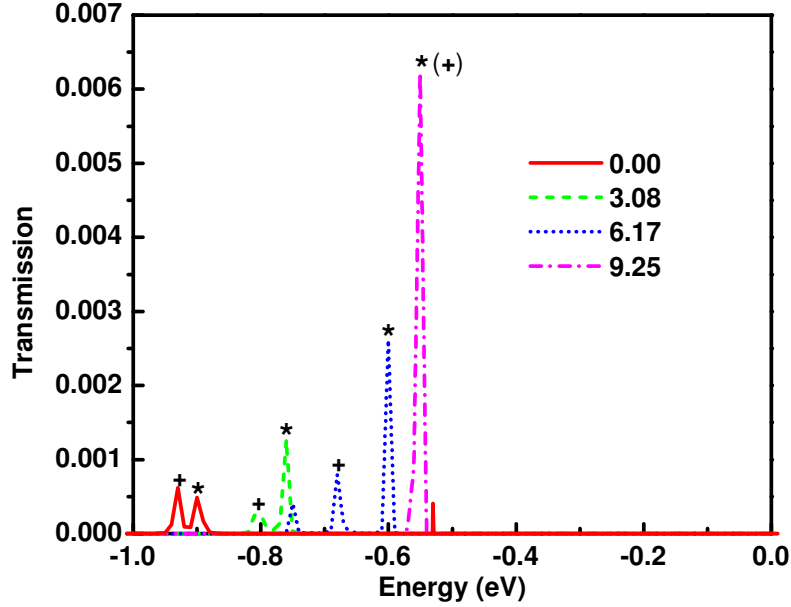


Figure 5.12: Transmission functions for the ABD-IC-DBA molecular system under a series of gate fields (labeled in the figure in unit of 10^8 V/m). The transmission peaks due to the second pair of the highest occupied D orbitals D3 and D4 are labeled by * and +, respectively. The pseudo Fermi level is aligned to zero.

molecule (highlighted in red in the Fig. 5.11) lies below the four D orbitals (labeled as D1, D2, D3, and D4 in sequence, the highest occupied orbitals due to the D group) near Fermi level at zero field, and moves even further down as a negative field increases in magnitude, but floats up as a positive field is applied, mixes significantly with the D orbitals (especially the antisymmetric wavefunctions D1 and D3) at a field of 6.17×10^8 V/m and lies above the second pair of D orbitals (D3 and D4) at a field of 9.25×10^8 V/m. It is found that this orbital has a strong influence on the wave character of the D orbitals, which again determine the electron transmission property

of the molecule. In general, the lift-up of the IC orbital brings more terphenyl-ring component to the D wavefunctions.

The consequence, however, is rather controversial. Note that the D-D connection is via one of the benzene rings. The transmission of electrons requires the delocalization of the wavefunction, therefore the bridging ring's contribution in the corresponding wavefunction. It, in turn, requires a certain amount of terphenyl-ring component in the D wavefunctions. Nevertheless, a strong terphenyl-ring character may otherwise work as an electron trap, making electron transmission difficult (see the small transmission peak due to the IC orbital with most contribution from the terphenyl rings). We can see this from the variation of the magnitude of the transmission peaks in Fig. 5.12, although it is out of our capability to quantize this effect at this point. The transmission peaks due to the first pair of D orbitals (D1 and D2) are rather small because of the strong localization of the molecular wavefunctions. The increase in the IC component in D1 with an increase in the gate field, however, does not make it significantly more conductive. The transmission peaks due to the second pair of D orbitals (D3 and D4) makes the most contribution to the conductance of the molecule, and corresponds to the steep increase in current and thereafter the plateau of current (saturation). The transmission probability increases with an increase in the terphenyl-ring character in the corresponding wavefunction under an increasing gate electric field. The transmission due to the IC wavefunction alone is again very small due to the strong localization. But when a large mixing between IC and D3 exists

at a gate field of 6.17×10^8 V/m, a relatively strong transmission peak appears at -0.6 eV, see Fig. 5.12. This observation suggests that the terphenyl molecule, in this case, works more than just a passive capacitor electrostatically coupling the molecule to the gate. Its intrinsic character in molecular orbitals plays an active role in the enhancement gating.

5.5 Summary

In summary, the electron transport properties of modeled single-molecule systems have been investigated in the framework of Landauer-Büttiker formalism using DFT and Green's function methods. The diode behavior is observed in a D-B-A architecture in the absence of redox reaction (zwitterionic state). The electrical rectification is found to result from its intrinsic dipole moment, which makes the molecule respond differently when the direction of the source-drain field changes. Under a forward applied potential (in the same direction as that of the permanent dipole), the polarization of the molecule is enhanced, the energy gap between the D and A frontier orbitals narrows and the electronic current increases rapidly; whereas under a reverse applied potential, the polarization of the molecule is reduced, the D-A energy gap widens and the current remains small. This leads to the asymmetry in the $I - V$ curve.

We have proposed to realize the enhancement and depletion mode of a transistor in

a designed single molecule with an architecture of ABD-IC-DBA. The asymmetric spacial structure leads to a sensitive coupling to electric field produced by the gate voltage. The source-drain current is affected not only by the magnitude, but also by the direction, or the sign of the gate potential. One way enhances electric signal, but depletes the other. The evolution of wavefunctions in the presence of the gate-coupling molecular part as well as the shift in molecular orbital energies result in the enhancement of source-drain current.

This study conveys an important message of the rich possibilities of using organic molecules in electronic devices by molecular design and engineering based on the fundamental properties of molecules.

Chapter 6

Modified Nanopore DNA Sequencing - Functionalization of Electrodes

6.1 Introduction

DNA sequencing is the determination of the sequence of nucleotides in DNA. Knowledge of a patient's DNA sequence may allow for the deduction of an immense amount of information about the health prospects of that person [187]. On the one hand certain genetic patterns in the sequence can indicate a higher risk to fall ill with a particular disease [188, 189]; an early recognition of such risks may allow for preventive counter measures that can either reduce the risk factor, or, via frequent monitoring of the patient, enable a timely treatment when first symptoms of the disease become ap-

parent. On the other hand, patients who are already suffering from a certain sickness may be treated more specifically with "personalized medicine" [190] that has been "custom-made" by considering the genetic characteristics of that person (or group of persons) and thus maximizes the positive effects of the drug components while simultaneously keeping negative side effects to a minimum. Besides these potential benefits for a particular group of patients, there is also the additional advantage for the research community in having the sequences from many individuals available for statistical studies and comparison of genomes [191]. Such a database can be used to analyze mutations [192] and hereditary diseases.

Therefore it would certainly be worthwhile to be able to read the DNA sequence of a patient rapidly and at a low cost. The recently proposed aim is to have one person's genome within one day at a cost less than \$1,000 [191]. DNA sequencing is, however, currently still a vastly time-consuming and very expensive task using the conventional gel-electrophoresis method consisting of pre-processing steps, the actual sequencing using the Sanger method, and the post-processing in the form of data analysis [187]. It takes about \$1,000,000 and at least several months to sequence a single human genome [193]. The further refinement and improvement based on the current technology is unlikely to achieve the "personal genome" goal. A fundamental obstacle is the read-length limit using electrophoresis, which is on the order of 1000 bases [194], in contrast to a whole human genome of 3.2×10^9 base-pairs to be sequenced.

The new possibility of passing a single-stranded DNA (ssDNA) through a so-called

"nanopore" with a diameter of only a few nanometers has been explored over the past decade [195, 196, 197, 198, 199] for the purpose of DNA sequencing. As the nucleotides of DNA are migrating through the membrane, they will partially block the pore in different ways depending on their size [200]. Thus, monitoring the ionic blockade currents could lead to the determination of the DNA sequence [198, 201]. To resolve the remaining ambiguity between the pyrimidine bases cytosine (C) and thymine (T), and the purine bases adenine (A) and guanine (G), it was recently suggested [64, 202, 203] that one could embed electrodes in the walls of a solid-state nanopore. By applying a bias voltage across the electrodes a small electric current perpendicular to the DNA strand can be measured. Thus as the ssDNA translocates through the pore, time-dependent current-voltage signals from the electrodes would supposedly be specific enough to allow the unequivocal identification of the nucleotide sequence. It is, however, still unclear whether or not the resulting current-voltage signal from pore-embedded electrodes is sensitive enough to reliably distinguish the four nucleic acid bases of DNA. The probability distributions of current signals for different nucleotides are found to overlap significantly [65, 66] largely due to the structural fluctuations of nucleotides between the embedded electrodes, which makes a reliable distinction of the different bases rather difficult. Although it may be possible to resolve the nucleic acid bases by applying a much smaller driving field and using statistical analysis [66, 67], this approach requires a relatively large number of independent electrical current samplings of a given base. Even so, the resulting probability distributions of

the signal currents span only one order of magnitude [67], which may not be good enough for an accurate sequencing run in a realistic setup.

In this study, we propose a new approach that relies on functionalized nanopore-embedded electrodes to achieve an unambiguous distinction of the four nucleic acid bases in the DNA sequencing process. A probe molecule is anchored at one of the electrodes. It has two roles to fulfill: to stabilize the coming-in nucleotide (the target) and to increase the sensibility of distinguishing different bases. The transport properties of the setup investigated by us, employing state-of-the-art density functional theory (DFT) together with the non-equilibrium Green's Function (NEGF) method, lead to current responses that differ by at least one order of magnitude for different bases. These results are intriguing in that this approach would potentially achieve base contrasts large enough to discriminate the four DNA bases.

6.2 Simulation Model and Computational Details*

6.2.1 Simulation model

A schematic illustration of the key elements of the proposed sensing device is shown in Fig. 6.1. It consists of two gold electrodes embedded oppositely in a nanopore;

*Section 6.2 and 6.3 are reproduced with permission from H. He, R. H. Scheicher, R. Pandey, A. R. Rocha, S. Sanvito, A. Grigoriev, R. Ahuja, and S. P. Karna, *J. Physical Chemistry C*, **112**, 3456 (2008) Copyright©2008 The American Chemical Society

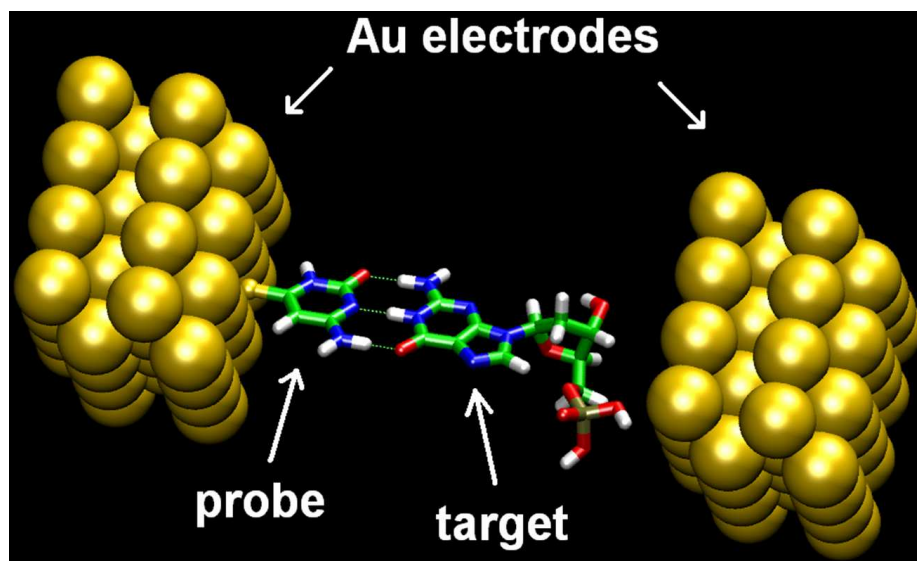


Figure 6.1: An illustration of the proposed device: ssDNA is passing through the nanopore with functionalized gold electrodes embedded. A probe molecule (e.g. Cytosine) is immobilized on the inner surface of the left electrode by a sulfur atom. As part of the ssDNA molecule, a Guanosine monophosphate unit is shown as the target to be identified.

a chosen DNA probe molecule anchored to the inner surface of one of the electrodes via a thiol group; and a target which is a segment of a ssDNA including base, sugar and phosphate group. Since the ions and water can effectively screen the charge on the phosphate group in a solution [67], it is kept uncharged. As a ssDNA is pulled through the nanopore via a driving electric field, the probing molecule will simultaneously fulfill two functions: (i) stabilization of the target base in the DNA sequence by forming weak hydrogen bonds, and (ii) detection of the target base by coupling electronically to it.

We have investigated four possibilities for the probe base molecule based on the four nucleic acid bases occurring in natural DNA, namely Adenine (A), Cytosine (C),

Guanine (G), and Thymine (T). The probe molecule is anchored by a sulfur atom at the hole site of Au(001) surface. The orientation of the probe molecule, however, is assumed to have the H-bonding edge parallel to the electrode surface. Due to the apparent difference in the size of the four bases, distance between the two electrodes is changed according to the size of the probe base ensuring the current measurements within the same detecting scale. However, for the same probe, the electrode-electrode distance is kept fixed at the same value. For example, the distance between electrodes was 2.27 nm when the purine base A or G works as the probe, and 2.18 nm in the case of the smaller pyrimidine base C or T as the probe.

The molecular probe couples electronically only to a single nucleotide at a time. Therefore, it is sufficient to include only a fraction of the ssDNA molecule, namely one nucleotide (a DNA base terminated by the phosphate-sugar backbone) in the central scattering region of our transverse electron transport calculations. The contributions from neighboring bases are negligibly small in the setup chosen by us due to the large vacuum space between the electrode and the molecular part positioned off the probe. Depending upon the size of the target base, the vacuum length left between the right-side of the DNA molecule and the right electrode will be different.

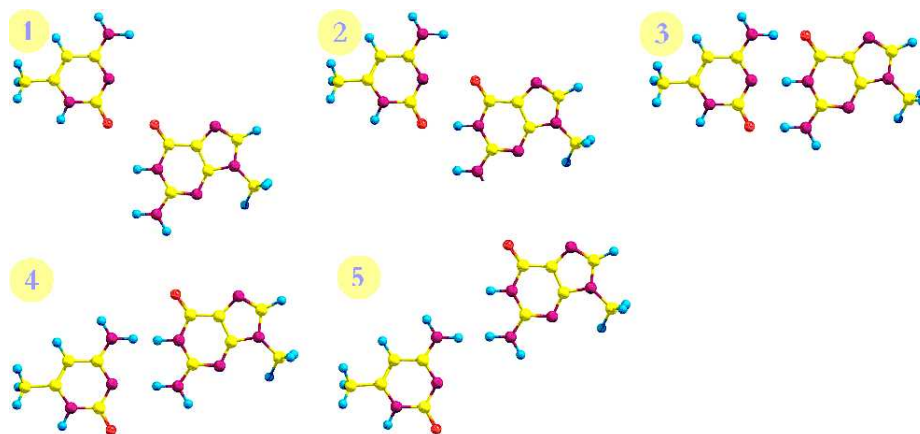


Figure 6.2: Five initial C-G base-pairing geometries.

6.2.2 Electronic structure and geometry optimization

We have started our investigation by determining the most stable pairing geometries between the probe and the target molecule. The pairing geometry between the probe and the target molecule is obtained by carrying a full optimization of an isolated pair of two bases terminated by methyl groups. For each pair, five initial positions were considered corresponding to the five matching position at the H-bonding edge (Fig. 6.2). We used the parameterization of Perdew, Burke and Ernzerhof (PBE) [121] for the exchange-correlation functional, and norm-conserving pseudopotentials [134] with nonlinear core correction [204]. The employed reference configuration was $2s^2 2p^2 3d^0 4f^0$, $2s^2 2p^3 3d^0 4f^0$, $2s^2 2p^4 3d^0 4f^0$, $3s^2 3p^4 3d^0 4f^0$, $1s^1 2p^0 3d^0 4f^0$, for C, N, O, S and H respectively. Valence wave functions were expanded in a SIESTA localized basis set (numerical localized pseudo-atomic orbitals) [205]. The finite range of the orbitals was defined by an orbital confinement energy [129] of 50 meV. We used a

double-zeta basis set with polarization orbitals on all the atoms [205]. The resolution of the real-space mesh was defined by a 150 Ry cutoff, assuring energy and force convergence. The tolerance in maximum density matrix difference is 10^{-5} and the tolerance in maximum atomic force is 0.04 eV/Å.

The optimized structures of base pairs are then used for transport calculation after substituting the methyl group with the phosphate-sugar backbone. The orientation as well as the structure of the phosphate-sugar is taken from the experimental structure of poly-nucleotides [206, 207] and kept fixed for all the four nucleotides.

6.2.3 NEGF quantum transport formalism

Under the assumption of coherent transport, the electronic transport calculations for such a molecular system coupled to Au electrodes (Fig. 6.1) are calculated from the non-equilibrium Green's Function method based on the Keldysh formalism, encoded in SMEAGOL [208, 49, 96], which has been successfully applied to the study of electron transport in molecular systems. The semi-infinite electrodes act as charge reservoirs with electrons following the Fermi-Dirac distribution under a certain temperature (300 K in this case). A central scattering region is defined to include four to six 4×4 **R** Au layers along the (001) direction on either side of the electrodes as well as the DNA probe-target bases in a periodic supercell. This region is chosen to enclose the significant change in the electronic structure due to the presence of an

external bias voltage. And the left and right electrodes outside this region are ensured to be not affected by the rearrangement within this region owing to the short screening length of Au [209]. The semi-infinite effect of the left (right) electrode is taken into account by introducing the self-energy Σ_L (Σ_R) in the effective Hamiltonian [96]. The total current in such a device is given by Eqn. 2.12. The transmission function, $T(E, V)$ is an important intrinsic factor describing the quantum mechanical transmission probabilities for electrons. It is worth noting that the transmission probability depends not only on the electron energy E but also upon the applied external bias V . More details of the theoretical scheme see Refs. [208, 49, 96].

In the current calculation, the positions of Au atoms in the electrodes are fixed at the bulk value of a face-centered cubic structure with a lattice constant of 4.08 Å. We have used a Monkhorst Pack grid of $4 \times 4 \times 20$ in the Au lead calculation, which sets the boundary condition at the interface between the scattering region and the electrodes. The S anchoring atom lies at the hole site of Au(100) surface with Au-S bond lengths close to an average value of 2.40 Å. Similar to our structure optimization, the PBE exchange-correlation functional form and norm-conserving pseudopotentials were used in Smeagol transport calculations. But in considering the computational cost, single-zeta basis sets with polarization orbitals were used for C, N, O, S and H; while a single-zeta basis set was used for Au with only 6s as the valence electron. Note that the Fermi level in the bulk Au is largely dominated by a broad Au 6s band. The 5d and 6p orbitals only start to play a role at energies 3 eV below or

3 eV above the E_F respectively. Since we are only interested in the low-bias (≤ 1.0 V) regime for transport calculations, the electrodes can be satisfactorily described by the 6s electron only. The resolution of the real-space mesh was again set to a 150 Ry cutoff, and the tolerance in maximum density matrix difference is 10^{-4} . The charge density is obtained by integrating the Green's function over 200 imaginary and 1000 real energy points according to the scheme described in Ref. [96].

6.3 Differentiation of DNA Bases - Static Calculations

6.3.1 Base paring and binding energies

Table 6.1: Binding energy E_b (in eV) for DNA base pairs used in transport calculations.

Probe/Target	A	C	G	T
A	0.38	0.43	0.95	0.88
C	0.43	0.50	1.48	0.76
G	0.95	1.48	0.48	0.88
T	0.88	0.76	0.88	0.65

The binding energies (E_b) of the probe-target base pairs formed temporarily in the nanopore are strongly correlated to the number of H-bonds formed in between with about ~ 0.4 eV per H-bond (see Table 6.1). The calculated values for E_b show that

the H-bonding can significantly stabilize the DNA molecule as it passes through the pore, thereby preventing drastic variations in the current due to thermal fluctuations of the structure and the uncertainty in the orientation of the base between the two electrodes. On the other hand, the H-bonding between probe- and target-base is weak enough to allow for an easy break-up when the ssDNA molecule is pulled through the nanopore by the driving field. The covalent bond of the probe-base's thiol group is, however, strong enough to keep the probe firmly placed on the surface of the gold electrode, without the risk that it would be swept along with the passing DNA molecule.

6.3.2 Tunneling currents and recognition map

Table 6.2: Vacuum size between the target and the right electrode (in Å) for different probe-target combinations.

A probe	A	2.53	C probe	A	2.50
	C	4.73		C	4.30
	G	3.17		G	3.10
	T	4.64		T	4.39
G probe	A	2.94	T probe	A	3.05
	C	4.53		C	4.34
	G	4.22		G	3.16
	T	4.56		T	4.63

The current-voltage curves calculated for the device involving the base C as a probe are shown in Fig. 6.3. The vacuum gap between target base and gold electrode (see Table 6.2) leads to relatively small current values at low biases. Recalling that the

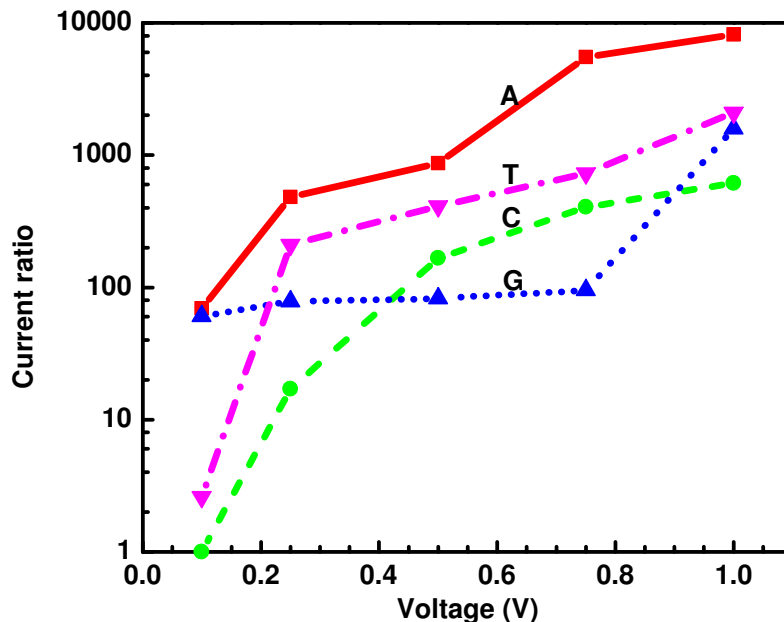


Figure 6.3: The current-voltage curves for the device functionalized with a C-probe for all four possible target bases (A: red square; C: green circle; G: blue triangle; T: pink upside-down triangle) with current signals plotted in logarithmic scale. The current signals are taken as ratios with respect to the value of having C as the target at a bias of 0.1 V.

figure of merit for distinguishing two different base molecules is that their associated currents differ by at least one order of magnitude, in Table 6.3 we present our recognition map. For instance at a bias of 100 mV, using either A, G, or T as a probe, we can distinguish the set A, C, and G from T (while A, C and G cannot be distinguished from each other). In contrast, when C is used as a probe, we can differentiate A and G from C and T. At an increased bias the recognition properties of the proposed device changes. For instance at 250 mV, the A probe provides different currents for

Table 6.3: Summary of the information deducible for different probes from current measurements (at 100 mV and 250 mV) or from a force signal (proportional to the binding energy). Target bases that cannot be distinguished are combined in parentheses.

Probe/Bias	100 mV	250 mV	E_b
A	(A, C, G) from T	A from (C, G) from T	(A, C) from (G, T)
C	(A, G) from (C, T)	A from G, G from T	(A, C) from G from T
G	(A, C, G) from T	(A, C, G) from T	(A, T) from C from G
T	(A, C, G) from T	C from (A, G) from T	(A, C, G, T)

A, T or C and G (C and G however remain indistinguishable from each other). At the same voltage the C probe can distinguish A from G, and C from T, the G probe can distinguish the set (A, G, C) from T, and finally the T probe can distinguish C from A or G, and from T. It therefore appears that T is the base most easy to identify, as also suggested in a previous study [65]. Our scheme, however, adds the ability of identifying A and G, which used to be the major obstacle of nanopore DNA sequencing. In our calculations, this is achievable by using A or C as probe at a bias of 250 mV.

Functionalization of the electrodes with C as a probe appears to yield the best way for a reliable identification of all four base molecules in DNA. This can be achieved by carrying out three sequencing runs at three different bias voltages, namely 100 mV, 250 mV, and 750 mV. The flow diagram shown in Fig. 6.4 gives the illustration of this proposed protocol of DNA sequencing.

The first set of measurements at 100 mV would result in a series of current signals

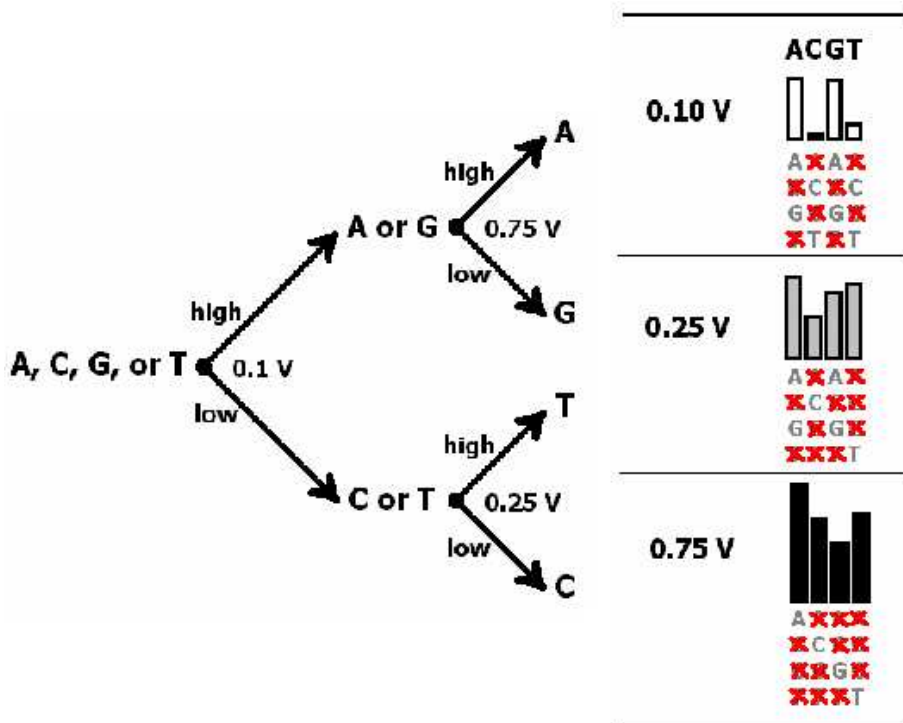


Figure 6.4: Flow diagram illustrating the decision-making process of a device involving C-probe leading to the identification of a target base in the sequence. Here, "high" and "low" refer to higher or lower current values at a given bias voltage. The height of the bars below the letters A, C, G, and T on the right side of the figure corresponds to the respective current signal (on a logarithmic scale). The crossed-out letters below the bars refer to possible target bases that have been ruled out.

that fall into two easily distinguishable categories: "high" current values if A or G is the target base, and "low" current values if C or T is the target base. The difference between the two categories is nearly two orders of magnitude, which should make the distinction extraordinarily robust. We now require additional information to resolve the remaining ambiguity of A/G and C/T. In a second measurement at 250 mV, it will be possible to distinguish between C and T, as their respective current values differ by one order of magnitude at that bias voltage. Thus, any "high" current value

would lead to the identification of a T in the sequence, while any "low" current value means that a C is at this position in the sequence. Finally, a third measurement at 750 mV causes the current values for the bases A and G to differ by two orders of magnitude, leading to an easy distinction between the two, where "high" current values correspond to A, while "low" current values correspond to G.

6.3.3 Detection Using Force Signal

It may even be possible in our proposed setup to combine the electrical signal from the embedded electrodes with a force signal [210] driving the ssDNA through the nanopore. Since the binding energy of the selected probe to the target through the H bond is sequence specific, a different force needs to be applied to ensure the DNA strand traverses at a constant speed through the nanopore. The applied force is linearly proportional to the binding energy of the probe-target pair. For a binding energy of 0.5 eV, the rupture of about 1 Å occurs with a force ~ 1 nN. Considering a typical thickness of 10 nm for a synthesized nanopore, the voltage required for such a force is about 2 V approximated by a uniform electric field across the nanopore. The external driving voltage is linearly scaled with the force, thereby the binding energy. The double/triple of the binding energy doubles/triples the voltage, which becomes detectable for pairs with different numbers of H bonds. This may provide supplemental information, in addition to the tunneling current, for distinguishing the

DNA bases. For instance, using C as the probe, the current results at 100 mV allow for a direct distinction between the sets (A, G) and (C, T), while the binding energies can tell the difference between A and G, and between C and T (Table 6.3). By combining the information of the driving force (threshold voltage) with the current results, it would suffice to have a single run with one probe at a given bias to distinguish all four nucleic acid bases.

6.4 Dynamic Stability of Currents - Molecular Dynamic Simulations

In this proof-of-concept study, we have shown that current responses may differ by at least one order of magnitude for different bases. Based on that we have proposed tentative recognition schemes to distinguish all the four bases. The potential feasibility of this approach has led us to the next-step study of the stability of probe-target pairing in the nanopore by *ab initio* molecular dynamic (MD) simulations and the investigation of the stability of tunneling currents employing state-of-the-art non-equilibrium Green's Function method.

6.4.1 Modeling and methods

In the last section, we considered each of the four natural DNA bases as the molecular probe of the functionalized electrode, which is anchored to the inner surface of one of the electrodes via a thiol group. As an ssDNA is pulled through the nanopore via a driving electric field, the probing molecule will form a base pair with the incoming base temporarily. We carried out static calculations using density functional theory (DFT) to find out the pairing geometry by energy minimization. In a real-world experiment, however, there are more environmental factors in play. For instance, the thermal fluctuation of structures under a non-zero temperature may affect the stability of base-pairing as well as the electrical response of the system.

In order to explore this effect, we have studied the variation of pairing geometries of the probe-target pairs by Born-Oppenheimer MD simulations. Nucleic acid bases terminated by methyl groups were used for these MD calculations based on the Kohn-Sham formulations of DFT implemented in SIESTA [129]. The size of the simulation box was chosen to be 20 Å to avoid unphysical interaction between adjacent periodic images. The tolerance in maximum density matrix difference was set to 10^{-4} . The Noé thermostat [211, 212] was used to thermalize the system at near room temperature with a MD time step of 1 fs and a Noé mass of 10 Ry·fs². The initial 3 ps data for each pair was discarded for the thermalisation (Note: We have done one test on C-T pair for 20000 steps, that is 20 ps. And it is shown that the system gets into

equilibrium after 3000 steps (3 ps).) We sampled the geometry for the following 1000 steps by every 100 steps. Each snapshot of geometry was used for electron transport calculation. The stability of tunneling currents is reflected from these results. It may not be a sufficient sampling from the statistical point of view, but it is expected to provide basic clues on achieving stable enough current in a dynamic electrical measurement. The bias-dependent tunneling current is then calculated from the NEGF method based on the Keldysh formalism, as implemented in SMEAGOL [208, 49, 96].

6.4.2 Stability of pairing geometry

The base-pairing geometry obtained by energy minimization may be driven out of its equilibrium configuration under thermal activation. Our MD simulations of DNA base heteropairing and homopairing geometries have revealed that two or more intermolecular hydrogen bonds are indispensable to avoid significant bending of the aromatic ring of one base with respect to that of the other. This agrees fairly well with other stability studies [213], where all stable dimers were constructed with at least two hydrogen bonds in between. The reason is that, the base stacking geometry becomes competitive under one hydrogen bond [214], and it tends to greatly disturb the planar base pairing structure. This is a disaster for the tunneling current signal. If we assume the orientation of the probe molecule remains the same, then the bending the target molecule with respect to the probe will significantly increase the

vacuum between the target molecule and the right electrode, which in turn, reduces the current drastically [215, 65, 216]. In other words, the probe is not good enough to stabilize the coming-in target, which is certainly out of the question of our proposed scheme.

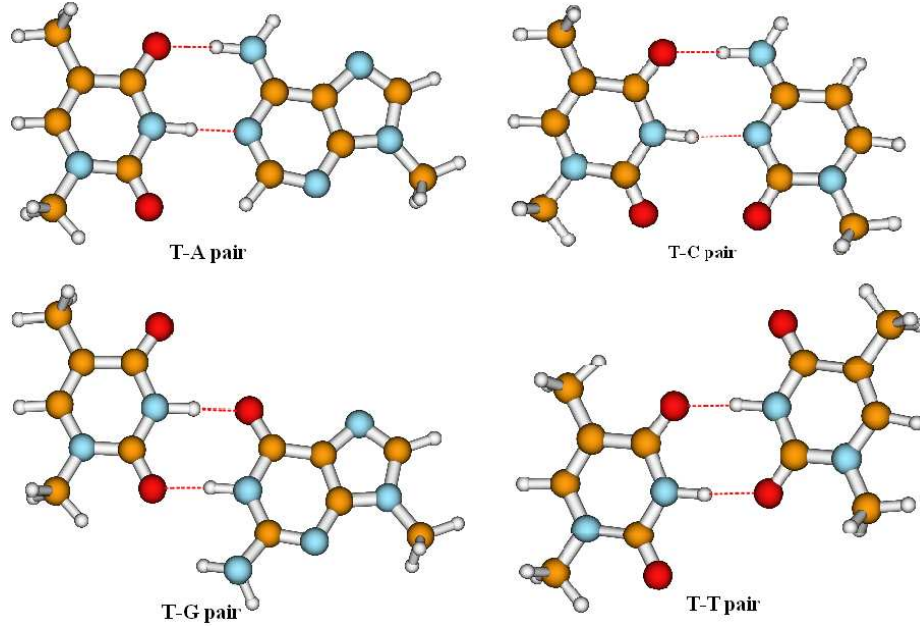


Figure 6.5: T-X (X=A, C, G and T) pairing geometries by energy minimization.

Table 6.4: Binding energy E_b and geometrical characteristics for T-X (X=A, C, G, T) DNA base pairs optimized using energy minimization.

X	E_b (eV)	H-bond 1 (O \cdots H-N) distance (\AA)	H-bond 1 (O \cdots H-N) angle ($^\circ$)	H-bond 2 (N-H \cdots N/O) distance (\AA)	H-bond 2 (N-H \cdots N/O) angle ($^\circ$)
A	0.88	2.765	176.583	2.765	178.364
C	0.76	2.728	178.071	2.903	172.028
G	0.88	2.713	175.537	2.686	178.429
T	0.65	2.744	175.264	2.787	174.419

Under the consideration of having at least two hydrogen bonds between the probe and target molecule, T (Thymine) seems to be a good fit for the purpose of stabilizing the structure within the nanopore. The static pairing geometries of T with all the four bases A, C, G, and T are demonstrated in Fig. 6.5 and tabulated in Table 6.4. Two strong hydrogen bonds are formed between all the probe-target pairs, which are usually holding the form of $\text{N-H}\cdots\text{O}$ or $\text{N-H}\cdots\text{N}$. It is generally accepted that the shorter the distance and the more linear the angle of a hydrogen bond, the stronger the bond is [217]. Thereby, the more stable the base-pairing geometry would be. The Watson-Crick complementary pair T-A and the Wobble base pair T-G have the highest stabilization energy of 0.88 eV. Despite the same binding energy, however, they are different in accommodating the secondary interactions associated with other atoms of the molecules which are not involved in the direct hydrogen bonding. The T probe has three H binding site which are exposed to form possible H-bonds with the target molecule: O, N-H and O in turn. In the T-A pair, the O at the 3rd place of T forms a weak H-bond with the hydrogen donor of A (O-H distance is about 2.789 Å), which further strengthens the planar conformation of T-A pair. Their pairing structure remains quite stable in a MD simulation. Nonetheless, the mismatch of the Wobble T-G pair at the H binding site gives more freedom for one base to rotate with respect to the other. This is the same with the T-T pair. Although the T-C pair is also at the right match position, the electrostatic repelling of O-O at the 3rd place again reduces its thermal stability.

6.4.3 Stability of tunneling current

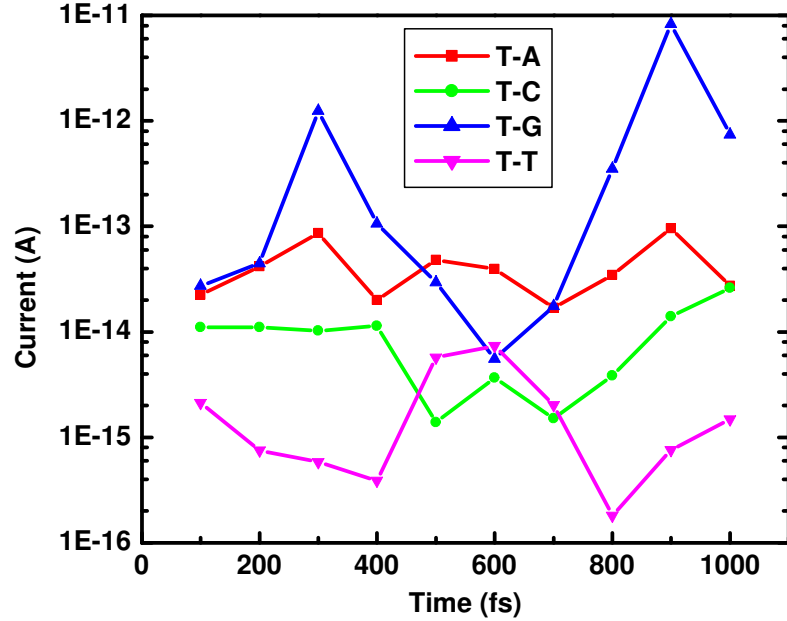


Figure 6.6: Current variation as a function of MD simulation time for T-X (X=A, C, G, T) pairing systems at a bias of 250 mV.

The tunneling currents of the snapshot pairing geometries sampled from MD simulations at a bias of 250 mV are plotted in Fig. 6.6. The current is most stable for the T-A pair, where the variation of current is less than 6 times. The current stability is followed by the T-C pair, where the variation is about 20 times within the time scale considered here. The situation apparently gets worse for the case of the T-T pair with nearly two orders of magnitude variation. The T-G pairing is the worst of all despite of its known thermodynamic stability. It brings us to the next section

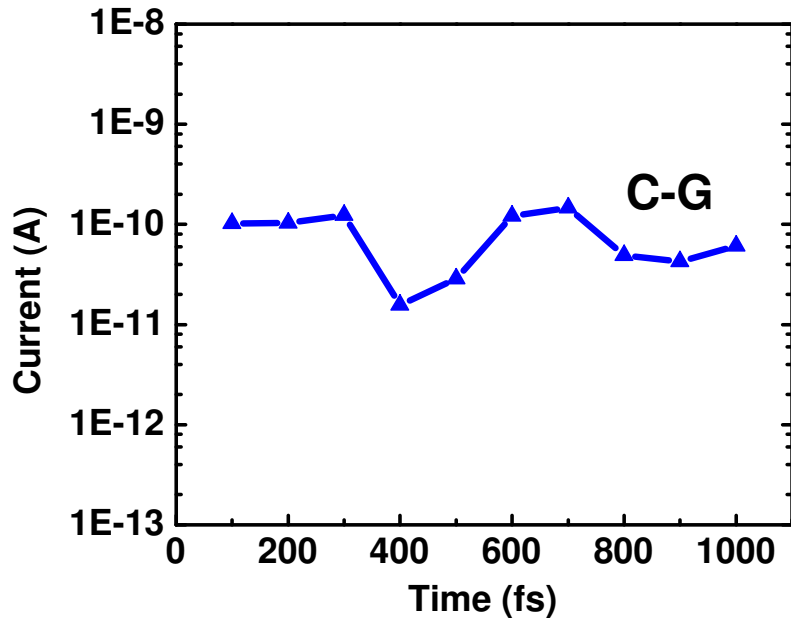


Figure 6.7: Tunneling currents of the C-G pairing system as a function of the MD simulation time at a bias of 250 mV.

of this study to investigate the possible factors that have significant effect on the tunneling currents besides the geometrical parameters. But before that, it may be a reasonable deduction that the Watson-Crick C-G pair may be as good as the T-A pair in stabilizing the tunneling current. Its current plot is shown in Fig. 6.7. The current variation is within one order of magnitude. In terms of stability, it is still good. But it is also a bit surprising to see a larger variation in current compared to the case of T-A pairing. We will uncover all these mysteries in the following section.

6.4.4 Influencing factors for tunneling current

To illuminate the major influencing factors for tunneling current, we will now focus on two cases: the Watson-Crick pairing T-A and C-G, where T/C works as the probe and A/G as the target. The distribution of transmission peaks (see Fig. 6.8 for a bias of 250 mV) is distinguishably different especially in the region near the Fermi level for the two cases.

6.4.4.1 Vacuum size

In case of T-A pair (Fig. 6.8(a)), the prominent transmission peaks are far away from the Fermi level, and makes no significant contribution to the current at a bias of 250 mV as considered here. Therefore the shift in the peak position does not have any observable effect on the tunneling current. Rather, the current, which is an integration of transmission function within the bias window, is basically determined by the baseline of the transmission function, which is a function of the vacuum size between the right side of the target molecule and the right electrode. For example, the vacuum size for the three selected snapshots No. 100, No. 300 and No. 500, are 2.42, 2.09 and 2.20 Å, respectively. It is clearly shown that the level of the transmission baseline increases as the vacuum size decreases in the order of snap100, snap500 and snap300. Besides the small variation, however, the level of the transmission baselines remains in the same order, so does the value of the tunneling currents (Fig. 6.6).

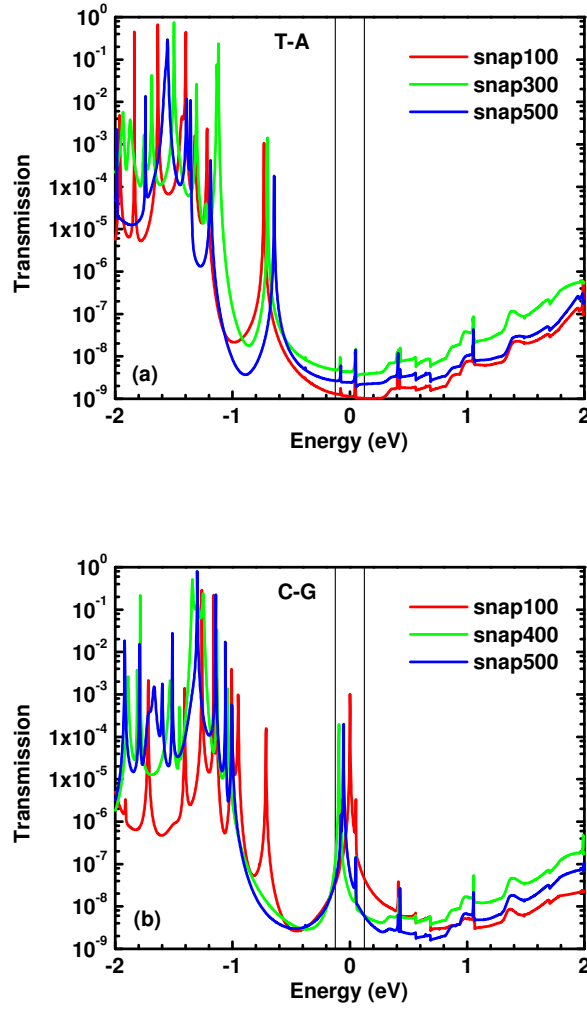


Figure 6.8: Transmission functions for (a) the T-A and (b) the C-G pairing system sampled from the MD simulations at a bias of 250 mV. The bias window is indicated by vertical black lines. The Fermi level is aligned to zero.

6.4.4.2 Hydrogen bonds

The transmission results of the C-G pair (Fig. 6.8(b)), however, point us to another factor. In this case, the transmission peak (labeled as PG hereafter) in the close affin-

ity of the Fermi level ($-125 \text{ meV} < E - E_F < 125 \text{ meV}$) has determinative significance to the tunneling current at a bias of 250 mV. This peak corresponds to a molecular orbital right below E_F arising mainly from the G (Guanine) part of this base pair, because of its low ionization potential. The location of this peak, however, is found to be related to the strength of the H-bonds connecting the target G to the probe C in contact with the left electrode.

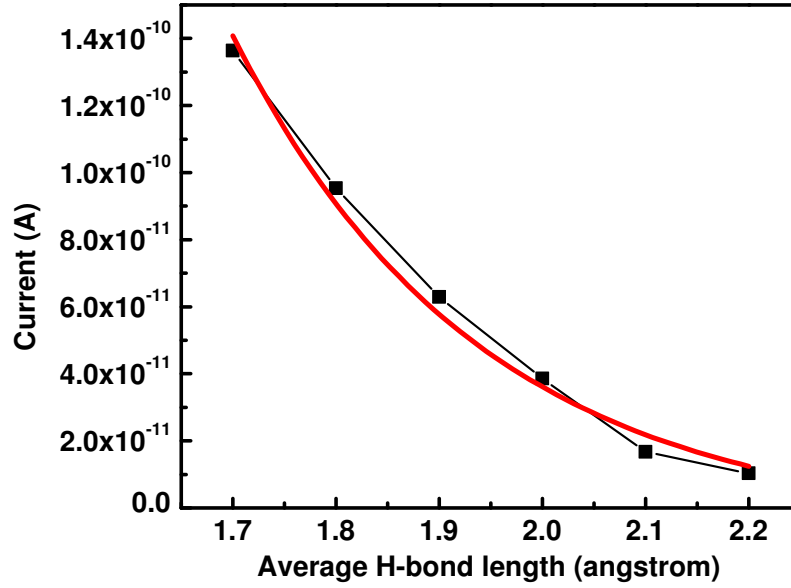


Figure 6.9: Current variation as a function of the average H-bond length at a bias of 250 mV. It is fitted by an exponential decay in red.

In order to clarify the effect of H-bonding on the tunneling current, we have done calculations on a simple thought experiment. One starts with the relaxed C-G pairing structure obtained from static optimization. Then one fixes the vacuum size on the

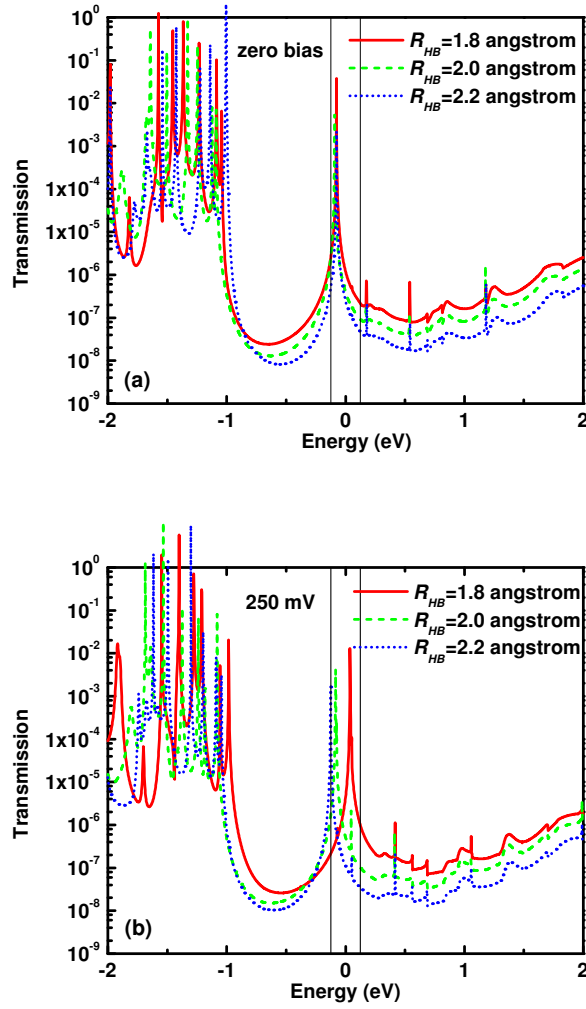


Figure 6.10: Transmission functions for the C-G pairing system with the average H-bond length varying from 1.8 to 2.2 at (a) zero bias and (b) a bias of 250 mV. The Fermi level is aligned to zero. A bias window of $-125 \text{ meV} < E - E_F < 125 \text{ meV}$ is indicated by vertical black lines on both graphs for easy of tracking the shift in peak positions near E_F .

right, and increases the H-bond distance by a step of 0.1 \AA . The current is calculated for each pairing geometry after being embedded in the nanopore. The current values at a bias of 250 mV are plotted in Fig. 6.9. The current follows an exponential

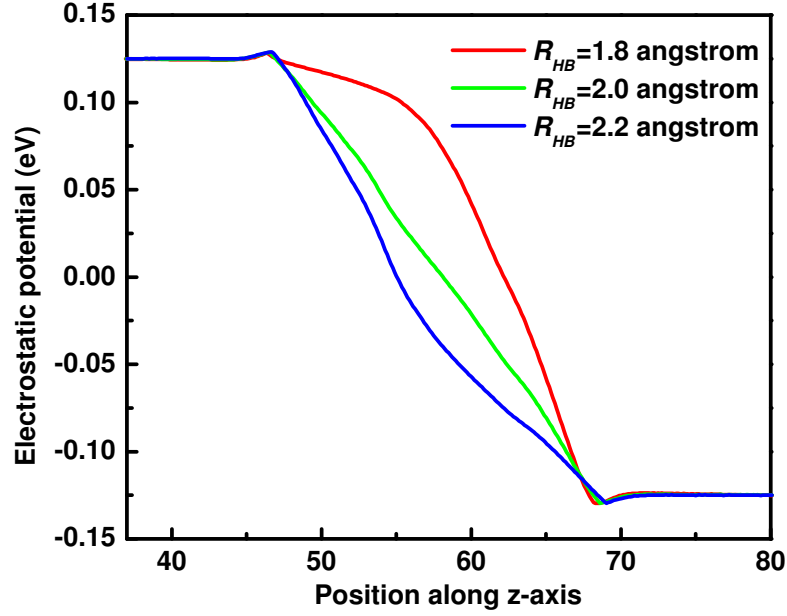


Figure 6.11: Electrostatic potential profile varies as a function of the strength of hydrogen bonding (reflected from the bonding length R_{HB} as labeled in the figure) between the C-G pairing.

decay when the average H-bond length increases, as also found in STM experiments using G-tip as the probe and C/T as the target [218]. The fitted (red curve in Fig. 6.9) decay constant is about 4.19 \AA^{-1} showing a very sensitive decrement in current when the H-bond is enlarged. The reason for this is easily seen from the corresponding transmission functions shown in Fig. 6.10. At zero bias, the positions of the transmission peak PG for all the three cases are located at about the same energy -0.09 eV. Under a positive bias of 250 mV (the left electrode has a lower potential, but a higher potential energy), however, the PG peak shifts by 0.12, 0.01 and -0.03

eV for $R_{HB}=1.8, 2.0, 2.2$ Å, respectively. The H-bond strength, which is closely reflected from the R_{HB} (the larger the length, the weaker the bonding), determines electrostatic potential profile of the system, thereby the shift of the PG transmission peak under bias. Fig. 6.11 is a demonstration of the electrostatic potential profile affected by the strength of hydrogen bonding. In the case of $R_{HB} = 1.8$ Å, the target G is strongly bounded to the probe C, and the transmission peak PG closely follows the shift of the potential energy of the left electrode. In the case of $R_{HB} = 2.0$ Å, the target G is more like an isolated island. The potential drops almost linearly between two electrodes, and the transmission peak PG hardly shifts. As R_{HB} increases to 2.2 Å, the transmission peak PG starts to shift to the lower energy following the potential energy change of the right electrode.

Table 6.5: Individual H-bond lengths, the average H-bond length as well as the vacuum size along the transport direction (z-axis) between G and the right electrode for the C-G pairing system sampled from the MD simulation.

	Vacuum R_{vac}	H-bond length R_{HB} (Å)				R_{HB}/R_{vac}
		O...H(-N)	N...H(-N)	(N-)H...O	average	
Snap100	2.37	1.840	1.808	1.876	1.841	0.777
Snap400	2.01	1.961	1.815	1.531	1.769	0.880
snap500	2.37	2.265	1.746	1.586	1.865	0.787

Back to the C-G pairing system sampled from the MD simulation, we have listed individual H-bond lengths, average H-bond length as well as the vacuum size along the transport direction (z-axis) between G and the right electrode in Table 6.5. We define a factor R_{HB}/R_{vac} to reflect the relative strength of the hydrogen bonding

between the probe and the target. This is to generalize the result that we have got in that extremely ideal case as discussed above. The smaller this value is, the stronger the binding. The relative strength of H-bonding determines the electrostatic potential profile of the system, thereby the shift of the transmission peak PG under bias. In the case of C-G study, snap100 has the lowest R_{HB}/R_{vac} ratio, thus the highest H-bond strength. The transmission peak PG shifts the same as the left electrode when an external bias is applied. In other words, it shifts to a higher energy when a positive bias is applied. This peak shifts from the position of -0.10, -0.14, -0.12 eV at zero bias to 0.00, -0.09, -0.05 eV at a bias of 250 mV (Fig. 6.8(b)) for snap100, snap400 and snap500, respectively. The amount of shifting follows the relative strength of the H-bonding of the base pair (the reverse order of the R_{HB}/R_{vac} ratio), i.e. snap100 > snap500 > snap400. The difference in the peak shifting brings the difference in its contribution to the tunneling current. As it is revealed earlier in our discussion, the current at a bias of 250 mV follows an exponential decay when the average H-bond length increases. However, since the aromatic rings do not bend significantly with respect to each other in the case of C-G pairing, the H-bonding and the vacuum size effect counteract each other resulting relatively stable currents in spite of the change in hydrogen bonding strength.

An observable shift of this near- E_F transmission peak appears for all the probes interacting with target G. Usually the change in the relative strength of the H-bonds induces different shifting of this peak under bias, thereby affecting the tunneling

current. This also explains the large variation in current for the T-G pair in Fig. 6.6.

6.4.5 Base recognition scheme

The Watson-Crick base pairing intends to form and provide the most stable current for electrical detecting. This is already observed in STM experiments [219], where a nucleic-acid-base tip can constantly pinpoint its complementary base among the non-complementary bases deposited on a metal surface. We propose using four pair of electrodes each having one electrode functionalized with one of the four natural nucleic acid bases A, C, G or T to detect their complementary bases as an ssDNA passes by in a nanopore. These four pairs of electrodes send out electrical signals to four channels. The sequence of bases can be discriminated by correlating the response versus time from the four outputs. For instance, an electrical signal indicating a stable current from a channel of probe A tells that a base T is passing by, the electrical signal from a channel of probe C means its partner is G, and so on. This might be accomplished by combining the nanopore technique with the "multiplexed electrical detection" technique [220], forming addressable electrical contacts with different probes printed on the electrodes. Another direction is to design a probe combining the features of bases. In that case, we might just need one probe and one channel, but requirement is that the $I - V$ characteristics for each base are distinguishable.

6.5 Summary

It is a revolutionary idea to apply nanopore techniques to the rapid DNA sequencing at a low cost. While it has been shown that an ssDNA can indeed rapidly pass through a nanopore when a driving electric field is applied, it is still somewhat uncertain whether the transverse electrical signal would be stable enough to reliably distinguish the nucleic acid bases of DNA. In this study, we have shown that the functionalization of nanopore-embedded gold electrodes with specific nucleic-acid-base probes can stabilize their complementary bases in a pore-translocating DNA sequence via hydrogen bonds against thermal fluctuations and thus lead to a dramatic improvement in the stability of transverse tunneling current in base detection, which had been a serious problem in previous setups lacking functionalization of the electrodes. This preliminary study has revealed that one needs to have at least two H-bonds between probe and target at the right matching position to achieve stable current. Our theoretical study has further revealed that the molecular orbital alignment (electronic signature, H-bonding distance) as well as the vacuum distance (size and orientation of the base) determines the tunneling current of the system.

From our results, it does now actually appear feasible to use the nanopore setup to successfully identify individual nucleotides. However, we do not want to close the question with conclusive answers. There are certainly a lot more real factors to consider about, such as the translocation dynamics of DNA, the effect of counter

ions and solutions, and the interactions between molecules and the nanopore walls.

Theoretical methods provide us a valuable tool in further evaluating these possibilities before an experiment can really take off.

Chapter 7

Grand Summary and Future Perspectives

7.1 Grand Summary

It may not seem to be an easy task to replace the role of semiconductors with molecules in electronics. But every revolutionary advance in science and technology starts with imagination. The potential use of molecules brings attractive features that are incomparable from the conventional Si-based electronics. Since the first proposal of a unimolecular diode by Aviram and Ratner[2], many prototypes have been fabricated using single molecules in electronic devices. Today we are standing at the beginning of understanding and building of electronic functional units at the molecular and

atomic levels. While the current experimental techniques have not reached the level of a single molecule measurement without some external perturbations which limit their applicability in understanding the underlying physics, it is possible to develop the fundamental physics from reliable first-principles calculations. This work is one of the efforts along this line. We have explored the possibility of having molecules working in a wide spectrum of electronic devices, ranging from molecular wires, spin valves/switches, diodes, transistors and sensors. The fundamental roles of molecules and molecule-electrode interfaces have been investigated from the electronic structure perspective. Following is a list of the central messages that we have gained from this thesis work, which deepens the understanding in this field and also provides guidance for experimental efforts.

1. We have observed the magnetoresistive effect in a spin-valve structure where the non-magnetic spacer sandwiched between two magnetic conducting materials is replaced by a self-assembled monolayer of organic molecules or a single molecule (like a carbon fullerene). That is, a significantly higher tunneling current is obtained for a configuration in which the net spins of two magnetic electrodes are aligned in parallel than for a configuration aligned in anti-parallel. In addition, the anti-parallel spin configuration (OFF state) has a lower energy than the parallel spin configuration (ON state), which eliminates the need for applying a local magnetic field to obtain an OFF state.

2. The spin-valve effect as well as the magnitude of the tunneling current is strongly

influenced by the nature of the chemical bonding in the molecular structure. π -conjugated molecules are more conductive than σ -bonded molecules. Besides, the delocalized electrons in π -bonds have higher magnetization susceptibility than the localized electrons in σ -bonds. Thus a higher difference in the parallel and anti-parallel currents is observed for the former.

3. The interface between the metallic electrode and the molecule in strongly-coupled systems need to be indispensably considered for molecular-scale electronic devices. The atomic configuration and the formation of chemical bonds at the interface strongly affect the spin-valve effect as well as the magnitude of tunneling current. The hybrid states of metal and molecule are usually responsible for a high tunneling current in the low bias regime. The generation and features of such states depend on both the detailed interfacial binding and the electrode spin configuration.

4. We have observed the diode behavior in donor(D)-bridge(B)-acceptor(A) type of single molecules. It is unambiguously revealed that the intrinsic dipole moment induced by substituent side groups in the molecule leads to enhanced/reduced polarization of the system under a forward/reverse applied potential, thus asymmetry in the charge distribution and the electronic current under bias. Under a forward bias, the energy gap between the D and A frontier orbitals closes and the current increases rapidly; whereas under a reverse bias, the D-A gap widens and the current remains small.

5. We have designed a unimolecular transistor based on the diode-rule and tested the transistor behavior. The enhancement/depletion mode of a transistor can be realized by applying a gate field along the positive/negative direction. The asymmetric molecular structure along the gate direction leads to a sensitive coupling to electric field produced by the gate potential. The evolution of wavefunctions in the presence of the gate-coupling molecular part as well as the shift in molecular orbital energies results in the enhancement of source-drain current under a positive gate.

6. We have proposed and primarily tested the idea of using functionalized electrodes for rapid nanopore DNA sequencing. The idea can essentially be extended to other chemical and biological sensing. It is shown that the functionalization of nanopore-embedded gold electrodes with specific nucleic-acid-base probes can stabilize their complementary bases in a pore-translocating DNA sequence via hydrogen bonds against thermal fluctuations and thus lead to a dramatic improvement in the stability of transverse tunneling current in nucleotide detection. The vacuum size and the hydrogen bonding are found to play central roles in determining the magnitude of the tunneling current.

This thesis work strives to provide a general view of the modeling and understanding of molecular electronic devices in this burgeoning new field. Three different transport theories were employed for different circumstances, each with their own limitations and strengths. One should always be aware of the approximations and assumptions for each theory when tackling a real-world problem. A quantitative way of estima-

tion of the possible error bars from these theoretical methodologies, however, is not established yet. The most prominent effect may come from the quantum mechanical electronic structure calculations. For instance, the applicability of mean-field theory, the choice of exchange-correlation functional form in density functional theory, the type and size of basis sets and the numerical implementation of a computational code. The choice of these parameters has always been a balance between the accuracy and the computational cost. Our main goal, especially in this study, is to gain a qualitative picture of the questions of interest. For each of the topics (Chapter 3-6), we have done a comparative study on the same footing. The absolute values of current may vary, for instance, with increasing the size of basis set, but one would expect that the overall relative picture be the same due to the fortuitous cancellation in the systematic error.

7.2 Future Perspectives

In conventional semiconductor electronics, doping is the indispensable way of tailoring the electronic property of materials, thus the functionality of the devices. Its "accuracy" breaks down when the size of the device is so small that the statistical physics can never hold. Molecular electronics, however, brings up a totally different perspective - using of organic molecules as ingredients of functional electronic devices. The large variety of molecules that one can design and synthesize are only limited

by our imagination. The molecules are usually featured by uniform structure and functions under a certain synthesis route, and are highly controllable. Besides, their functions can be largely flexible and tailorable by modification of either the bonding feature of the backbone (like π -type or σ -type) or the side groups, like the donor or acceptor groups. The specific interaction among molecules is another bonus, which allows selective detection of chemical and biological molecules in the environment by design of the probe molecules attached to the electrodes. The molecular design and engineering would be a very promising area of research in the future. And theoretical simulation would continue to serve as a powerful tool in revealing the underlying physics and providing guidance in this area. In the following, I will primarily talk about the current limitations, the future prospects and the challenges that we are facing from the theoretical model and methodology perspective.

In this thesis work, we have been focusing on a low-bias low-temperature short-length transport regime, which is featured by elastic coherent electron transport. This assumption may, however, be violated by the real world sophistication.

1. Inelastic electron transport - electron-phonon coupling

At a low temperature, the atoms of a molecule are "frozen" in their positions, and this frozen atomic potential is used to calculate the energy levels of electrons from the density functional theory in our case. As the temperature is raised, the vibrations of atoms increase in amplitude and exchange energy with electrons through the electron-

phonon interaction [105]. The phonon-assisted tunneling is usually characterized by a sharp peak in the d^2I/dV^2 curve. This effect is important in prediction of heat dissipation under practical application conditions. It has also been developed into a useful tool for molecule identification, like the inelastic electron tunneling spectroscopy (IETS) [221, 108, 107].

The NEGF transport methodology used in this work can be extended to incorporate the electron-phonon coupling in a systematic way. The scattering term due to the electron-phonon interaction can be introduced by means of appropriate self-energy terms.

2. Strong correlation effect - electron-electron interaction

Like any other cases of strong correlated electron systems, the mean field theory used to calculate the electronic structure fails in describing the electron-electron dynamic correlation. Thereby the calculated transport properties cannot reproduce the observed Coulomb blockade, Kondo effect, etc. In the study of these fascinating frontier physical phenomena, we have to go beyond the single-particle mean field theory. Again the NEGF methodology is highly adaptive to many-body perturbation theory. It is possible to evaluate the self-energy and scattering functions to higher orders using many-body theory such as the GW method [109]. An appropriate formulation involving Fock space (essentially a full configuration interaction methodology) has been developed by Datta and co-workers [222].

For sufficiently strong interactions, however, even the perturbation theory breaks down. Besides, one needs higher order Green's functions in the NEGF formalism to describe the electrical response of such super-strongly correlated systems [82]. Increasing interest is shown from the theoretical community.

3. Local heating and current-induced force - time-dependent approach

In the ideal cases considered in our work, electrons experience elastic transport, the Joule heating I^2R associated with a resistor R could be dissipated in the contacts rather than in the conductor itself. The reason is that resistance comes from the loss of momentum associated with scattering while the associated Joule heating comes from the loss of energy. That is why we can reach a very high apparent current density without burning up the molecule. As a matter of fact, this is observed in experiments. But the existence of dynamic phase-breaking factors in the conductor, like phonon-electron scattering, induces heat dissipation in the conductor. The local heating and current-induced force are topics of high interest these days [223]. A promising way of studying these effects is to use the time-dependent density functional theory (TDDFT) [224], which powers the DFT formalism to dealing with excited states. It not only helps to provide more accurate energy levels for the virtual orbitals, overcoming the notorious band gap underestimate problem of using DFT, but also generates time-dependent wavefunctions. The true many-body total current in a closed system is given exactly by the one-electron total current, obtained from TDDFT [225]. Similar to the DFT approach, the Kohn-Sham time-dependent one-

electron orbitals can be used to compute the time-dependent transport properties of the system. Frequency-dependent currents and the evolution of current flow with time can explicitly be mapped out [226]. Under the linear response assumption, TDDFT can be implemented with the NEGF method in place of DFT.

4. Three terminal device - simulation of transistors

In this thesis work, we have been focused on two-terminal devices (Note that in the calculation of source-drain current for a transistor in Chapter 5, we have mimicked the gate potential using an applied electric field). The need for more rigorous simulation of three-terminal devices, like transistors and transistor-based sensors, requires an extension of the current transport scheme to a three or more-terminal case. In fact, Büttiker extended the two-terminal linear response approach to describe multi-terminal measurements long time ago [85, 86]. The current at each terminal is a summation of currents coming in from all the other terminals, with each component following the same two-terminal linear response formula associated with the transmission and potential drop between the pair of electrodes. One can have the Poisson equation including all the external fields (including the gate field) as the electrostatic boundary conditions [143] and still solve the Schrödinger equation self-consistently. The NEGF method would be appropriately modified to adjust the changes for the treatment of any gate potentials (three or more terminal devices).

Looking ahead, we have a bright future of molecular electronics. A vision from Ba-

sic Energy Sciences Advisory Committee (BESAC) states "if the time comes when integrated circuits can be fabricated at the molecular or nanoscale level, the limits of Moore's Law will be far surpassed. A supercomputer based on nanochips would comfortably fit in the palm of your hand and use less electricity than a cottage. All the information stored in the Library of Congress could be contained in a memory the size of a sugar cube. Ultimately, if computations can be carried out at the atomic or sub-nanoscale levels, today's most powerful microtechnology will seem as antiquated and slow as an abacus." [227]. Not only so, it also tells the grand challenges "The difficulties involved in this change of our understanding are huge, but the rewards for success should be extraordinary."

Appendix A

Accuracy and Computational Cost: A Case Study in Smeagol

All the calculations presented in this thesis were carried out on our group machine RAMA (a Beowulf Linux Cluster). Each slave node has Dual Intel Xeon 2.8G processor and 2GB RAM.

An example of the accuracy and computational cost comparison using SMEAGOL code is given below.

Table A.1: A convergence test of the calculated current with respect to the k -point sampling (Monkhorst-Pack kgrid) on a system of Au₆₄-Cytosine-Guanine...Au₆₄ using the parallel SMEAGOL code. The current is calculated at a single voltage of 0.25 V using 8 processors in parallel. The total number of atoms, electrons and orbitals are 178, 301, and 488, respectively. The mesh cutoff is set to 150 Ryd.

MP-kgrid	Number of kpoints	Current (A)	CPU time (min)
1×1×1	1	4.0972×10^{-12}	105.6
2×2×2	4	0.1289×10^{-12}	143.8
4×4×4	12	0.1436×10^{-12}	480.0
6×6×6	24	0.1393×10^{-12}	600.0
8×8×8	40	0.1376×10^{-12}	640.8

Appendix B

List of Related Publications

† Current Stabilization in Nanopore Detection of DNA Sequence

Haiying He, Ravindra Pandey, and Shashi P. Karna

in preparation.

† Asymmetric Currents in a Donor (D)-Bridge (B)-Acceptor (A) Single Molecule

- Revisit of the Aviram-Ratner Diode

Haiying He, Ravindra Pandey, Govind Mallick and Shashi P. Karna

J. Physical Chemistry C, **113**, 1575 (2009).

† Electronic Conduction in a Model Three-terminal Molecular Transistor

Haiying He, Ravindra Pandey, and Shashi P. Karna

Nanotechnology **19**, 505203 (2008).

† Functionalized Nanopore-Embedded Electrodes for Rapid DNA Sequencing

Haiying He, Ralph H. Scheicher, Ravindra Pandey, Alexandre Reily Rocha,
Stefano Sanvito, Anton Grigoriev, Rajeev Ahuja and Shashi P. Karna
J. Physical Chemistry C **112**, 3456 (2008).

† Mechanism of Electrical Rectification in a Unimolecular Donor-Bridge (π)-
Acceptor Diode

Haiying He, Govind Mallick, Ravindra Pandey and Shashi P. Karna
Proceedings of 2007 7th IEEE Conference on Nanotechnology, Aug. 2-5, 2007,
Hong Kong.

† Electronic Structure Mechanism of Spin-Polarized Electron Transport in a Ni-
C₆₀-Ni System

Haiying He, Ravindra Pandey and Shashi P. Karna
Chemical Physics Letters **439**, 110 (2007).

† Theoretical Study of Molecule Mediated Spin-Polarized Electron Tunneling be-
tween Magnetic Materials

Haiying He, Ravindra Pandey and Shashi P. Karna
Chemical Physics Letters **428**, 411 (2006).

† Spin-Polarized Electron Transport via a C₆₀ Molecule

Haiying He, Ravindra Pandey and Shashi P. Karna
Proceedings of 2006 6th IEEE Conference on Nanotechnology **2**, 830 (2006).

† Theoretical Study of Spin-Polarized Electron Transport from a Self-Assembled

Organic Monolayer on a Ni (111) Substrate: Organic Spin Switch

Haiying He, Ravindra Pandey, Ranjit Pati and Shashi P. Karna

Physical Review B **73**, 195311 (2006).

† Spin-dependent Electron transport along a Molecular Wire in a Metal (Probe)
- Vacuum - Molecule - Metal System: the Effects of the Size and the Shape of
the Probe Tip

Haiying He, Ranjit Pati, Ravindra Pandey and Shashi P. Karna

Proceedings of 2005 5th IEEE Conference on Nanotechnology **2**, 815 (2005).

References

- [1] Mann, B.; Kuhn, H. *J. Appl. Phys.* **1971**, *42*, 4398–4405.
- [2] Aviram, A.; Ratner, M. *Chem. Phys. Lett.* **1974**, *29*, 277–283.
- [3] Hammett, L. P. *J. Am. Chem. Soc.* **1937**, *59*, 96–103.
- [4] Hine, J. *Physical Organic Chemistry*; McGraw-Hill: New York, 1962.
- [5] Weiss, J. *J. Chem. Soc.* **1942**, *245*, 18.
- [6] Mulliken, R. S.; Person, W. B. *Molecular Complexes*; Benjamin: New York, 1969.
- [7] Iwai, H. *IEEE J. Solid State Circuits* **1999**, *34*, 357–366.
- [8] Mulliken, R. S. *J. Phys. Chem.* **1952**, *56*, 801.
- [9] Mulliken, R. S. *J. Am. Chem. Soc.* **1952**, *74*, 811.
- [10] Szent-Györgyi, A. *Sci.* **1968**, *161*, 988–990.
- [11] Pati, R.; Karna, S. P. *J. Chem. Phys.* **2001**, *115*, 1703.

- [12] Metzger, R. M.; Day, P.; Papavassiliou, G. C. *Lower-Dimensional Systems and Molecular Electronics*; Plenum Press: New York, 1991.
- [13] Carter, F. L. *Physica D* **1984**, *10*, 175–194.
- [14] Carter, F. L. *Molecular Electronic Devices*; Dekker: New York, 1982.
- [15] Carter, F. L. *Molecular Electronic Devices II*; Dekker: New York, 1987.
- [16] Carter, F. L.; Siatkowski, R. E.; Wohltjen, H. *Molecular Electronic Devices, Proc. 3rd Intl. Symp.*; Elsevier: North-Holland, 1988.
- [17] Petty, M. C.; Bryce, M. R.; Bloor, D. *Introduction to Molecular Electronics*; Oxford University Press: New York, 1995.
- [18] Binnig, G.; Rohrer, H.; Gerber, C.; Wihel, E. *Phys. Rev. Lett.* **1983**, *50*, 120–123.
- [19] Schneiker, C. W. "Nanotechnology workstation based on scanning tunneling/optical microscopy: applications to molecular scale devices" in *Proc. of the 3rd International Workshop on molecular electronic devices*.
- [20] Hameroff, S.; Schneiker, C.; Voelker, M.; He, J.; Dereniak, E.; McCuskey, R. *Proc. of IEEE Engineering in Medicine and Biology Society 10th Annual International Conference* **1988**, *1*, 1009–1011.
- [21] Pomerantz, M.; Aviram, A.; McCorkle, R. A.; Li, L.; Schrott, A. G. *Science* **1992**, *255*, 1115–1118.

- [22] Dorogi, M.; Gomez, J.; Osifchin, R.; Andres, R. P.; Reifengerger, R. *Phys. Rev. B* **1995**, *52*, 9071–9077.
- [23] Bumm, L. A.; Arnold, J. J.; Cygan, M. T.; Dunbar, T. D.; Burgin, T. P.; II, L. J.; Allara, D. L.; Tour, J. M.; Weiss, P. S. *Science* **1996**, *271*, 1705.
- [24] Martin, A. S.; Sambles, J. R.; Ashwell, G. J. *Phys. Rev. Lett.* **1993**, *70*, 218–221.
- [25] Geddes, N. J.; Sambles, J. R.; Couch, N. R.; Parker, W. G.; Jarvis, D. J. *Thin Solid Films* **1989**, *179*, 143–153.
- [26] Metzger, R. M.; Chen, B.; Böpfner, U.; Lakshmikantham, M. V.; Vuillaume, D.; Kawai, . T.; Wu, X.; Tachibana, H.; Hughes, T. V.; Sakurai, H.; Baldwin, J. W.; Hosch, C.; Cava, . M. P.; Brehmer, L.; Ashwell, G. J. *J. Am. Chem. Soc.* **1997**, *119*, 10455–10466.
- [27] Reed, M. A.; Zhou, C.; Muller, C. J.; Burgin, T. P.; Tour, J. M. *Science* **1997**, *278*, 252–254.
- [28] Frank, S.; Poncharal, P.; Wang, Z. L.; de Heer, W. A. *Science* **1998**, *280*, 1744–1746.
- [29] Tian, W.; Datta, S. *Phys. Rev. B* **1994**, *49*, 5097–5100.
- [30] Chico, L.; Benedict, L. X.; Louie, S. G.; Cohen, M. L. *Phys. Rev. B* **1996**, *54*, 2600–2606.
- [31] Seminario, J. M. *J. Phys. B* **2007**, *40*, F275.

- [32] Chen, J.; Reed, M. A.; Rawlett, A. M.; Tour, J. M. *Science* **1999**, *286*, 1550–1552.
- [33] Seminario, J. M.; Zacarias, A. G.; Tour, J. M. *J. Am. Chem. Soc.* **2000**, *122*, 3015–3020.
- [34] Tans, S. J.; Verschueren, A. R. M.; Dekker, C. *Nature* **1998**, *393*, 49–52.
- [35] Postma, H. W. C.; Teepen, T.; Yao, Z.; Grifoni, M.; Dekker, C. *Science* **2001**, *293*, 76–79.
- [36] Piva, P. G.; Dilabio, G. A.; Pitters, J. L.; Zikovsky, J.; Rezeq, M.; Dogel, . S.; Hofer, W. A.; Wolkow, R. A. *Nature* **2005**, *435*, 658–661.
- [37] Jaeger, R. C. *Introduction to Microelectronic Fabrication*; Prentice Hall: Upper Saddle River, New Jersey, 2002.
- [38] Maruccio, G.; Cingolani, R.; Rinaldi, R. *J. Mater. Chem.* **2004**, *14*, 542–554.
- [39] Balzani, V.; Venturi, M.; Credi, A. *Molecular Devices and Machines - A Journey into the Nano World*; Wiley-VCH, 2002.
- [40] Stan, M. R.; Franzon, P. D.; Goldstein, S. C.; Lach, J. C.; Ziegler, M. M. *Proceedings of the IEEE* **2003**, *91(11)*, 1940–1957.
- [41] Žutić, I.; Fabian, J.; Sarma, S. D. *Review of Modern Physics* **2004**, *76*, 323.
- [42] Baibich, M. N.; Broto, J. M.; Fert, A.; van Dau, F. N.; Petroff, F.; Etienne, P.; Creuzet, G.; Friederich, A.; Chazelas, J. *Phys. Rev. Lett.* **1988**, *61*, 2472.

- [43] Xiong, Z. H.; Wu, D.; Vardeny, Z. V.; Shi, J. *Nature* **2004**, *427*, 821.
- [44] Petta, J. R.; Slater, S. K.; Ralph, D. C. *Phys. Rev. Lett.* **2004**, *93*, 136601.
- [45] Rocha, A. R. *Theoretical and Computational Aspects of Electronic Transport at the Nanoscale (Ph.D dissertation)*; University of Dublin, Trinity College: Dublin, Ireland, 2007.
- [46] Tsukagoshi, K.; Alphenaar, B. W.; Ago, H. *Nature* **1999**, *401*, 572–574.
- [47] Emberly, E. G.; Kirczenow, G. *Chem. Phys.* **2002**, *281*, 311.
- [48] Pati, R.; Senapati, L.; Ajayan, P. M.; Nayak, S. K. *Phys. Rev. B* **2003**, *68*, 100407.
- [49] Rocha, A. R.; García-Suárez, V. M.; Bailey, S. W.; Lambert, C. J.; Ferrer, J.; Sanvito, S. *Nat. Mater.* **2005**, *4*, 335.
- [50] Emberly, E. G.; Kirczenow, G. *Phys. Rev. B* **2005**, *72*, 184407.
- [51] Wei, Y.; Xu, Y.; Wang, J.; Guo, H. *Phys. Rev. B* **2005**, *70*, 193406.
- [52] Zwolak, M.; Ventra, M. D. *Appl. Phys. Lett.* **2002**, *81*, 925.
- [53] de Pablo, P. J.; Moreno-Herrero, F.; Colchero, J.; Herrero, J. G.; Herrero, P.; Baró, A. M.; Ordejón, . P.; Soler, J. M.; Artacho, E. *Phys. Rev. Lett.* **2000**, *85*, 4992.

- [54] Okahata, Y.; Kobayashi, T.; Tanaka, K.; Shimomura, M. *J. Am. Chem. Soc.* **1998**, *120*, 6165–6166.
- [55] Fink, H. W.; Schönenberger, C. *Nature* **1999**, *398*, 407–410.
- [56] Xu, B.; Zhang, P.; Li, X.; Tao, N. *Nano Lett.* **2004**, *4*, 1105.
- [57] Porath, D.; Bezryadin, A.; de Vries, S.; Dekker, C. *Nature* **2000**, *403*, 635–638.
- [58] Cohen, H.; Nogues, C.; Naaman, R.; Porath, D. *Proc. Nat. Acad. Sci.* **2005**, *102*, 11589.
- [59] Cohen, H.; Nogues, C.; Ullien, D.; Daube, S.; Naaman, R.; Porath, D. *Faraday Discussions* **2006**, *131*, 367.
- [60] Kasumov, A. Y.; Kociak, M.; Guéron, S.; Reulet, B.; Volkov, V. T.; Bouchiat, H. *Science* **2001**, *291*, 280.
- [61] Taniguchi, M.; Tomoji, K. *Phys. Rev. E* **2004**, *70*, 011913.
- [62] Endres, R. G.; Cox, D. L.; Singh, R. R. P. *Rev. Mod. Phys.* **2004**, *76*, 195.
- [63] Gutierrez, R.; Mohapatra, S.; Cohen, H.; Porath, D.; Cuniberti, G. *cond-mat*.
- [64] Li, J.; Gershow, M.; Stein, D.; Brandin, E.; Golovchenko, J. A. *Nat. Mater.* **2003**, *2*, 611–615.
- [65] Zwolak, M.; Ventra, M. D. *Nano Lett.* **2005**, *5*, 421–424.
- [66] Lagerqvist, J.; Zwolak, M.; Ventra, M. D. *Nano Lett.* **2006**, *6*, 779–782.

- [67] Lagerqvist, J.; Zwolak, M.; Ventra, M. D. *Biophysical Journal* **2007**, *93*, 2384–2390.
- [68] Maruccio, G.; Visconti, P.; Arima, V.; D’Amico, S.; Biasco, A.; D’Amone, E.; Cingolani, R.; Rinaldi, R. *Nano Lett.* **2003**, *3*, 479–483.
- [69] Maruccio, G.; Biasco, A.; Visconti, P.; Bramanti, A.; Pompa, P. P.; Calabi, F.; Cingolani, R.; and S. Corni, R. R.; Felice, R. D.; Molinari, E.; Verbeet, M. P.; Canters, G. W. *Adv. Mater.* **2005**, *17*, 816–822.
- [70] Katz, E.; Willner, I. *ChemPhysChem* **2004**, *5*, 1084–1104.
- [71] Star, A.; Gabriel, J.-C. P.; Bradley, K.; Grüner, G. *Nano Lett.* **2003**, *3*, 459–463.
- [72] Chen, R. J.; Bangsaruntip, S.; Drouvalakis, K. A.; Kam, N. W. S.; Shim, M.; Li, Y.; Kim, W.; Utz, P. J.; Dai, H. *Proc. Natl. Acad. Sci.* **2003**, *100*, 4984–4989.
- [73] Bradley, K.; Briman, M.; Star, A.; Grüner, G. *Nano Lett.* **2004**, *4*, 253–256.
- [74] Chen, R. J.; Choi, H. C.; Bangsaruntip, S.; Yenilmez, E.; Tang, X.; Wang, Q.; Chang, Y. L.; Dai, H. *J. Am. Chem. Soc.* **2004**, *126*, 1563–1568.
- [75] Datta, S. *Online Lecture Notes: Concepts of Quantum Transport I - Nanodevices and Maxwell’s Demon*; <http://www.nanohub.org/resources/2041/> (accessed on May 16, 2008).
- [76] Mahan, G. D. *Many-Particle Physics*; Kluwer Academic/Plenum Publishers: New York, 2000.

- [77] Vasileska, D. *Course Lecture Notes: Semiconductor Transport*;
<http://www.eas.asu.edu/~vasilesk/EEE534.html> (accessed on May 16, 2008).
- [78] Pantelides, S. T.; Ventra, M. D.; Lang, N. D.; Rashkeev, S. N. *IEEE Trans. Nanotechnol.* **2002**, *1*, 86.
- [79] Kushmerick, J. G. *Materials Today* **2005**, *8* (7-8), 26–30.
- [80] Goodnick, S. M.; Vasileska, D. *Course Lecture Notes: Computational Electronics*; <http://www.eas.asu.edu/~eee598> (accessed on May 16, 2008), 1998.
- [81] Pecchia, A.; Carlo, A. D. *Rep. Prog. Phys.* **2004**, *67*, 1497–1561.
- [82] Datta, S. *Electronic Transport in Mesoscopic Systems*; Cambridge University Press: Cambridge, UK, 1995.
- [83] Landauer, R. *IBM J. Res. Dev.* **1988**, *32*, 306.
- [84] Landauer, R. *J. Phys. Condens. Matter* **1989**, *1*, 8099–8110.
- [85] Büttiker, M. *Phys. Rev. Lett.* **1986**, *57*, 1761–1764.
- [86] Büttiker, M. *IBM J. Res. Dev.* **1988**, *32*, 317.
- [87] McCreery, R. L. *Chem. Mater.* **2004**, *16*, 4477–4496.
- [88] Bardeen, J. *Phys. Rev. Lett.* **1961**, *6*, 57–59.
- [89] Tersoff, J.; Hamann, D. R. *Phys. Rev. Lett.* **1983**, *50*, 1998–2001.

- [90] Lang, N. D. *Phys. Rev. B* **1986**, *34*, 5947–5950.
- [91] Sharvin, Y. V.; Bogatina, N. I. *Sov. Phys. JETP* **1969**, *29*, 419.
- [92] van Wees, B. J.; van Houten, H.; Beenakker, C. W. J.; Williamson, J. G.; Kouwenhoven, L. P.; van der Marel, D.; Foxon, C. T. *Phys. Rev. Lett.* **1988**, *60*, 848.
- [93] Wharam, D.; Thornton, T. J.; Newbury, R.; Pepper, M.; Ahmed, H.; J. E. F. F.; Hasko, D. G.; Peacock, D. C.; Ritchie, D. A.; Jones, G. A. C. *J. Phys. C* **1988**, *21*, L209.
- [94] Cohen, M. H.; Falicov, L. M.; Phillips, J. C. *Phys. Rev. Lett.* **1962**, *8*, 316.
- [95] Harrison, W. A. *Surf. Sci.* **1994**, *299/300*, 298.
- [96] Rocha, A. R.; García-Suárez, V. M.; Bailey, S.; Lambert, C.; Ferrer, J.; Sanvito, S. *Phys. Rev. B* **2006**, *73*, 085414.
- [97] Palacios, J. J.; Pérez-Jiménez, A. J.; Louis, E.; Vergés, J. A. *Phys. Rev. B* **2001**, *64*, 115411.
- [98] Tian, W.; Datta, S.; Hong, S.; Reifenberger, R.; Henderson, J. I.; Kubiak, C. P. *J. Chem. Phys.* **1998**, *109*, 2874.
- [99] Fisher, D. S.; Lee, P. A. *Phys. Rev. B* **1981**, *23*, 6851.
- [100] Keldysh, L. V. *Sov. Phys. JETP* **1965**, *20*, 1018.

- [101] Caroli, C.; Combescot, R.; Nozieres, P.; Saint-James, D. *J. Phys. C: solid State Phys.* **1972**, *5*, 21.
- [102] Williams, A. R.; Feibelman, P. J.; Lang, N. D. *Phys. Rev. B* **1982**, *26*, 5433.
- [103] Carlo, A. D.; Gheorghe, M.; Lugli, P.; Stenberga, M.; Seifert, G.; Frauenheim, T. *Physica B* **2002**, *314*, 86.
- [104] Brandbyge, M.; Mozos, J. L.; Ordejon, P.; Taylor, J.; Stokbro, K. *Phys. Rev. B* **2002**, *65*, 165401.
- [105] Datta, S. *Quantum Transport: Atom to Transistor*; Cambridge University Press: Cambridge, UK, 2004.
- [106] Frederiksen, T.; Brandbyge, M.; Lorente, N.; Jauho, A. *Phys. Rev. Lett.* **2004**, *93*, 256601.
- [107] Sergueev, N.; Roubtsov, D.; Guo, H. *Phys. Rev. Lett.* **2005**, *95*, 146803.
- [108] Troisi, A.; Ratner, M. A. *Phys. Rev. B* **2005**, *72*, 33408.
- [109] Danielewicz, P. *Ann. Phys.* **1984**, *152*, 239.
- [110] Gartner, P.; Banyai, L.; Haug, H. *Phys. Rev. B* **2000**, *62*, 7116.
- [111] Szabo, A.; Ostlund, N. S. *Modern Quantum Chemistry*; Dover Publications, Inc.: New York, 1989.

- [112] Payne, M. C.; Teter, M. P.; Allan, D. C.; Arias, T. A.; Joannopoulos, J. D.
Rev. Mod. Phys. **1992**, *64*, 1045.
- [113] Merzbacher, E. *Quantum Mechanics*; John Wiley & Sons Inc.: New York, 1998.
- [114] Hohenberg, P.; Kohn, W. *Phys. Rev.* **1964**, *136*, B864.
- [115] Parr, R. G.; Yang, W. *Density Functional Theory of Atoms and Molecules*;
Oxford University Press: New York, 1989.
- [116] Kohn, W.; Sham, L. *Phys. Rev.* **1965**, *140*, A1133.
- [117] Zhang, G.; Musgrave, C. B. *J. Phys. Chem. A* **2007**, *111*, 1554.
- [118] von Barth, U.; Hedin, L. *J. Phys. C: Condens. Matt.* **1972**, *5*, 1629.
- [119] Perdew, J. P.; Zunger, A. *Phys. Rev. B* **1981**, *23*, 5048.
- [120] Perdew, J.; Wang, Y. *Phys. Rev. B* **1992**, *45*, 13244.
- [121] Perdew, J. P.; Burke, K.; Ernzerhof, M. *Phys. Rev. Lett.* **1996**, *77*, 3865.
- [122] Perdew, J. P.; Kurth, S. *Density Functionals for Non-relativistic Coulomb Sys-*
tems in the New Century, in Density Functionals: Theory and Applications;
Springer: Berlin, Volume 500, Lecture Notes in Physics, 1998.
- [123] Becke, A. D. *J. Chem. Phys.* **1993**, *45*, 5648.
- [124] Lee, C.; Yang, W.; Parr, R. G. *Phys. Rev. B* **1998**, *37*, 785.

- [125] He, H.; Orlando, R.; Blanco, M. A.; Pandey, R.; Amzallag, E.; Baraille, I.; Rérat, M. *Phys. Rev. B* **2006**, *74*, 195123.
- [126] Boys, S. F. *Proc. R. Soc. Londdon A* **1950**, *200*, 542.
- [127] Frisch, M. J.; et al.. *GAUSSIAN03*; Gaussian, Inc.: Pittsburgh, PA, 2003.
- [128] Kresse, G.; Furthmüller, J. *Phys. Rev. B* **1996**, *54*, 11169.
- [129] Soler, J. M.; Artacho, E.; Gale, J. D.; García, A.; Junquera, J.; Ordejón, P.; Sánchez-Portal, D. *J. Phys.: Condens. Matt.* **2002**, *14*, 2745.
- [130] Koch, W.; Holthausen, M. C. *A Chemist's Guide to Density Functional Theory*; Wiley-VCH: Weinheim, 2001.
- [131] Martin, R. M. *Electronic Structure, Basic Theory and Practical Methods*; Cambridge University Press: Cambridge, 2004.
- [132] Hamann, D. R.; Schlüter, M.; Chiang, C. *Phys. Rev. Lett.* **1979**, *43*, 1494.
- [133] Bachelet, G. B.; Hamann, D. R.; Schlüter, M. *Phys. Rev. B* **1982**, *26*, 4199.
- [134] Troullier, N.; Martins, J. L. *Phys. Rev. B* **1991**, *43*, 1993.
- [135] Vanderbilt, D. *Phys. Rev. B* **1990**, *41*, 7892.
- [136] Dieny, B.; Speriosu, V. S.; Parkin, S. S. P.; Gurney, B. A.; Wilhoit, D. R.; Mauri, D. *Phys. Rev. B* **1991**, *43*, 1297.

- [137] Andres, R. P.; Bein, T.; Dorogi, M.; Feng, S.; Henderson, J. I.; Kubiak, C. P.; Mahoney, W.; Osifchin, R. G.; Reifenberger, R. *Science* **1996**, *272*, 1323.
- [138] Wu, S. W.; Nazin, G. V.; Chen, X.; Qiu, X. H.; Ho, W. *Phys. Rev. Lett.* **2004**, *93*, 236802.
- [139] Moresco, F.; Meyer, G.; Rieder, K.; Tang, H.; Gourdon, A.; Joachim, C. *Phys. Rev. Lett.* **2001**, *86*, 672.
- [140] Collier, C. P.; Wong, E. W.; Belohradsky, M.; Raymo, F. M.; Stoddart, J. F.; Kuekes, P. J.; Williams, R. S.; Heath, J. R. *Science* **1999**, *285*, 391.
- [141] Mujica, V.; Kemp, M.; Roitberg, A.; Ratner, M. A. *J. Chem. Phys.* **1996**, *104*, 7296.
- [142] Ventra, M. D.; Pantelides, S. T.; Lang, N. D. *Phys. Rev. Lett.* **2000**, *84*, 979.
- [143] Taylor, J.; Guo, H.; Wang, J. *Phys. Rev. B* **2001**, *63*, 245407.
- [144] Ghosh, A. W.; Zahid, F.; Datta, S.; Birge, R. *Chem. Phys.* **2002**, *281*, 225.
- [145] Heurich, J.; Cuevas, J. C.; Wenzel, W.; Schön, G. *Phys. Rev. Lett.* **2002**, *88*, 256803.
- [146] Pati, R.; Karna, S. P. *Chem. Phys. Lett.* **2002**, *351*, 302.
- [147] Mullins, D. R.; Huntley, D. R.; Tang, T.; Saldin, D. K.; Tysoe, W. T. *Surf. Sci.* **1997**, *380*, 468.

- [148] Bolotov, L.; Uchida, N.; Kanayama, T. *Eur. Phys. J. D* **2001**, *16*, 271.
- [149] Grad, G. B.; Blaha, P.; Schwarz, K.; Auwärter, W.; Greber, T. *Phys. Rev. B* **2003**, *68*, 085404.
- [150] Knickelbein, M. B.; Yang, S.; Riley, S. J. *J. Chem. Phys.* **1990**, *93*, 94.
- [151] Butler, W. H.; Zhang, X.-G.; Schulthess, T. C.; MacLaren, J. M. *Phys. Rev. B* **2001**, *63*, 054416.
- [152] Teresa, J. M. D.; Barthélémy, A.; Fert, A.; Contour, J. P.; Lyonnet, R.; Montaigne, F.; Seneor, P.; Vaurés, A. *Phys. Rev. Lett.* **1999**, *82*, 4288.
- [153] Pasupathy, A. N.; Bialczak, R. C.; Martinek, J.; Grose, J. E.; Donev, L. A. K.; McEuen, P. L.; Ralph, D. C. *Science* **2004**, *306*, 86.
- [154] Utsumi, Y.; Martinek, J.; Schön, G.; Imamura, H.; Maekawa, S. *Phys. Rev. B* **2005**, *71*, 245116.
- [155] Fasel, R.; Aebi, P.; Agostino, R. G.; Naumović, D.; Osterwalder, J.; Santaniello, A.; Schlapbach, L. *Phys. Rev. Lett.* **1996**, *76*, 4733.
- [156] Untiedt, C.; Dekker, D. M. T.; Djukic, D.; van Ruitenbeek, J. M. *Phys. Rev. B* **2004**, *69*, 081401R.
- [157] Mathur, P.; Mavunkal, I. J.; Umbarkar, S. B. *J. Cluster Sci.* **1998**, *9*, 393.
- [158] Alemany, M. M. G.; Diéguez, O.; Rey, C.; Gallego, L. J. *J. Chem. Phys.* **2001**, *114*, 9371.

- [159] Rabilloud, F.; Rayane, D.; Allouche, A. R.; Antoine, R.; Aubert-Frécon, M.; Broyer, M.; Compagnon, I.; Dugouret, P. *J. Phys. Chem. A* **2003**, *107*, 11347.
- [160] Taylor, J.; Guo, H.; Wang, J. *Phys. Rev. B* **2001**, *63*, 121104R.
- [161] Sergueev, N.; Roubtsov, D.; Guo, H. *arXiv:cond-mat/0309614*.
- [162] Gimzewski, J. K.; Joachim, C. *Science* **1999**, *283*, 1683.
- [163] Dag, S.; Gülseren, O.; Ciraci, S.; Yildirim, T. *Appl. Phys. Lett.* **2003**, *83*, 3180.
- [164] Moore, G. E. *Electronics* **1965**, *65*, 114.
- [165] *International Technology Roadmap for Semiconductors*;
<http://www.itrs.net/reports.html> (web access on Oct. 16, 2008), 2007.
- [166] Geddes, N. J.; Sambles, J. R.; Jarvis, D. J.; Parker, W. G.; Sandman, D. J. *Appl. Phys. Lett.* **1990**, *56*, 1916.
- [167] Metzger, R. M.; Xu, T.; Peterson, I. R. *Angew. Chem. Int. Ed. Engl.* **2001**, *40*, 1749.
- [168] Krzeminski, C.; Delerue, C.; Allan, G.; Vuillaume, D. *Phys. Rev. B* **2001**, *64*, 085405.
- [169] Taylor, J.; Brandbyge, M.; Stokbro, K. *Phys. Rev. Lett.* **2002**, *89*, 138301.
- [170] Stokbro, K.; Taylor, J.; Brandbyge, M. *J. Am. Chem. Soc.* **2003**, *125*, 3674.
- [171] Staykov, A.; Nozaki, D.; Yoshizawa, K. *J. Phys. Chem. C* **2007**, *111*, 11699.

- [172] Lang, N. D.; Solomon, P. M. *Nano Lett.* **2005**, *5*, 921.
- [173] Yaliraki, S. N.; Kemp, M.; Ratner, M. A. *J. Am. Chem. Soc.* **1999**, *121*, 3428.
- [174] Lang, N. D.; Kagan, C. R. *Nano Lett.* **2006**, *6*, 2955.
- [175] Lamoen, D.; Ballone, P.; Parrinello, M. *Phys. Rev. B* **1996**, *54*, 5097.
- [176] Dhirani, A.; Lin, P. H.; Guyot-Sionnest, P.; Zehner, R. W.; Sita, L. R. *J. Chem. Phys.* **1997**, *106*, 5249.
- [177] Elbing, M.; Ochs, R.; Koentopp, M.; Fischer, M.; von Hänisch, C.; Weigend, F.; Evers, F.; Weber, H. B.; Mayor, M. *Proc. Nat. Acad. Sci. USA* **2005**, *102*, 8815.
- [178] Jäckel, F.; Watson, M. D.; Mllen, K.; Rabe, J. P. *Phys. Rev. Lett.* **2004**, *92*, 188303.
- [179] Park, H.; Park, J.; Lim, A. K. L.; Anderson, E. H.; Alivisatos, A. P.; McEuen, P. L. *Nature* **2000**, *407*, 57.
- [180] Yu, L. H.; Natelson, D. *Nanotechnology* **2004**, *15*, S517.
- [181] Martel, R.; Schmidt, T.; Shea, H. R.; Hertel, T.; Avouris, P. *Appl. Phys. Lett.* **1998**, *73*, 2447.
- [182] Luo, K.; Chae, D.-H.; Yao, Z. *Nanotechnology* **2007**, *18*, 465203.
- [183] Ventra, M. D.; Pantelides, S. T.; Lang, N. D. *Appl. Phys. Lett.* **2000**, *76*, 3448.

- [184] Rashkeev, S. N.; Ventra, M. D.; Pantelides, S. T. *Phys. Rev. B* **2002**, *66*, 033301.
- [185] Yu, L. H.; Keane, Z. K.; Ciszek, J. W.; Cheng, L.; Tour, J. M.; Baruah, T.; Pederson, M. R.; Natelson, D. *Phys. Rev. Lett.* **2005**, *95*, 256803.
- [186] Perrine, T. M.; Smith, R. G.; Marsh, C.; Dunietz, B. D. *J. Chem. Phys.* **2008**, *128*, 154706.
- [187] Consortium, I. H. G. S. *Nature* **2001**, *409*, 860.
- [188] Futreal, P. A.; Kasprzyk, A.; Birney, E.; Mullikin, J. C.; Wooster, R.; Stratton, M. R. *Nature* **2001**, *409*, 850.
- [189] Jimenez-Sanchez, G.; Childs, B.; Valle, D. *Nature* **2001**, *409*, 853.
- [190] Chakravarti, A. *Nature* **2001**, *409*, 822.
- [191] Church, G. M. *Scientific American* **2006**, *294*, 47.
- [192] Stoneking, M. *Nature* **2001**, *409*, 821.
- [193] Fredlake, C. P.; Hert, D. G.; Mardis, E. R.; Barron, A. E. *Electrophoresis* **2006**, *27*, 3689.
- [194] Chan, E. Y. *Mutat. Res.* **2005**, *573*, 13.
- [195] Kasianowicz, J. J.; Brandin, E.; Branton, D.; Deamer, D. W. *Proc. Natl. Acad. Sci. USA* **1996**, *93*, 13770.

- [196] Akeson, M.; Branton, D.; Kasianowicz, J. J.; Brandin, E.; Deamer, D. W. *Biophysical Journal* **1999**, *77*, 3227.
- [197] Meller, A.; Nivon, L.; Brandin, E.; Golovchenko, J.; Branton, D. *Proc. Natl. Acad. Sci. USA* **2000**, *97*, 1079.
- [198] Deamer, D. W.; Akeson, M. *Trends Biotechnol.* **2000**, *18*, 147.
- [199] Khanna, V. K. *Biotechnol. Advances* **2007**, *25*, 85.
- [200] Fologea, D.; Gershow, M.; Ledden, B.; McNabb, D. S.; Golovchenko, J. A.; Li, J. *Nano Lett.* **2005**, *5*, 1905.
- [201] Vercoutere, W. A.; Winters-Hilt, S.; DeGuzman, V. S.; Deamer, D.; Ridino, S. E.; Rodgers, J. T.; Olsen, H. E.; Marziali, A.; Akeson, M. *Nucleic Acids Research* **2003**, *31*, 1311.
- [202] Rhee, M.; Burns, M. A. *Trends Biotechnol.* **2007**, *25*, 174.
- [203] Zwolak, M.; Ventra, M. D. *Rev. Mod. Phys.* **2008**, *80*, 141.
- [204] Louie, S. G.; Froyen, S.; Cohen, M. L. *Phys. Rev. B* **1982**, *26*, 1738.
- [205] Artacho, E.; Sánchez-Portal, D.; Ordejón, P.; García, A.; Soler, J. M. *Phys. Stat. Sol. B* **1999**, *215*, 809.
- [206] Berman, H. M.; Olson, W. K.; Beveridge, D. L.; Westbrook, J.; Gelbin, A.; Demeny, T.; Hsieh, S. H.; Srinivasan, A. R.; Schneider, B. *BioPhys. J.* **1992**, *63*, 751.

- [207] Tjandra, N.; Tate, S.; Ono, A.; Kainosho, M.; Bax, A. *J. Am. Chem. Soc.* **2000**, *122*, 6190.
- [208] Rocha, A. R.; García-Suárez, V. M.; Bailey, S.; Lambert, C.; Ferrer, J.; Sanvito, S. *Computer code SMEAGOL (Spin and Molecular Electronics in an Atomically Generated Orbital Landscape)*; www.smeagol.tcd.ie.
- [209] Pettifor, D. *Bonding and Structure of Molecules and Solids*; Oxford University Press: Oxford, 2002.
- [210] Zhao, Q.; Sigalov, G.; Dimitrov, V.; Dorvel, B.; Mirsaidov, U.; Sligar, S.; Aksimentiev, A.; Timp, G. *Nano Lett.* **2007**, *7*, 1680.
- [211] Noše, S. *J. Chem. Phys.* **1984**, *81*, 511.
- [212] Bylander, D. M.; Kleinman, L. *Phys. Rev. B* **1992**, *46*, 13756.
- [213] Kelly, R. E. A.; Kantorovich, L. N. *J. Phys. Chem. C* **2007**, *111*, 3883.
- [214] Šponer, J.; Lankaš, F. (eds.) *Computational Studies of RNA and DNA, Chapter 14 "Base stacking and base pairing"*; by J. Šponer and P. Jurečka and P. Hobza: Springer Netherlands, 2006.
- [215] He, H.; Scheicher, R. H.; Pandey, R.; Rocha, A. R.; Sanvito, S.; Grigoriev, A.; Ahuja, R.; Karna, S. P. *J. Phys. Chem. C* **2008**, *112*, 3456.
- [216] Zikic, R.; Krstić, P. S.; Zhang, X.-G.; Ruentes-Cabrera, M.; Wells, J.; Zhao, X. *Phys. Rev. E* **2006**, *74*, 011919.

- [217] Kelly, R. E. A.; Lee, Y. J.; Kantorovich, L. N. *J. Phys. Chem. B* **2005**, *109*, 11933.
- [218] He, J.; Lin, L.; Zhang, P.; Lindsay, S. *Nano Lett.* **2007**, *7*, 3854.
- [219] Ohshiro, T.; Umezawa, Y. *Proc. Natl. Acad. Sci. USA* **2006**, *103*, 10.
- [220] Zheng, G.; Patolsky, F.; Cui, Y.; Wang, W. U.; Lieber, C. M. *Nature Biotech.* **2005**, *23*, 1294.
- [221] Galperin, M.; Ratner, M. A. *Nano Lett.* **2004**, *4*, 1605.
- [222] Muralidharan, B.; Ghosh, A. W.; Pati, S. K.; Datta, S. *arXiv:cond-mat/0505375*.
- [223] Yang, Z.; Chshiev, M.; Zwolak, M.; Chen, Y. C.; Ventra, M. D. *Phys. Rev. B* **2005**, *71*, 041402(R).
- [224] Runge, E.; Gross, E. K. U. *Phys. Rev. Lett.* **1984**, *52*, 997.
- [225] Ventra, M. D.; Todorov, T. N. *J. Phys.: Condens. Matt.* **2004**, *16*, 8025.
- [226] Tomfohr, J. K.; Sankey, O. F. *Phys. Status Solidi b* **2001**, *226*, 115.
- [227] *Basic Energy Sciences Advisory Committee, Directing Matter and Energy: Five Challenges for Science and the Imagination*; <http://www.science.doe.gov/production/bes/reports/list.html> (accessed on May 14, 2008), 2007.